Pacific Northwest
NATIONAL LABORATORY

PNNL-30440 Rev 1
DVZ-RPT-0049 Rev 1

Spectral Induced Polarization-Biogeochemical Relationships for Remediation Amendment Monitoring

September 2021

Hilary P. Emerson
James E. Szecsody
Amanda Lawter
Christopher Halter
Adam Mangel
Eleda Fernald
Tom Resch
Katherine Muller
Kitt Bagwell
Mark Bowden
Odeta Qafoku
Jonathan Thomle
Nikolla Qafoku
Vicky Freedman

U.S. DEPARTMENT OF ENERGY

Prepared for the U.S. Department of Energy
under Contract DE-AC05-76RL01830

DISCLAIMER

PACIFIC NORTHWEST NATIONAL LABORATORY
operated by
BATTELLE
for the
UNITED STATES DEPARTMENT OF ENERGY
under Contract DE-AC05-76RL01830

Printed in the United States of America

Available to DOE and DOE contractors from the
Office of Scientific and Technical Information,
P.O. Box 62, Oak Ridge, TN 37831-0062;
ph: (865) 576-8401
fax: (865) 576-5728
email: reports@adonis.osti.gov

Available to the public from the National Technical Information Service
5301 Shawnee Rd., Alexandria, VA 22312
ph: (800) 553-NTIS (6847)
email: orders@ntis.gov <https://www.ntis.gov/about>
Online ordering: http://www.ntis.gov

PNNL-30440 Rev 1
DVZ-RPT-0049 Rev 1

Spectral Induced Polarization-Biogeochemical Relationships for Remediation Amendment Monitoring

September 2021

Hilary P. Emerson
James E. Szecsody
Amanda Lawter
Christopher Halter
Adam Mangel
Eleda Fernald
Tom Resch
Katherine Muller
Kitt Bagwell
Mark Bowden
Odeta Qafoku
Jonathan Thomle
Nikolla Qafoku
Vicky Freedman

Prepared for
the U.S. Department of Energy
under Contract DE-AC05-76RL01830

Pacific Northwest National Laboratory
Richland, Washington 99354

Abstract

Geophysical tools can indirectly monitor subsurface changes in response to remedial injections. These methods exhibit relatively low spatial resolution compared to sediment core characterization but are advantageous due to the ability to collect measurements non-intrusively over time across large volumes of the subsurface. Moreover, along with confirmatory groundwater or core sampling, geophysical methods can be used during active biogeochemical remedies to monitor short-term contaminant transformations and mobility, as well as part of an overall strategy for long-term monitoring of subsurface contaminated sites. The use of alternating current spectral induced polarization (SIP) provides significantly more information than conventional geophysical methods like direct current electrical resistivity (ER). SIP allows for monitoring frequency-specific changes in both solution and surface conductivity by separation of real and imaginary conductivity, respectively, as well as surface capacitance, while ER methods only measure the bulk conductivity (combined solution and surface conductivity) at a single frequency. SIP may be able to differentiate indicators of remedy progression such as precipitation reactions that sequester contaminants and changes in solution conductivity, potentially providing a better indication of amendment delivery and reactivity as compared to conventional ER methods. However, multiple processes and material properties have overlapping (interacting) electrical responses across a range of frequencies. Hence, the purpose of this scoping study was to evaluate if SIP can be used to monitor (a) amendment delivery and (b) precipitation and reactivity of amendments under consideration at Hanford with the ultimate goal of differentiating major reactions (e.g., mineral formation versus delivery of a high ionic strength amendment).

The purpose of this study is to evaluate the sensitivity of alternating current (AC) SIP for non-intrusively monitoring the delivery of different amendments into the subsurface and the subsequent reactions (i.e., develop relationships between the biogeochemical amendment concentration and the SIP response). These experiments are designed to collect SIP data during geochemical and physical alterations of the subsurface as part of single- or two-step remediation processes, which may include the initial delivery of a reductant (e.g., iron) followed by a secondary injection intended to co-precipitate and form coatings of relatively low-solubility phases (e.g., apatite and calcite) on the surfaces of reactive minerals and/or amendments that have immobilized contaminants, making them less likely to re-oxidize and re-mobilize in solution. SIP measurements were collected in fully saturated columns packed with sand and Hanford formation sediments containing (a) amendments that were highly conductive with significant capacitance (zero valent iron – ZVI, sulfur modified iron – SMI) and (b) amendments that exhibited low electrical conductivity with a small capacitance (calcite, apatite, bismuth). The sand was a quartz material with homogenous particle size that exhibited a relatively low surface conductivity. It was used as a control for comparison with the sediments from the Hanford Site, which have a greater surface conductivity because of their complex mineralogy and heterogeneous particle size distribution and may have complex interactions with amendments. The amendment mass fraction was varied to represent the different stages and subsurface locations associated with the delivery of a remedy.

Figure S.1 summarizes results for the amendments tested through this project. The SIP phase shift or imaginary conductivity change for the high-conductivity amendments was more than 10 times that of the low-conductivity amendments, highlighting the relative ease of detecting ZVI and SMI independent of the background signal from sand or Hanford sediments which suggests SIP may be appropriate for monitoring delivery of ZVI or SMI to a source of contamination. The ZVI phase shift and imaginary conductivity changes occur primarily at high frequency (> 100 Hz) whereas SMI changes were at low frequency (0.01 to 10 Hz) further confirming that we can differentiate between the two amendments. SIP signals of SMI also increased over time and the maximum shifted to lower frequencies highlighting that we may be able to detect changes in amendment reactivity or efficacy of treatment over time. The low-conductivity amendments (calcite, abiotic and biotic apatite, bismuth subnitrate) exhibited relatively small

phase and imaginary conductivity changes when added to sediments. The changes were above minimum detection limits (0.5 mrad for phase shift, 0.03 µS/cm for imaginary conductivity) for the highest concentration except for the commercial bismuth material. The lowest amendment concentration that can be detected is likely sediment specific, as minerals in sediments (clays, magnetite, Fe-oxides) have some capacitance and therefore exhibit a variable phase shift. While additional testing was conducted for calcite and apatite amendments to consider *in situ* delivery and sediment coating processes, testing ceased for bismuth until a solution delivery option is available. The low-conductivity apatite and calcite amendments were detectable in sediments due to their ability to *decrease* the phase shift and imaginary conductivity of specific sediment surfaces as observed in some conditions in *in situ* experiments with Hanford formation sediments with and without ZVI or SMI as they coated sediment surfaces with low conductivity phases. The simultaneous collection of both bulk conductivity (ER) and SIP should be considered for field-scale monitoring with SIP targeting detection and monitoring of contaminant source terms and ER for larger scale monitoring of the surrounding plumes. Therefore, future experiments should focus on performing SIP monitoring under unsaturated conditions using electrodes optimized for this purpose and scaling up experiments (e.g., to 2D boxes) to identify additional sensitivities associated with electrode configurations.

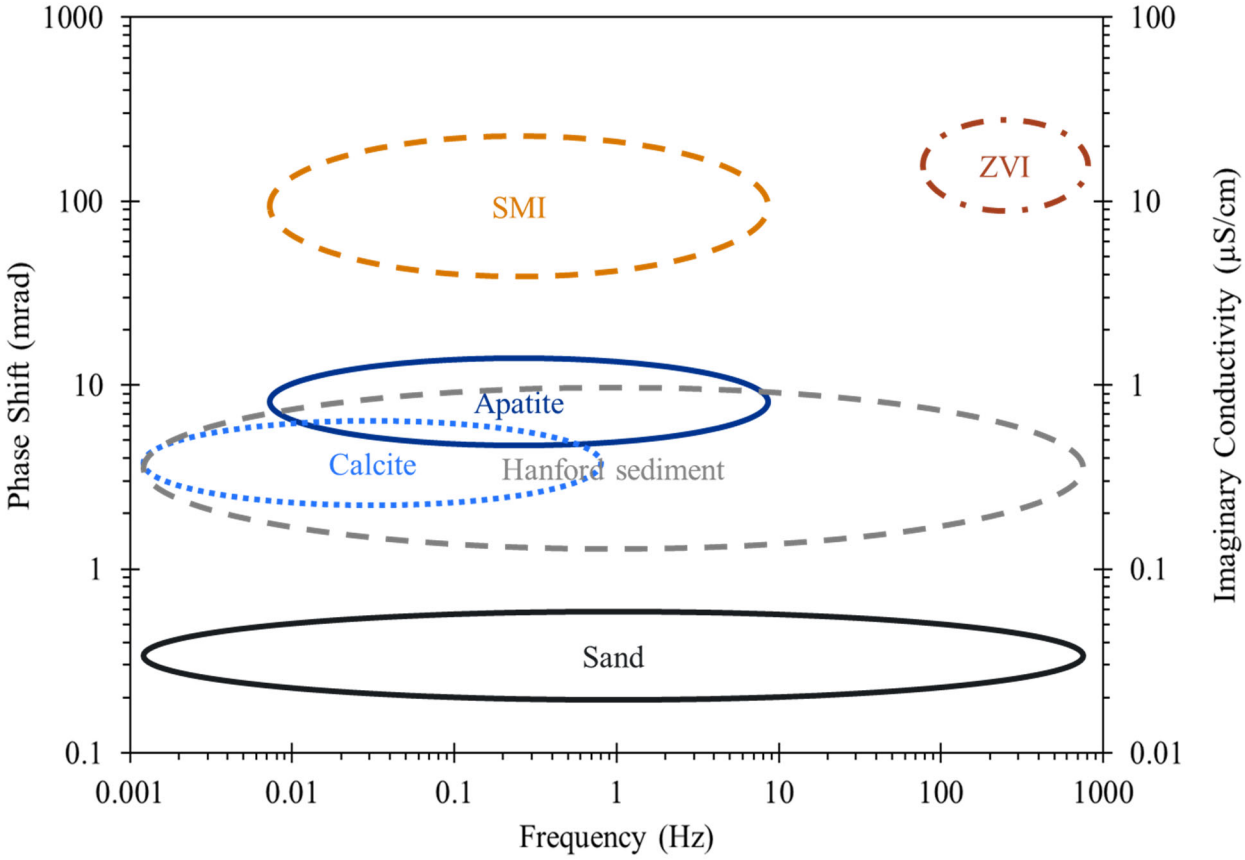

Figure S.1. Qualitative summary of results for the amendments and porous media tested through this project.

Acknowledgments

Funding for this work was provided by the U.S. Department of Energy Richland Operations Office under the Deep Vadose Zone – Applied Field Research Initiative. The Pacific Northwest National Laboratory is operated by Battelle Memorial Institute for the Department of Energy under Contract DE-AC05-76RL01830.

Acronyms and Abbreviations

AC	alternating current
AGW	artificial groundwater
APW	artificial perched water
BET	Brunauer – Emmett – Teller
CI	confidence interval
CPS	calcium polysulfide
EDL	electrical double layer
ER	electrical resistivity
IC	inorganic carbon
ICDD	International Center for Diffraction Data
ICP-OES	inductively coupled plasma optical emission spectrometry
ID	inner diameter
IFRC	Integrated Field Research Challenge
IP	induced polarization
NQAP	Nuclear Quality Assurance Program
PEEK	polyether ether ketone
PET	polyethylene terephthalate
PTFE	polytetrafluoroethylene
PVC	polyvinyl chloride
SIP	spectral induced polarization
SMB	sub miniature version B (type of radio frequency connector)
SMI	sulfur modified iron
TOC	total organic carbon
TC	total carbon
XRD	X-ray diffraction
ZVI	zero valent iron

Contents

Figures

Tables

1.0 Introduction

Groundwater sampling has been reliably used to infer reactions occurring *in situ* during both active and passive remediation. While groundwater sampling is informative, there are disadvantages associated with solely relying on groundwater sampling to confirm that biogeochemical reactions are occurring, including (1) low spatial resolution (i.e., point measurements), (2) high cost (i.e., monitoring well installation and sampling), (3) poor representation for low-permeability regions, and (4) lack of sensitivity to surficial and interfacial reactions that are important but do not result in major changes to bulk groundwater chemistry (e.g., Williams et al. 2009). Noninvasive geophysical tools, however, can indirectly monitor large volumes of the subsurface with relatively high spatial resolution. Along with confirmatory groundwater sampling, geophysical methods can monitor physical and geochemical changes to the subsurface during active biogeochemical remedies as indicators of contaminant transformations, as well as part of an overall strategy for long-term monitoring of subsurface contaminated sites (Binley and Slater 2020).

Electrical resistivity (ER) methods can be employed to measure bulk conductivity (the inverse of resistivity) changes spatially over time during injection. This geophysical technique is commonly used to correlate changes in the bulk conductivity with changes in total ionic strength in the subsurface (Johnson et al. 2013; Truex et al. 2018). However, ER measurements cannot be correlated directly with specific surface alterations or reactions induced by an amendment because bulk electrical conductivity cannot be separated into solution and surface components, as ER involves measurement at only a single frequency. Moreover, field ER measurements often cannot differentiate changes induced by remediation activities from baseline heterogeneities due to changes in both solution and surface conductivity. The spectral induced polarization (SIP) method provides significantly more information with collection of frequency-specific ER and phase shift measurements allowing for separation of bulk electrical conductivity into real and imaginary conductivity. SIP can then be used to distinguish between aqueous properties (e.g., ionic strength) observed in the real conductivity and surface reactions (e.g., adsorption, precipitation, biofilm growth) that modify surface properties (e.g., surface area, grain size, polarizability) observed in both the real and imaginary conductivity. SIP is especially useful as the resistivity of minerals in the subsurface spans almost 18 orders of magnitude (Schön 2011). There is potential for collection of ER and SIP data as part of a cohesive monitoring plan (e.g., SIP for monitoring of secondary reactions at sediment surfaces in source zones and ER for surveying of larger, surrounding areas).

Previous studies have demonstrated the utility of SIP methods for physical/chemical characterization of subsurface sediments (Kemna et al. 2012; Vinegar and Waxman 1984) and to delineate contaminant plumes (Orozco et al. 2012; Sogade et al. 2006). For example, changes in induced polarization (IP) signals during bio-reduction by injection of acetate, microbe-induced carbonate precipitation, and detection of organic plumes were observed previously (Ntarlagiannis et al. 2016; Orozco et al. 2011; Saneiyan et al. 2019). Williams et al. (2009) applied an IP method at the Rifle Integrated Field Research Challenge (IFRC) site to monitor responses during active remediation of uranium-contaminated groundwater. Frequency-dependent responses that corresponded to iron sulfide (FeS_2, FeS) mineral precipitation were measured as a direct consequence of *in situ* bio-stimulation during acetate injections (Orozco et al. 2011).

Mwakanyamale et al. (2012) suggested that SIP should be acquired whenever possible to improve the quantitative interpretation of these measurements. However, while advantageous, the application of SIP is complicated by multiple physical and geochemical processes and material properties with overlapping (interacting) electrical responses across a range of frequencies that can be difficult to disentangle (e.g., Doetsch et al. 2015; Placencia-Gómez et al. 2015; Williams et al. 2009). SIP electrical responses are not well understood for the biogeochemical processes that are encountered at complex contaminated sites. Hence, systematic studies are needed to accurately evaluate the utility and feasibility of SIP for field site

characterization and monitoring during active remediation with a focus on the low frequency range (< 1000 Hz), as this is most applicable for field data collection (Atekwana and Slater 2009).

Hence, the purpose of this study is to evaluate the sensitivity of alternating current (AC) SIP for non-intrusively monitoring the delivery of different amendments into the subsurface and the subsequent reactions (i.e., develop relationships between the biogeochemical amendment concentration and the SIP response). These experiments are designed to collect SIP data during geochemical and physical alterations of the subsurface as part of single- or two-step remediation processes, which may include the initial delivery of a reductant (e.g., iron) followed by a secondary injection intended to co-precipitate and form coatings of relatively low-solubility phases (e.g., apatite and calcite) on the surfaces of reactive minerals and/or amendments that have immobilized contaminants, making them less likely to re-oxidize and re-mobilize in solution. These technologies are currently under consideration for future remediation of vadose and perched water zones, such as BY Cribs, BC Cribs and Trenches, S-SX Tank Farm, C Tank Farm, and 216-U-1&2 (DOE/RL 2019).

1.1 SIP Description

The SIP effect is primarily linked to a buildup of excess ions in the electrical double layer (EDL) during current injection (Binley and Slater 2020). Early research ruled out significant contributions from other phenomena, including electro-osmotic and thermal electric mechanisms, but noted the importance of mineral geometry for ion diffusion (Marshall and Madden 1959). When an AC is applied to a sediment/water system, most of the current flows through the pore water (1 – *red,* in Figure 1.1), some current along mineral surfaces (2 – *black,* depending on the specific minerals present), and some current through minerals (3 – *blue*). The SIP response of porous media is governed by the frequency-dependent complex conductivity ($\sigma = \sigma' + i\sigma''$) generally collected at frequencies below 10 kHz. The total (or complex) conductivity or resistance is measured in parallel to a known reference resistor (Figure 1.1). Complex conductivity consists of two components: (1) the real conductivity and (2) the imaginary conductivity. The real (σ') conductivity is due to (1) pore water conductivity, σ'_w, which is dependent on electromigration of ions through the bulk pore water; and (2) surface conductivity, σ'_{surf}, which includes interactions within the EDL of grain surfaces (Abdel Aal et al. 2004; Kemna et al. 2012) with pore water conductivity generally representing the majority of the real conductivity in porous media.

Conversely, imaginary (σ'') conductivity is associated with ionic polarization of the EDL at the grain surface-pore water interface based on charge accumulation and transfer reactions (Abdel Aal et al. 2004; Kemna et al. 2012; Binley and Slater 2020). The imaginary conductivity can also be used to calculate two intrinsic properties of porous media: (1) chargeability (M) and (2) relaxation time (t_o), which differ between minerals. Phase shift is measured alongside resistivity to separate real and imaginary conductivity. It represents the lag in an applied AC sine wave traveling through a sample due to charge storage (1 radian = 57.3 degrees). The AC current through the sediment (purple in Figure 1.1) may lag (i.e., phase shift) relative to a reference resistor (*blue*). Moreover, the (1) solution resistance, (2) surface resistance, and (3) capacitance in Figure 1.1a correspond to the equivalent circuit as RS, R1, and C1, respectively, in Figure 1.1b. Multiple frequencies of applied AC current are used for data collection (i.e., SIP) as the response may be frequency specific.

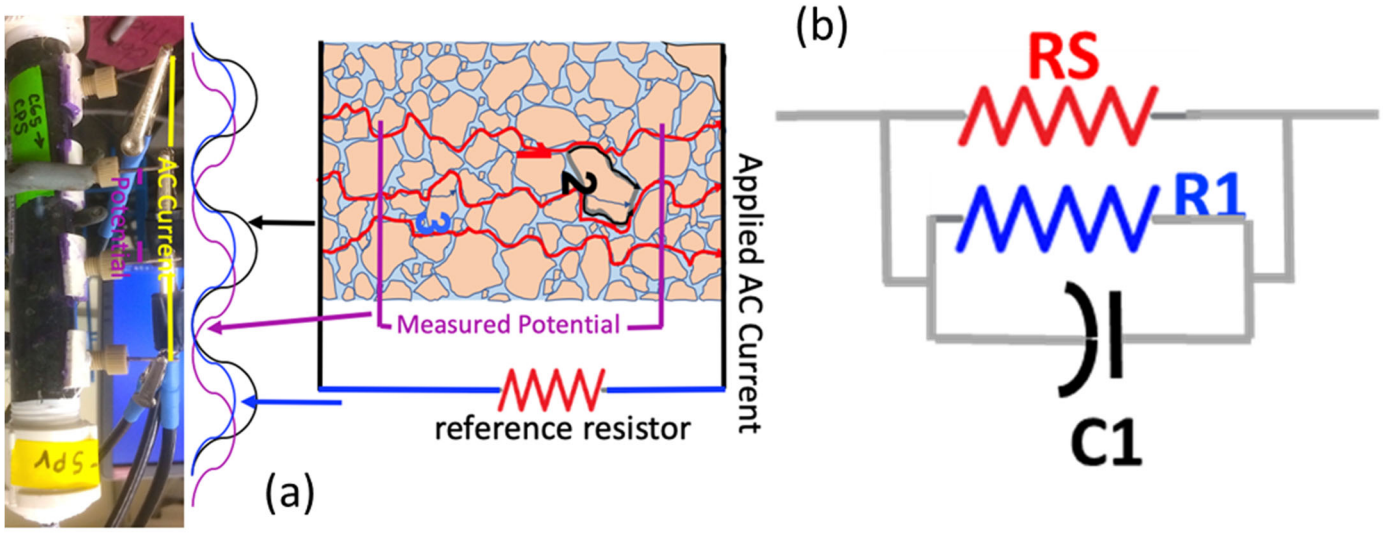

Figure 1.1. SIP 4-electrode configuration and circuit diagram (a), and an example of an equivalent electrical circuit (b) (Szecsody 2020a).

Electrolytic conduction (real term) and surface conduction (complex term – real and imaginary) are the two primary mechanisms at frequencies < 1 kHz (Kemna et al. 2012; Mwakanyamale et al. 2012). The real conductivity component is strongly controlled by fluid conductivity, porosity, and surface area or grain size distribution. Prominent features impacting the imaginary conductivity term include mineralogical composition, surface area, pore size, surface charge density, aqueous ionic composition, mineral's exchange capacity, and redox reactions (Archie 1942; Lesmes and Frye 2001; Revil and Glover 1998; Binley and Slater 2020). Electrochemical polarization is expected to dominate at low frequencies (< 1000 Hz) due to migration of counterions in the Stern layer of the EDL and back diffusion of ions in pore spaces (Mellage et al. 2018).

1.1.1 Electrical Response of Sediments

Both ER and SIP techniques have historically been used to characterize sediments. However, the resistivity of sediments can vary widely (nearly 18 orders of magnitude; Schön 2011) and may be differentiated from the resistivity of pore fluids only using SIP. For example, experiments at the Rifle IFRC site in Colorado reported resistivity values for sediments prior to field remediation of 10 to 400 Ω·m for sediments with high clay content and sand/gravel (Orozco et al. 2011; Williams et al. 2009), although some have reported values as high as 30,000 Ω·m (Sogade et al. 2006). However, the phase response is small in comparison to resistivity. Previous phase shift measurements in soils and sediments were between 1 and 20 mrad (Orozco et al. 2011; Williams et al. 2009; Zimmermann et al. 2008a,b). A review of 56 sandstone samples reported a range of formation factors from 9.0 to 151.4, an imaginary conductivity 0.03 to 1.07 mS/m, and a chargeability 0.17 to 4.77 mV/m (Weller et al. 2015). Note that chargeability as high as 20 mV/m was observed during prospecting for manganese ore deposits (Vieira et al. 2016).

Previously, SIP was correlated with specific sediments based on geochemical and physical properties. For example, normalized chargeability has been shown to correlate strongly with mineral phases including clay content (R^2 = 0.97) (Slater and Lesmes 2002). However, physical parameters like permeability, porosity, particle size, and geometry also play a role. The shape of the spectra across the frequency range may also correlate with grain or pore size distribution (Lesmes and Morgan 2001; Bücker et al. 2018,

2019). Modeling by Bücker et al. (2018, 2019) confirmed that increasing particle size leads to a decrease in the frequency (increasing relaxation time) at which the maxima is observed for a polarizing particle. Mellage et al. (2018) also outlined effects due to pores in the 10^{-3} to 10^{-1} Hz, surface roughness in the 10^{-1} to 10^{3} frequency range, and dielectric effects at greater than 10^{3} Hz. More importantly, the geometry of minerals in the subsurface can affect the diffusive flow of ions along the EDL (Chuprinko and Titov 2017; Marshall and Madden 1959). Each system must be carefully characterized to determine which factors control the SIP response. For example, a strong correlation between imaginary conductivity and permeability has been demonstrated for unconsolidated sediment samples while the electric formation factor was most important for predicting permeability in sandstone samples (Weller et al. 2013).

1.1.2 Detection of Amendments by SIP

SIP techniques have been used primarily at the laboratory scale (a summary of the few field-scale demonstrations is included in Section 1.1.3), to monitor changes induced by remediation. Changes in the phase shifts, imaginary conductivity, and chargeability terms have been correlated with the complex processes occurring during remediation. For example, addition of a particulate amendment like zero valent iron (ZVI) will cause changes in the aqueous and solid phase of subsurface materials due to oxidative dissolution and secondary precipitation of iron phases, formation of reducing conditions, and reductive dissolution of Fe phases. In some cases, the phase shift may also be impacted by the delivery or carrier solutions used for delivery of an amendment. For example, Shi et al. (2015) noted an increase in the phase shift for ZVI in sand when ZVI was first coated with mineral oil for delivery. For remediation technologies that stimulate microbial growth, the changes in SIP signal are generally lower for microbial cell-fluid interface as compared to metallic minerals (Ntarlagiannis et al. 2005; Williams et al. 2009) and should be considered for amendment technologies that may result in microbial growth.

Overall, there is a need to determine the threshold for detection of different materials and complex reactions occurring *in situ* during and after amendment application as described in Sections 1.1.2.1 and 1.1.2.2. These will be compared across amendments and frequencies at which signals are most significant, with Table 1.1 representing observations from peer-reviewed literature.

1.1.2.1 Detection of Minerals Formed during *In Situ* Remediation

The potential for detection of mineral phases is dependent on their polarizability or the effect of the precipitation of targeted minerals by amendments as they coat natural mineral phases and alter physical properties (e.g., porosity). Insulating mineral phases are associated with smaller signals (e.g., apatite and calcite). For example, laboratory experiments have primarily shown that calcite precipitation in porous media may generate phase shifts (< 4 mrad) in the low-frequency range (< 1 Hz) (Saneiyan et al. 2018; Wu et al. 2010). Shifts were observed at lower frequencies when larger particles were formed (< 0.01 Hz – based on precipitation in Ottawa sand versus a sand/clay mixture) (Saneiyan et al. 2018). All lower frequency shifts in SIP were attributed to changes in surface area with some electrochemical polarization of the EDL observed during calcite particle growth at higher frequency (500 Hz) (Wu et al. 2010). Note that no literature has been located investigating SIP detection of apatite, but signals similar to calcite are expected.

ZVI and sulfur modified iron (SMI) are potential amendments used to reduce and immobilize redox active contaminants in the subsurface. ZVI is metallic iron (Fe^{0}) and SMI is prepared by reacting ZVI with lower valence states of sulfur. Due to the significantly greater polarization and conduction capacity of iron minerals, there is more literature investigating their detection with SIP. ZVI has been observed via SIP based on an increase imaginary conductivity above 0.1 Hz (Abdel Aal et al. 2014; Joyce et al. 2012; Mellage et al. 2018; Orozco et al. 2015; Slater et al. 2005; Wu et al. 2005). Although direct measurements of SMI were not found in literature, there is a growing body of work on SIP detection of sulfide minerals

(Orozco et al. 2011; Placencia-Gómez et al. 2013; Williams et al. 2009). Iron sulfides have been primarily observed at low frequency (≤ 1 Hz) with a greater magnitude than observed for ZVI (Orozco et al. 2011; Placencia-Gómez et al. 2013; Williams et al. 2009). Phase shifts up to 60 mrad were observed in column experiments where biomineralization of iron sulfides in sand was observed at frequency near 1 Hz (Personna et al. 2008; Williams et al. 2009) with a peak up to 100 mrad in columns packed with 8 wt.% of pyrite or pyrrhotite in sand (Placencia-Gómez et al. 2013).

Changes in SIP have also been observed during delivery and reaction of ZVI with sediments, including related oxidation-reduction and dissolution-precipitation reactions. Frequency-specific changes have been observed due to Fe(II) consumption and accumulation of iron sulfides based on stimulation of bio-reduction in the presence of sulfates (Mellage et al. 2018; Orozco et al. 2011; Williams et al. 2009). A higher solution ionic strength and smaller particle size (nanoparticles) has also been suggested to increase polarization above 100 Hz (Joyce et al. 2012) and was confirmed with modeling by Bücker et al. (2018, 2019), which showed that increasing particle size leads to a decrease in the frequency (increasing relaxation time) at which the maxima is observed for a polarizing particle. Iron oxide precipitation from ZVI oxidative dissolution primarily identified as magnetite and green rust has been shown to increase phase shift and imaginary conductivity (Wu et al. 2008). Orozco et al. (2011) also reported shifts associated with Fe(II) consumption across the range of their experiments, which were conducted from 0.25 to 4 Hz. However, the maximum increase in phase shift associated with Fe(II) consumption was observed from 10-100 Hz, although they did report an increase across the range of their experiments from 1-1000 Hz (Williams et al. 2009). For iron sulfides, the maximum phase shifts were observed at the lowest frequencies measured and were greater than shifts observed for iron-only reduction (Orozco et al. 2011; Williams et al. 2009). Frequency-dependent phase shifts that corresponded to changes in iron and sulfate reduction were also measured as a direct consequence of *in situ* bio-stimulation during acetate injections (Orozco et al. 2011; Williams et al. 2009). However, changes in Fe^{2+}, dissolved sulfide, and iron sulfide nanoparticles were observed, making it difficult to isolate controlling mechanisms with only select frequencies collected in the field.

Additional components used for particle delivery or secondary mineral phase formation may also impact the SIP response, including carrier solutions. For example, results with guar gum and poloxamer-coated iron suggest that the signal is decreased in the presence of carriers (P104 surfactant in this work) as it inhibits the ability of the iron to polarize (Mellage et al. 2018; Orozco et al. 2015), although the imaginary conductivity at 1000 Hz was directly correlated to the signal from increasing concentrations of poloxamer-coated superparamagnetic iron-oxide nanoparticles with R^2 values of 0.98 and 0.99 based on two columns experiments (Mellage et al. 2018). In addition, the formation of non-metallic calcite phases from groundwater components following pH increases triggered by OH^- production during Fe^0 oxidation may decrease phase shift, complicating the interpretation of signal changes with time (Wu et al. 2008; Wu et al. 2009).

1.1.2.2 Direct and Indirect Indicators of Microbial Activity

The most quantitative and mechanistic characterization of SIP signals has been proposed for detection of bacteria. SIP has been used for characterization of intrinsic electrochemical properties of bacterial cells, including the cell surface-electrolyte interface (Prodan et al. 2004). The low-frequency dependent responses of bacterial cells are associated with the polarization of the EDL and Stern layers that develop along the outer membrane of bacterial cells in contact with aqueous solutions due to their net negative surface charge (Abdel Aal et al. 2004; Atekwana et al. 2002; Revil et al. 2012; Zhang et al. 2014). Previous signals from bacteria have been observed at low frequencies (0.125 to 10 Hz) associated with phase shifts up to 2 mrad (Abdel Aal et al. 2009; Davis et al. 2006; Ntarlagiannis et al. 2005; Revil et al. 2012; Turick et al. 2019; Zhang et al. 2013).

Revil et al. (2012) and Zhang et al. (2014) have proposed a quantitative model to describe the SIP responses of bacterial cell suspensions and cells attached to saturated porous media. According to the model, the imaginary conductivity is proportionally responsive to the concentration of bacteria cells in suspension once the formation factor (F) of the porous media has been considered. By contrast, the real conductivity is insensitive to suspended cells but can provide information about the density of attached cells (biofilms), which can alter the surface conductivity and constrain pore spaces (Revil et al. 2012; Zhang et al. 2014).

Table 1.1. Comparison of frequencies (in Hz) at which SIP response has been observed for various amendments.

Frequency (Hz)	Type	References
0.05 - 100	Bacteria	0.1 - 10 Hz (Revil et al. 2012), 0.05 to 100 Hz (Revil et al. 2012; Zhang et al. 2014)
< 1.0	Surface area	Due to calcite precipitation (Saneiyan et al. 2018)
500, 2000	Calcite	Formation (500 Hz), maturation (2000 Hz) (Wu et al. 2010)
0.001 - 0.1	Clays	0.001 to 0.1 Hz (Szecsody et al. 2020a)
0.1 - 10	Adsorbed Fe^{2+}	0.1 - 10 Hz as produced with dithionite reductant - Szecsody 2020a; < 4 Hz - Orozco et al. 2011
0.001 - 0.1	FeS, FeS_2	0.001 to 0.1 Hz decrease as produced by calcium polysulfide reaction and addition of minerals (Szecsody et al. 2020a) increase at 0.001-0.1 and < 100 Hz (Orozco et al. 2011; Williams et al. 2009)
0.001 - 0.03	Structural Fe	Structural ferrous iron in 2:1 clays (Szecsody et al. 2020a)
5000	Zero valent iron	Nano-size (Abdel Aal et al. 2014; Szecsody et al. 2020a)

1.1.3 Field-Scale SIP for Remediation Monitoring

Most previous field SIP measurements have been conducted for mineral exploration. However, this section describes the growing body of work using SIP for remediation monitoring and characterization. Because field ER measurements often cannot differentiate changes induced by remediation activities from baseline heterogeneities, SIP has been successfully used to delineate regions of active remediation. Previous field applications successfully observed changes in IP signals during bio-reduction by injection of acetate (Orozco et al. 2015), microbe-induced carbonate precipitation (Saneiyan et al. 2019), and detection of organic plumes (Ntarlagiannis et al. 2016). Maximum signal shifts observed are up to 80 mrad phase shifts and 5 mS/m imaginary conductivity, which have represented a change of up to 500% as compared to baseline phase shifts prior to remediation, as summarized in Table 1.2.

SIP applications in field settings have identified opportunities for improvement in the following areas: scaling up, frequency range, and inversion methods (Orozco et al. 2015, 2011; Saneiyan et al. 2019; Williams et al. 2009). There is also a need to extend applications to additional remediation technologies in the field. Previous SIP experiments have used small-scale (1-meter electrode spacings, up to 30 electrodes per array) surface arrays with different types of electrodes, including copper sulfate, stainless steel, silver chloride, and graphite (Orozco et al. 2015, 2011; Saneiyan et al. 2019; Williams et al. 2009). In addition, these data have been limited in the range of frequency (0.125 to 4.0 Hz), with the acknowledgement that it is critical that future field studies expand this range (Orozco et al. 2015, 2011; Williams et al. 2009), although higher frequencies may lead to induction coupling problems (Sogade et al. 2006). There is also a need to develop improved methods of SIP inversion that increase resolution and reliability of final images (Saneiyan et al. 2019).

Previous characterization and monitoring applications have focused primarily on detection of highly conductive and polarizable materials (e.g., iron sulfides) with recent work delineating the impacts of insulating materials (e.g., calcite) (Saneiyan et al. 2019). For example, Orozco et al. (2015) measured SIP signals from guar gum coated, micron-sized iron materials into a 1.5-m^3 volume of the subsurface with shifts of up to 80 mrad and imaginary conductivity up to 5 mS/m. In the short term (up to 12 hours after the last injection), changes in signals were modest (25% for phase shift and 10% for electrical conductivity). In some regions, a slight decrease (10%) in conductivity was observed with a reduction in porosity. A reduction in polarization was also observed in some regions and was suggested to be due to accumulation of guar gum coated iron on sediment surfaces, decreasing electrical conduction and polarization. This was further correlated with laboratory measurements highlighting a decrease in zeta potential (or the electrical potential at the slipping plane, which is generally within the diffuse layer of the EDL) with guar gum coatings.

Orozco et al. (2011) also conducted a 2-year experiment monitoring the impacts to the subsurface during bioremediation with phase shifts of up 40 mrad. Up to 88 days after the short-term injection (31 days), phase shifts decreased to < 5 mrad across the injection area as measured at 1 and 4 Hz. Phase shifts increased significantly following the second round of acetate injection for 110 days where, after day 450, phase shifts were > 40 mrad and persisted over time, with the greatest shifts observed at low frequency (0.25 Hz) and correlated with iron sulfide formation. In addition, increases in Fe(II) correlated with increases in phase shift ($R^2 > 0.94$) and imaginary conductivity ($R^2 > 0.95$) across all frequencies. Williams et al. (2009) observed increases at 0.125 and 1.0 Hz near the zone of injection of acetate to stimulate microbial reduction, although the difference in the magnitude of the phase response as compared to the initial conditions was greater at 1.0 Hz. Moreover, increases of up to 125% of the baseline phase shift (max of 16 mrad) were directly correlated with regions that observed an accumulation of electroactive ions and precipitation of sulfide minerals. Although frequency-specific shifts were not correlated to changes in the field experiments, a companion column experiment showed that increases in aqueous Fe(II) correlated with broad increases across frequency (1 to 1000 Hz) while increases in sulfate reduction were more significant at low frequency.

Recent work by Saneiyan et al. (2019) has also considered the impact of microbe-induced calcite precipitation on changes in SIP following injection of sugarcane molasses to stimulate bacteria, followed by urea injection to promote calcite bio-mineralization over 15 days. They observed a 500% increase in imaginary conductivity (max of 6 mrad for phase shifts) in comparison to only a 30% increase in real conductivity relative to the baseline, with significant impacts observed beginning at 6 days after injection. However, the specific frequency at which these observations were made was not reported as data were collected in the time domain, although they correlate with low frequency (Fiandaca et al. 2017).

These previous field applications show that there is significant potential for SIP to help address critical characterization and monitoring problems. This work will measure SIP response to a broader range of amendments and remediation technologies than previously considered, including redox-active particulate amendments (ZVI and SMI) as well as amendments that exhibit strong sorption and/or co-precipitation of contaminants (calcite, apatite, and bismuth). The amendment technologies tested in this report are currently under consideration for remediation of the Hanford Site's Central Plateau based on a previous review of available technologies for deep vadose zone remediation (DOE/RL 2019). Due to the limited frequency range of current field application configurations and technologies as summarized in Table 1.2, this work focuses on lower frequency applications (< 100 Hz).

Table 1.2. Summary of field experiments monitoring remediation with SIP.

Monitoring Period (days)	Electrode Spacing (m)/ # of electrodes	Frequency Range (Hz)	Maximum Phase Shifts (mrad)	Remediation Technology	Reference
0.5	1/30	0.125	80	Injection of guar gum coated iron	Orozco et al. 2015
15	1/24	0.125, 1, 10	16	Injection of acetate to stimulate bio-reduction	Williams et al. 2009
57	1/30	0.25 to 4.0	40	Injection of acetate to stimulate bio-reduction	Orozco et al. 2011
730	1/24	NM	6	Injection of molasses and urea to stimulate bio-precipitation of calcite	Saneiyan et al. 2019

NM – not measured

2.0 Materials and Methods

2.1 Materials

2.1.1 Amendment and Porous Media Materials

The amendments listed in Table 2.1 were tested via SIP in the laboratory and include ZVI, SMI, calcite, bismuth, and apatite. X-ray diffraction (XRD) analysis was conducted for these amendments as shown in Table 2.2 to confirm intended mineral phase and purity and to correlate changes in mineralogy with SIP changes. Full XRD methods and patterns as well as mineral synthesis methods for select amendments are summarized in Appendix A, Section A.1. Two different types of porous media were used in column experiments, including Hanford formation sediments from the Pasco Gravel Pit in Pasco, WA, and high-purity silica sand commercially available from Unimin Corporation (Accusand 40 – 60 mesh). The mineral surface area and compositions from Brunauer – Emmett – Teller (BET) and XRD, respectively, for both sediments are shown in Table 2.3.

Table 2.1. Summary of amendments tested in the laboratory.

Amendment	Description	BET Surface Area (m^2/g)[a]	Vendor or Lab-Synthesized
Zero valent iron – 1 (ZVI)	< 44 µm	0.852 ± 0.081	Hepure (target)
Zero valent iron – 2 (ZVI-2)	1 – 5 µm	0.729 ± 0.005	Ashland
Zero valent iron – 3 (ZVI-3)	44 µm	0.206 ± 0.055	Alfa Aesar (325 mesh)
Zero valent iron – 4 (ZVI-4)	74 µm	0.061 ± 0.010	Alfa Aesar (200 mesh)
Zero valent iron – 5 (ZVI-5)	149 µm	1.705 ± 0.013	Hepure (Flow)
Zero valent iron – 6 (ZVI-6)	841 µm	0.093 ± 0.004	Alfa Aesar (20 mesh)
Zero valent iron – 7 (ZVI-7)	10 µm	0.367 ± 0.002	Alfa Aesar (< 10 µm)
Zero valent iron – 8 (ZVI-8)	6-10 µm	0.410 ± 0.004	Alfa Aesar (6-10 µm)
Sulfur modified iron (SMI)	0.841 – 0.297 mm	1.544 ± 0.006	Veolia
Calcite	$CaCl_2$ + $NaCO_3$	0.256 ± 0.002	Synthesized
Bismuth	Sub-nitrate	0.86[b]	Sigma Aldrich (B0426)
Apatite – 1 (Abiotic apatite)	Hydroxyapatite	55.86 ± 0.11	Sigma Aldrich (289396)
Apatite – 2 (Bio-apatite)	Bio-precipitated	94.44 ± 0.05	Synthesized

(a) BET surface area conducted in triplicate.
(b) As reported in Cordova et al. 2020.

Table 2.2. Summary XRD results for amendments.

Amendment	Description
Zero valent iron – 1 (ZVI)[a]	78.8% iron, 9.0% magnetite, 7.8% quartz, and 4.4% wustite
Zero valent iron – 2 (ZVI-2)	NA
Sulfur modified iron (SMI)[a]	60% iron, 33% magnetite, 7% FeO
Calcite	99% calcite, 0.8% sodium chloride
Bismuth[b]	100% bismuth oxide nitrate hydroxide hydrate, $Bi_6[NO_3]_5O[OH]_3[H_2O]_3$
Apatite – 1	100% hydroxyl-apatite
Apatite – 2 (Bio-apatite)	99% hydroxyl-apatite, 0.4% quartz

NA – not available
(a) As reported in Lawter et al. 2018.
(b) As reported in Cordova et al. 2020.

Table 2.3. Summary of porous media materials utilized in experiments.

Material	Description	BET Surface Area (m^2/g)[a]	XRD (semi-quantitative)
Sand	40 – 60 mesh	0.160 ± 0.003	59% quartz, 41% feldspar
Hanford	< 2 mm	3.70 ± 0.37	42% quartz, 40% feldspar, 10% mica, 6% pyroxene, 1.2% chlorite

(a) BET surface area conducted in triplicate.

2.1.2 Columns and Equipment

Custom-built columns were constructed with end caps and side ports to accommodate Ag-AgCl electrodes for the collection of geophysical data. Briefly, the columns were 1.27 cm (1/2 in.) inner diameter (ID), schedule 80, clear polyvinyl chloride (PVC) with a body length of 8 cm (3.15 in.) or 61 cm (25 in.), as shown in Figure 2.1. A conventional Wenner array with a four-electrode design was used for all data collection on 8.0-cm length columns (Seidel and Lange 2007), while 61-cm length columns allowed for collected of data across more pairs of potential electrodes with different sediment layers. Threaded end caps were constructed from polyethylene terephthalate (PET) plastics. All electrodes were prepared from 1.6 mm (1/16 in.) Ag-AgCl wire (Ag wire reacted with NaOCl for > 48 hours) with straight wires inserted into Nylon tubes and 3.18 mm (1/8 in.) to 6.35 mm (1/4 in.) polyether ether ketone (PEEK) fittings for potential electrodes spaced equidistant along the column body and coiled wires used as current electrodes inserted into the end caps (Figure 2.2). The electrodes were connected to coaxial cables with radio frequency fittings (brass, 50 Ω, Amphenol Manufacturer, Wallingford, CT).

To reduce the possibility of electrode polarization, potential electrodes were placed approximately 1.27 cm (1/2 in.) from the column (from the surface where the sediments contact the column body) or twice the ID of the cable gland with porous Nylon placed inside the connection for the potential electrodes (Huisman et al. 2016; Zimmermann et al. 2012). This design allowed for exchange of pore solutions with potential electrodes without interaction with the current injected through the sediments within the column. In addition, based on previous publications, potential electrodes were placed at least twice the diameter from the current electrodes in the end cap and at least 2-3 cm apart (Kemna et al. 2012; Zimmermann et al. 2008b). All measurements were collected using a portable SIP unit (Ontash and Ermac) (Figure 2.3).

In preparation for future experiments under unsaturated conditions, a new design was tested to allow for increased contact between electrodes and sediments in low water content conditions. These preliminary results are presented in Appendix C.

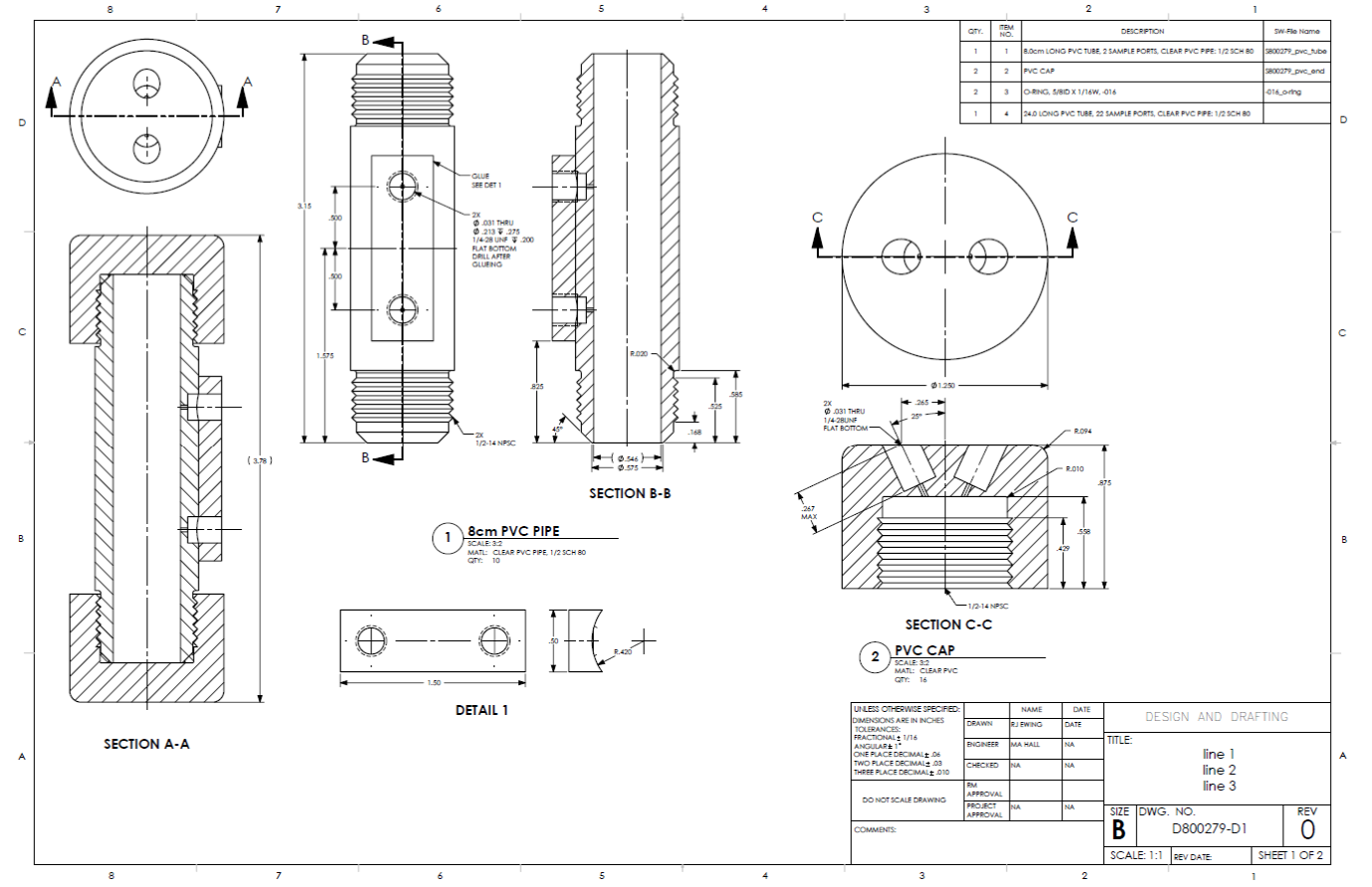

Figure 2.1. AutoCAD schematic of the column design.

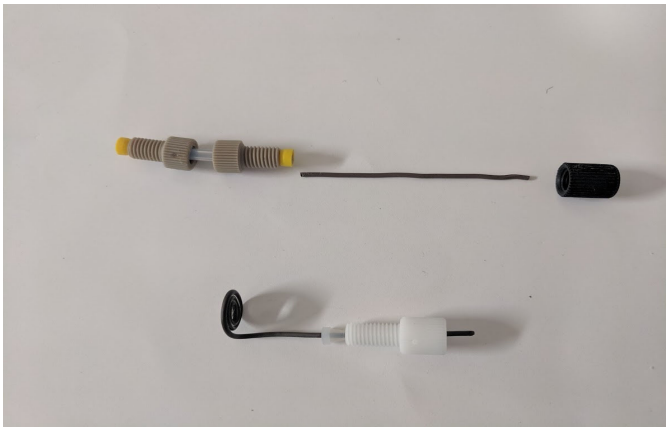

Figure 2.2. Electrode design with top representing potential electrodes installed along the column body with Ag-AgCl wire from associated PEEK fittings and bottom representing the current electrodes installed in end caps with Ag-AgCl wire and associated PEEK fittings.

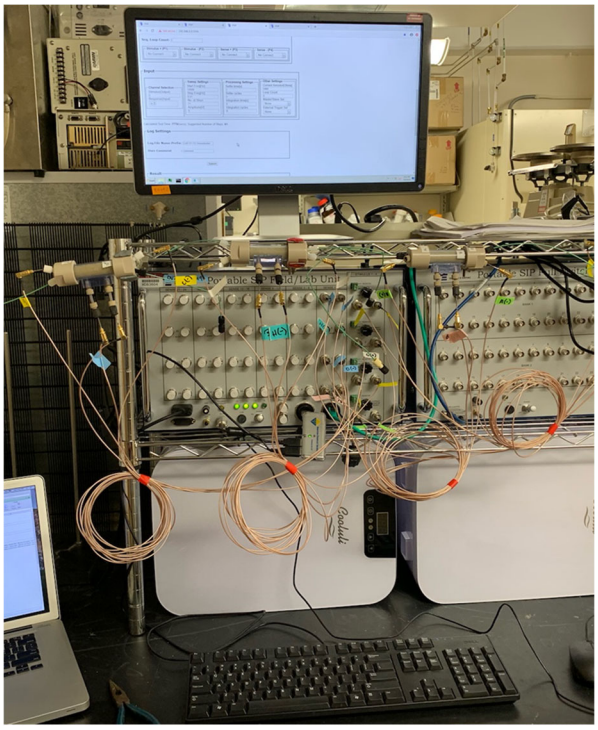

Figure 2.3. Photograph of SIP unit with attached cables that are connected to electrodes via radio frequency fittings.

2.2 Spectral Induced Polarization

2.2.1 Geometric and Intrinsic Factor Calculations

The following equations were used to calculate the geometric factor, *k*, for the columns with estimated factors summarized in Appendix B (Table B.3). Based on Eq. (2.1), a linear regression is used to calculate the geometric factor following the measurement of resistance (impedance, ohms) in columns filled with solutions of varying ionic strength: 0.001, 0.01, 0.05, 0.1, and 1.0 M NaCl. The complex resistivity of the solution was converted from a measurement of the conductivity of each solution at 20°C via electrode and meter (Orion 4Star meter with Orion 013005MD electrode) calibrated daily with certified standards (Inorganic Ventures). These measurements were independently validated using Eq. (2.2) to calculate the complex resistivity of the solution based strictly on the physical dimensions of the column.

$$\rho = k \times R \tag{2.1}$$

where R = complex resistance or impedance (ohms), ρ = complex resistivity (ohms·cm), k = geometric factor (configuration specific, cm).

$$R = \frac{L \times \rho}{A} = \frac{L \times \rho}{\pi r^2} \tag{2.2}$$

where L = column length (cm), A = column area (cm^2), and r = column radius (cm).

Further, the intrinsic electrical formation factor, *F*, was computed using Eq. (2.3) for columns packed with sand and Hanford formation sediments. This factor describes the dependence of the bulk resistivity (ρ) to the resistivity of the fluid filling the pore space (ρ_w); this dependence is a function of porosity and

the connectivity of the pore space, as described by a cementation exponent. This factor was independently measured for variable ionic strength solutions and regression analysis was used to describe the relationship between the inverse measured bulk resistivity and the inverse of the solution resistivity. It allows for measurement of the surface resistivity of the porous material based on the *F* factor.

$$\frac{1}{\rho} = \frac{1}{F\rho_w} + \frac{1}{\rho_s} \tag{2.3}$$

where ρ = measured complex resistivity (ohms·cm), ρ_w = solution resistivity, ρ_s = matrix resistivity, and *F* = intrinsic formation factor.

Calculated formation factors for sand and Hanford formation sediments are summarized in Appendix B (Table B.2 and Table B.3, respectively) based on Eqs. (2.1) and (2.3) with calculations using multiple frequencies based on Eq. (2.2). These results highlight that the method of estimation of the geometric factor based on the sample holder geometry (L/A) provides similar estimation factors based on regression measurements collected at variable ionic strength (across four orders of magnitude), although the variable ionic strength measurements allow for a more accurate correction for each column. Further, it should be noted that both factors are theoretically independent of frequency. This independence is confirmed as summarized in Figure B.1 and Table B.4 in Appendix B.

2.2.2 Resistivity and Conductivity Relationship

The complex conductivity (σ, S/cm) is the inverse of the complex resistivity (ρ, Ω-cm) based on Eq. (2.4). Real and imaginary conductivity can then be calculated from Eqs. (2.5) through (2.7). The real conductivity was described further using Eq. (2.8) to distinguish surface conductivity from that of the bulk electrolyte (Abdel Aal et al. 2004; Garcia 2018; Joseph 2016; Binley and Slater 2020).

$$\sigma = \frac{1}{\rho} \tag{2.4}$$

$$\sigma = \sigma' + i\sigma'' \tag{2.5}$$

$$\sigma' = |\sigma| cos(\varphi) \tag{2.6}$$

$$\sigma'' = |\sigma| sin(\varphi) \tag{2.7}$$

$$\sigma' = \frac{\sigma_w{}'}{F} + \sigma'_{surf} = \sigma_{el}{}' + \sigma'_{surf} \tag{2.8}$$

where σ' is the real conductivity and σ" is the imaginary conductivity based on the measured impedance magnitude and phase. The F is the sediment intrinsic formation factor, σ_{surf}' is representative of the interfacial conductivity or conduction (transport) along the surface of grains and pore spaces, σ_w' is the solution conductivity, σ" is the result of diffusive polarization effects on the surface, and σ_{el}' is the electrolytic conductivity.

Moreover, the imaginary conductivity can also be written in terms of a frequency-dependent dielectric permittivity, although it reflects the quadrature component of the conductivity rather than a pure dielectric effect (Hao et al. 2015).

2.3 Amendment Testing Protocols

Amendments were packed into columns with Hanford formation sediments (< 2 mm size fraction) or sand (40-60 mesh, Accusand) at variable concentrations (0.1, 1.0, and 10 wt.% for most amendments – differences noted in Section 3.0). Each column was fully saturated with artificial groundwater (AGW) or artificial perched water (APW) (recipes in Appendix A) prior to collection of data. SIP measurements were collected from 0.001 to 10,000 Hz with 71 datapoints or 0.01 to 1,000 Hz with 51 datapoints across the frequency range, with 10 measurements for each order of magnitude in phase shift across frequencies. All SIP runs were collected in triplicate (via three loops across the range of frequencies) and many columns were also prepared in triplicate. Further, a conductance meter and electrode were used with certified standards (Inorganic Ventures) to measure the conductivity (µS/cm) for aqueous solutions injected into the columns. SIP measurements were collected immediately after packing and saturating with select samples monitored over time (up to 77 days). Select samples were also analyzed for pH (Fisherbrand Accumet 13-620-183A electrode and Orion Star meter), dissolved oxygen (Thermo Orion DO 081010 electrode and Orion model 810 meter), redox potential (Mettler Toledo Pt 4865-50-90-K9 electrode with Fisher Accumet XL150 meter), and total Fe, Ca, P, Na, and K by inductively coupled plasma optical emission spectrometry as described in Section A.3.1 in Appendix A.

All experiments in 8-cm columns were conducted under static conditions (no flow) with injection of solution only upon sampling. However, experiments conducted in 61-cm columns were subjected to continuous flow conditions unless specified – an additional description of experiments in 61-cm columns is included in Section 3.2.1.5 for testing *in situ* formation of bioapatite, Section 3.2.1.3 for testing *in situ* formation of apatite from polyphosphate, and Sections 3.4.3 and 3.4.4 and Appendix A, Section A.3.1, for dual amendment testing with SMI and subsequent treatment by calcite or apatite forming solutions. In addition, one set of experiments for *in situ* injection of particles was conducted with brass current and potential electrodes with 2.54-cm (1-in.) diameter PVC columns of 30.5 cm (12 in.) in length (Section 3.3.1.3) for *in situ* injection of ZVI with xanthan gum as a carrier solution. The design of potential electrodes was identical to the previous description with the exception of the material (brass as opposed to Ag-AgCl wire). Current electrodes in the end caps were replaced with a 60-mesh (250-µm) brass screen to allow for injection of micron-size particles without significant impacts to flow.

3.0 Results

SIP measurements were collected with varying concentrations of amendment (i.e., mass fraction) in silica sand and in Hanford formation sediments to determine if the amendments could be successfully detected at different stages of remediation with SIP. Amendments were either mixed with sediments after precipitation and packed into columns or delivered (*in situ*) to columns via particulate injection or mineral-forming solution injection. The primary focus is the phase shift and imaginary conductivity. In some instances, the real conductivity (or solution conductivity), which is a measurement primarily of the ionic strength of solutions, is changing over time with solution delivery and mineral formation. The SIP response to remediation amendment occurs at some time after the injection of a precipitate-forming solution (e.g., calcite- or apatite-forming solutions) depending on reactivity and subsequent changes to the solid surfaces. ZVI and SMI are not immediately redox reactive upon injection into porous media and can take days to weeks to form a rind of redox-reactive ferrous phases on the iron surface, which may impact their SIP signatures over time. Their chemical reactivity can also be impacted by carrier fluids (e.g., xanthan gum) used to increase injectability.

3.1 Silica Sand and Hanford Formation Sediment with No Amendments

For comparison to amendment additions, SIP measurements were collected on clean, untreated silica sand (Accusand) and Hanford formation sediment (Figure 3.1). The phase shift (i.e., phase angle) was significantly smaller for the silica sand, and both sand and sediment increased the phase shift as the frequency increased above 10 Hz. The imaginary conductivity of the Hanford formation sediment is one to two orders of magnitude greater than the sand at all frequencies, as expected. The greater difference between the sand and Hanford formation sediments at low frequency (< 0.1 Hz) may be due to increased electrical conductivity of clays with a maximum near 0.1 Hz based on previous work (Slater and Lesmes 2002; Szecsody et al. 2020a) as well as the heterogeneity in particle size and mineralogy of sediments as compared to the sand. This response is commonly observed in sediments, where the particle size and clay content have been shown to impact the baseline but may be inversely correlated (Mellage et al. 2018; Slater and Lesmes 2002). Modeling by Bücker et al. (2018, 2019) further confirmed that increasing particle size leads to a decrease in the frequency (increasing relaxation time) at which the maxima is observed for a polarizing particle. Due to the increased response and potential for Maxwell Wagner polarization and parasitic capacitive coupling with the SIP instrument (Wang and Slater 2019), the 95% confidence intervals (CIs) increased at higher frequency (i.e., greater variability between the SIP measurements on the three columns). In addition, the variability in the baselines for Hanford sediments was greater than the variability for sand, possibly due to increased heterogeneity with respect to both surface area and mineralogy with the sediments.

For amendment additions in subsequent sections, phase shift, real conductivity, and imaginary conductivity are shown along with normalized imaginary conductivity. The normalized imaginary conductivity is the amendment imaginary conductivity divided by the imaginary conductivity of the sediment with no additions. This normalization is used to highlight the differences with variable amendment concentrations added to sediment or sand after dividing by the baselines shown in Figure 3.1.

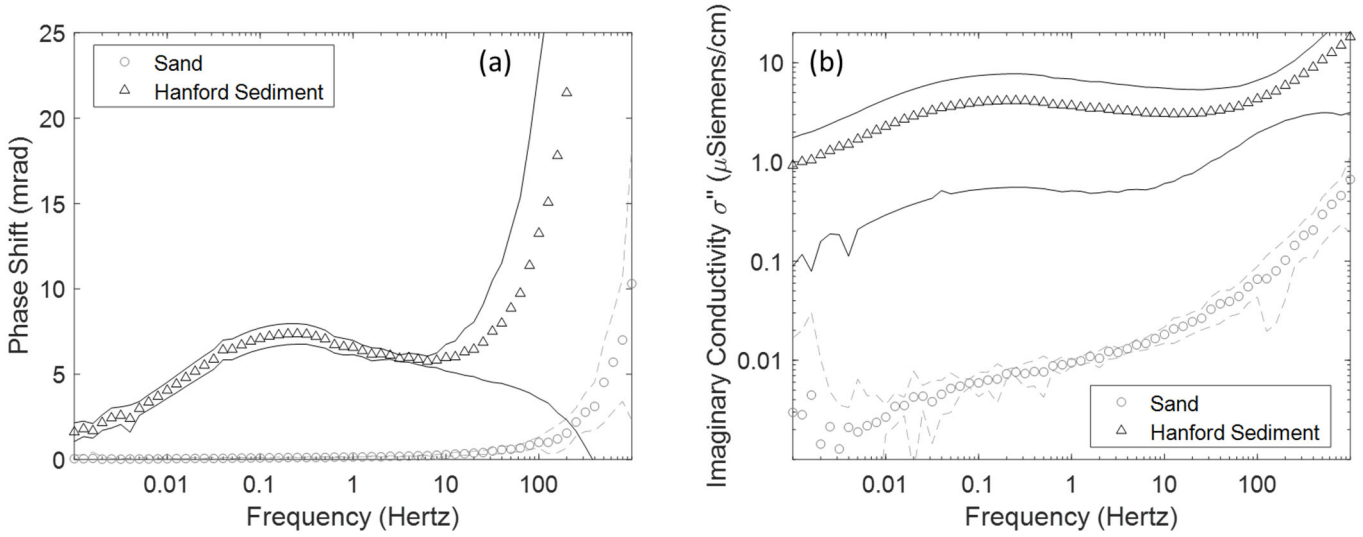

Figure 3.1. SIP response for sand and Hanford formation sediment with no amendment additions and saturated with either AGW or APW as depicted in the legend for (a) phase shift and (b) imaginary conductivity with respect to frequency (hertz), where *lines* represent 95% CIs for data collected for triplicate columns and *circles* represent the average response for each frequency. Note: 95% CIs removed for Sand + AGW in the imaginary conductivity (b) to simplify due to overlapping lines.

3.2 Low-Conductivity Amendment Materials

3.2.1 Apatite Amendments

3.2.1.1 Inorganic Apatite Mixed with Sand

Additions of a commercial apatite material (apatite – 1, Sigma Aldrich) at concentrations ranging from 1 to 10 wt.% in silica sand showed a shift in the phase and imaginary conductivity (Figure 3.2). The circles represent the average with each weight fraction of apatite. The phase shift for 10 wt.% apatite (black circles, Figure 3.2a) was 10 times greater than the untreated sand in the 0.1 to 10 Hz frequency range. The imaginary conductivity change was also greatest in the 0.1 to 10 Hz range, as was the corresponding change in phase shift (Figure 3.2b and c). The real conductivity was between 50 and 65 µS/cm for all wt.% of apatite and is primarily due to the solution conductivity of AGW as discussed in Section 2.2.

The imaginary conductivity better represents changes in surface conductivity and polarization [accounting for change in the real conductivity by separating the complex conductivity into real and imaginary – Eq. (2.5)]. Although the addition of apatite led to a decrease in phase shift and change in imaginary conductivity relative to the untreated sediment, the changes were not linearly related to the percent apatite nor were they consistent across the frequency range. The normalized imaginary conductivity more clearly shows the frequency range of change relative to the untreated sand. The 1 wt.%, 3 wt.%, and 5 wt.% apatite showed nearly the same change relative to the untreated sediment, and the 10 wt.% apatite showed a significantly greater change relative to the untreated sediment with a maximum near 5 and < 0.1 Hz. It is possible that the changes with addition of apatite are due to the different EDL of apatite particles as compared to sand due to their differing surface charges (Zhou et al. 2020) and particle sizes (Table 2.1 and Table 2.3), as well as the physical interactions between the two (e.g., blocking of pore throats with apatite) (Chuprinko and Titov 2017; Bücker et al. 2019).

Additional SIP measurements were collected with the same apatite added to sand columns, but saturated with APW, which has approximately four times greater ionic strength relative to AGW (ionic strength is 7.1 and 32.6 mmol/L for AGW and APW, respectively). A plot of the normalized imaginary conductivity shows a consistent increase in imaginary conductivity (Figure 3.3d) and phase shift (Figure 3.3a) with greater apatite content by weight in the 0.01 to 10 Hz range for apatite mixed with sand and saturated with both APW and AGW, although the 10 wt.% apatite data shows considerable noise above 10 Hz frequency. Overall, the results show that commercial apatite is detectable at 10 wt.% in sand with the greatest response at low frequency (< 0.1 Hz), which can be measured at field scale. These results show that detection of apatite alone is unlikely in a remediation setting except source locations with high concentrations delivered as most previous field injections resulted in less than 0.5 wt.% or 5 mg/g of apatite (Szecsody et al. 2020b, 2016; Vermeul et al. 2014).

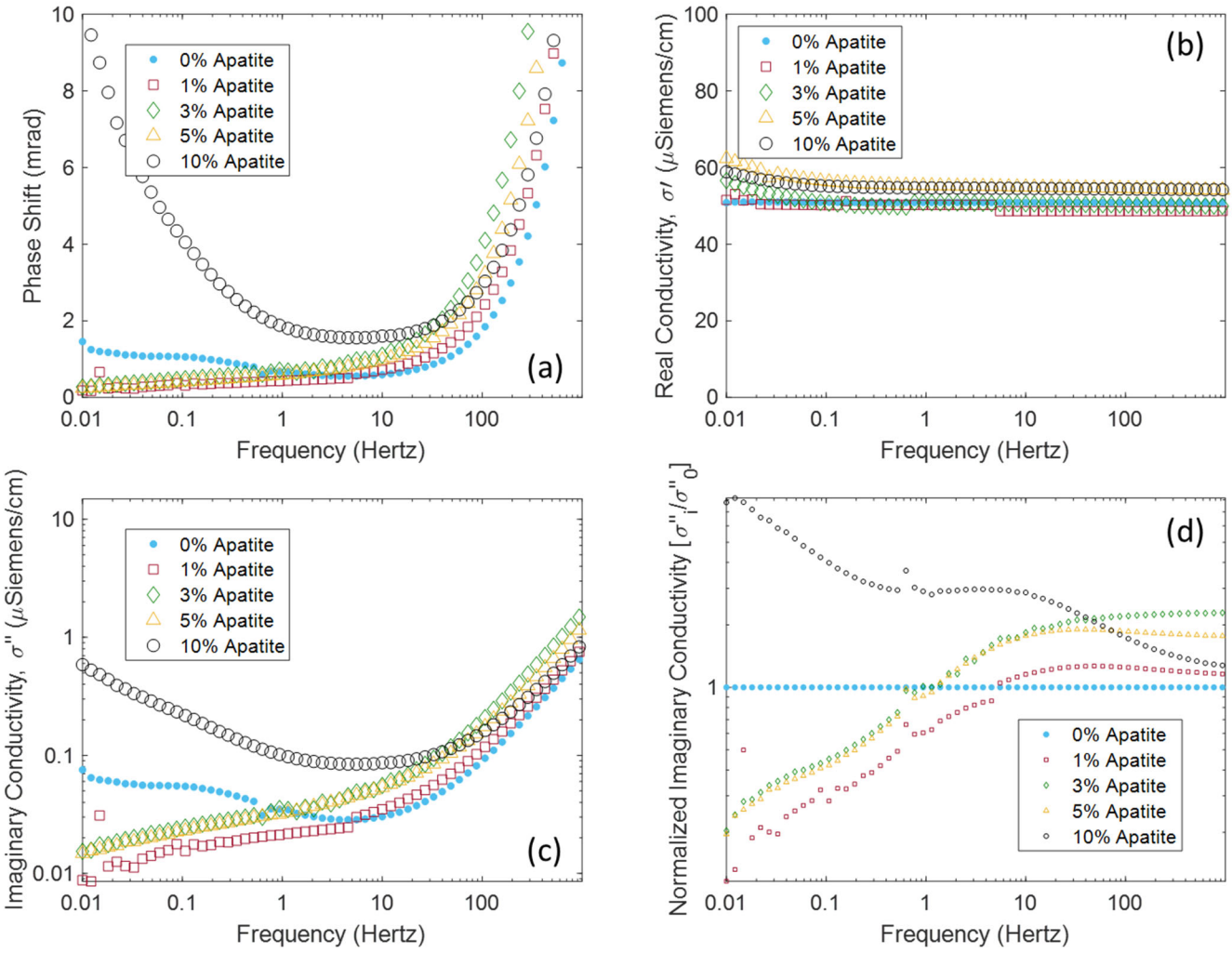

Figure 3.2. SIP response to apatite-1 (Sigma Aldrich) mixed at variable wt.% in sand saturated with AGW, as shown by (a) phase response, (b) real conductivity, (c) imaginary conductivity, and (d) normalized imaginary conductivity with respect to sediment without amendment where *circles* represent the average response for each frequency.

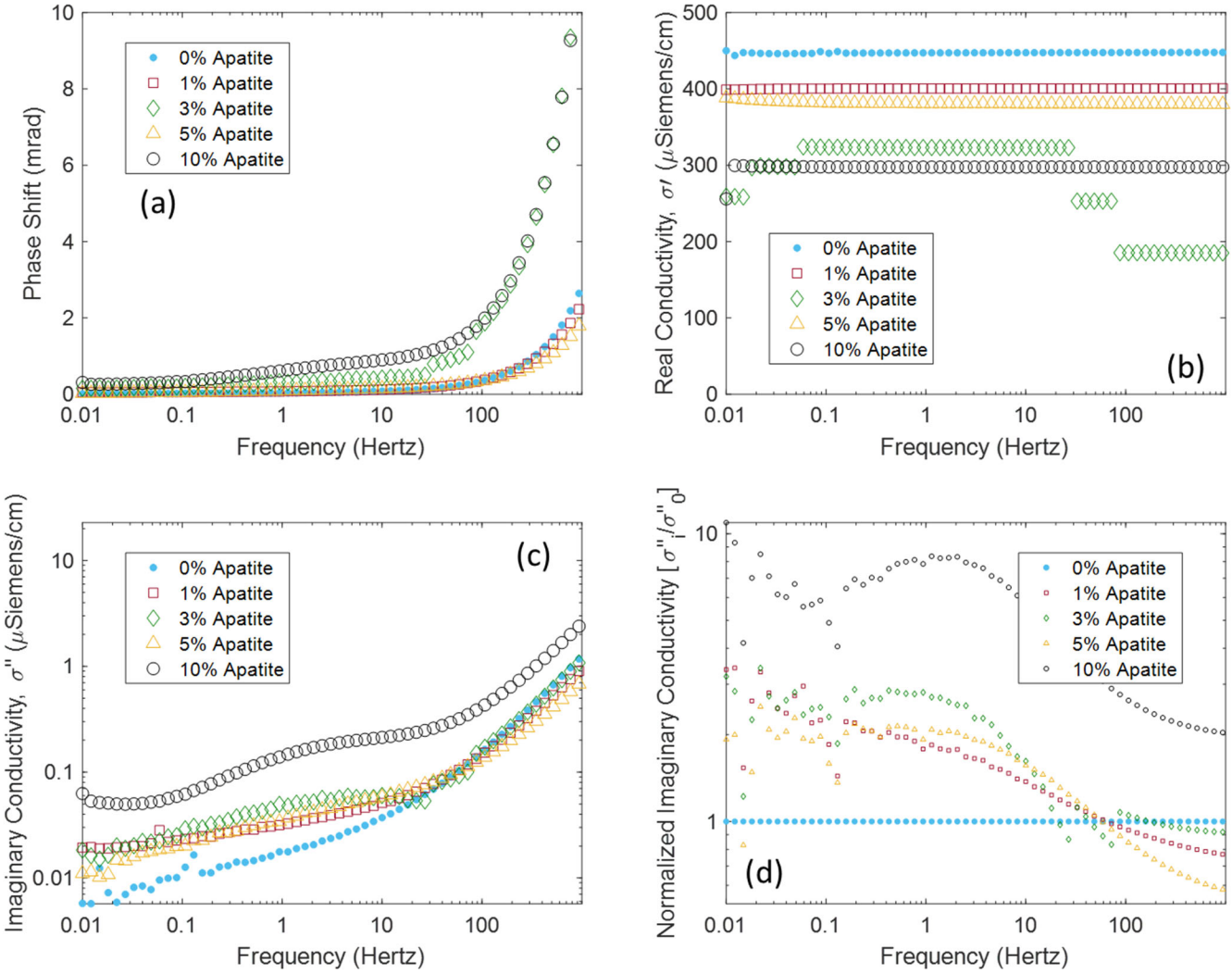

Figure 3.3. SIP response to apatite-1 (Sigma Aldrich) mixed at variable wt.% in sand saturated with APW as shown by (a) phase shift, (b) real conductivity, (c) imaginary conductivity, and (d) normalized imaginary conductivity with respect to sediment without amendment where *circles* represent the average response for each frequency.

3.2.1.2 Inorganic Apatite Mixed with Hanford Formation Sediments

Different percentages of apatite added to the Hanford formation sediment showed phase and imaginary conductivity shifts in the 0.01 to 1 and > 10 Hz frequency ranges (Figure 3.4). The lower frequency changes were similar to apatite additions to sand (Figure 3.2 and Figure 3.3), although the range of increase in imaginary conductivity was broader in the sand (< 10 Hz). The phase shifts show small increases with increasing apatite content (Figure 3.4a), although they are likely not significant within the error between the triplicate columns (see error on control sediments in Figure 3.1). Moreover, the imaginary conductivity shows differences between the 0.1 wt.% and 1 wt.% apatite additions, although there is a significant increase in the high and low frequency range for the 10 wt.% apatite (Figure 3.4b and c). The maxima for phase shift and imaginary conductivity for 10 wt.% apatite also shift to lower frequencies (0.5 to 0.05 Hz) and higher frequencies (> 10 Hz), highlighting both a low and high frequency change in SIP response. The normalized imaginary conductivity illustrates a similar trend, which increases over the frequency range of 1 to 0.01 and > 10 Hz (Figure 3.4d), although the greater

variability in the 10% apatite columns should be considered as the relative percent difference in the 95% CIs was approximately 65% and 130% for the low frequency (< 1 Hz) and high frequency (> 100 Hz), respectively, as compared to 8% and 12% for the three duplicate columns for 1 wt.% apatite (Figure 3.4c). However, these phase shifts and imaginary conductivity changes may differ in a more heterogeneous sediment or with the injection of a solution that precipitates apatite, as precipitates may preferentially coat high surface area clays, micas, and Fe oxides in sediment, all of which exhibit some capacitance (and phase shift) without amendments. Moreover, when apatite is mixed with sediment as opposed to precipitated in the presence of sediment, it may physically block some pore spaces and impact the surface conductivity by interacting with the EDL (Chuprinkov and Titov 2017). Although the low-frequency changes may not be differentiated from the baseline for the Hanford formation sediment based on relative signal, they may be differentiated based on the shift in peak maxima, which suggests a change in the characteristic time constant or chargeability (Binley and Slater 2020). In addition, there is potential to observe apatite in heterogeneous sediments at high frequencies (> 10 Hz). These results are different from observations for apatite in sand, which would likely be undetectable, highlighting the importance of understanding the SIP baseline signal from sediments.

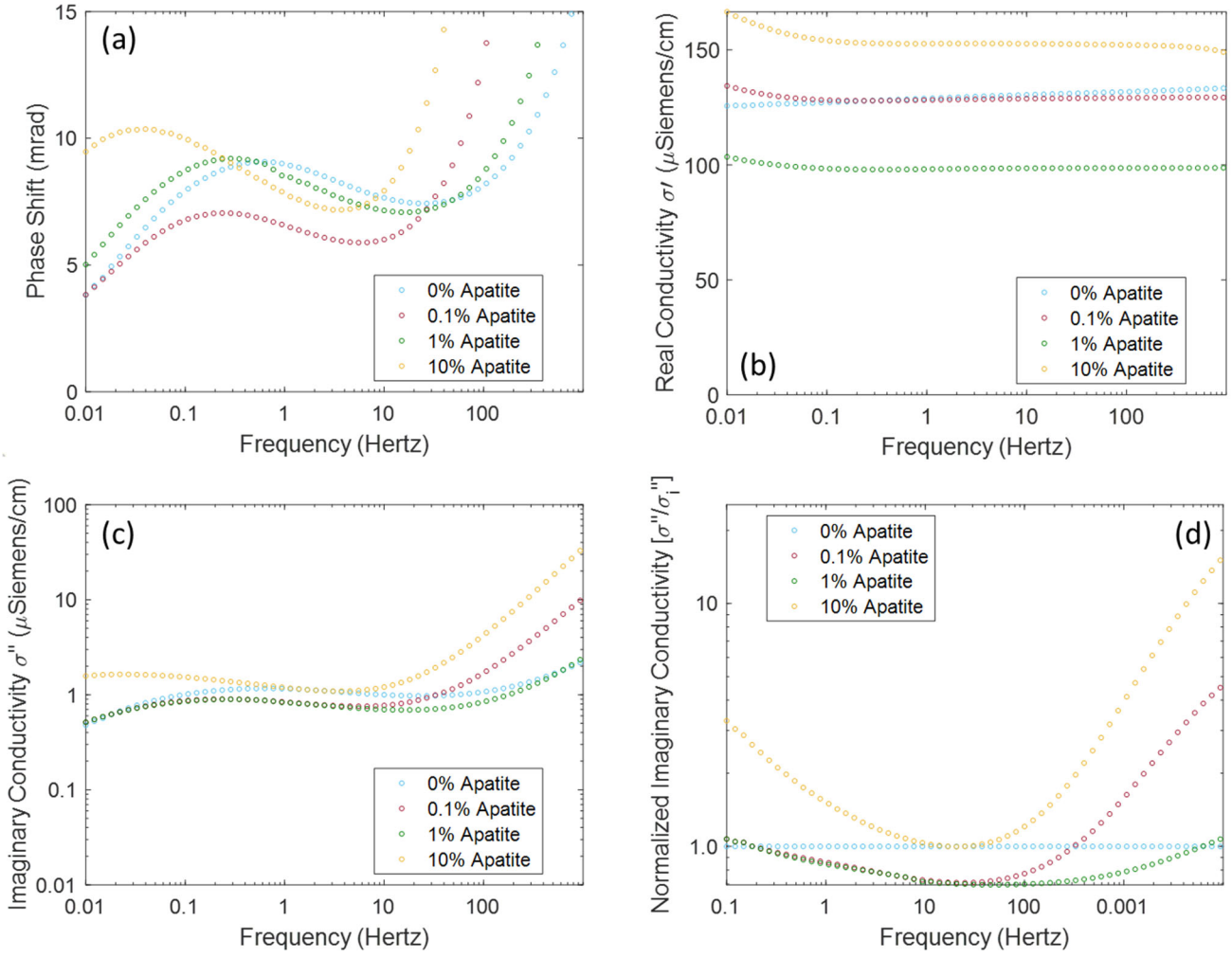

Figure 3.4. Apatite-1 (Sigma Aldrich) at variable wt.% in Hanford formation sediments saturated with AGW with (a) phase shift in mrad, (b) real conductivity, (c) imaginary conductivity in µS/cm, and (d) normalized imaginary conductivity with respect to sediment without amendment where *circles* represent the average response for each frequency.

3.2.1.3 Inorganic Apatite *In Situ* Formation in Laboratory-Scale Columns

For comparison with apatite mixed with sediments, apatite was also precipitated *in situ* in 24-in. length by 0.5-in. ID columns from polyphosphate solutions as described in Appendix A, Section A.1.5. After injection of polyphosphate solutions, SIP response was monitored for approximately 40 days as shown in Figure 3.5, Figure 3.6, and Figure 3.7 for data collected across multiple pairs of SIP electrodes as depicted in Figure 3.6. Then, the columns were flushed with AGW and monitoring continued up to 70 days with effluent monitoring summarized in Figure 3.8 and solid phase characterization in Table 3.1. The total P in extract 6 likely represents apatite as not enough Ca is removed in extract 5 for stoichiometric apatite. Loadings of P are relatively consistent throughout the column, suggesting an even distribution, which is consistent with SIP response for three potential electrode pairs across the column body. For all three SIP potential electrode pairs, the phase shifts decreased significantly after injection of polyphosphate solutions while the real conductivity and imaginary conductivity both increased.

A significant increase in real conductivity was observed, primarily due to the significant ionic strength of the polyphosphate solution (> 6000 µS/cm) as compared to AGW (< 300 µS/cm). However, as the column was static (no flow) for approximately 40 days after injection of polyphosphate, the decrease in real conductivity over time for all three electrode pairs suggests that apatite is slowly precipitating from the polyphosphate solution and consuming ions. Following flushing of the column with AGW, the real conductivity decreased significantly but was still approximately three times the initial solution conductivity and real conductivity as confirmed by effluent solution conductivity monitoring in Figure 3.8.

The changes observed with time in the imaginary conductivity were relatively smaller. However, after comparison of the three electrode pairs in Figure 3.5, Figure 3.6, and Figure 3.7 part C, the observed trend is similar to that observed for the real conductivity. Initially, the imaginary conductivity peak in the low frequency range was observed at approximately 0.3 Hz with a maximum near 0.3 µS/cm, indicating a relatively low surface polarization. Previous research has observed a maximum in this range of low frequency due to the presence of clays in sediments (Slater and Lesmes 2002; Szecsody et al. 2020a). Following injection of polyphosphate solutions, imaginary conductivity increases to approximately 0.6-0.7 µS/cm, likely due to both interaction of the high salt concentration with the EDL of sediments and formation of apatite on sediment surfaces.

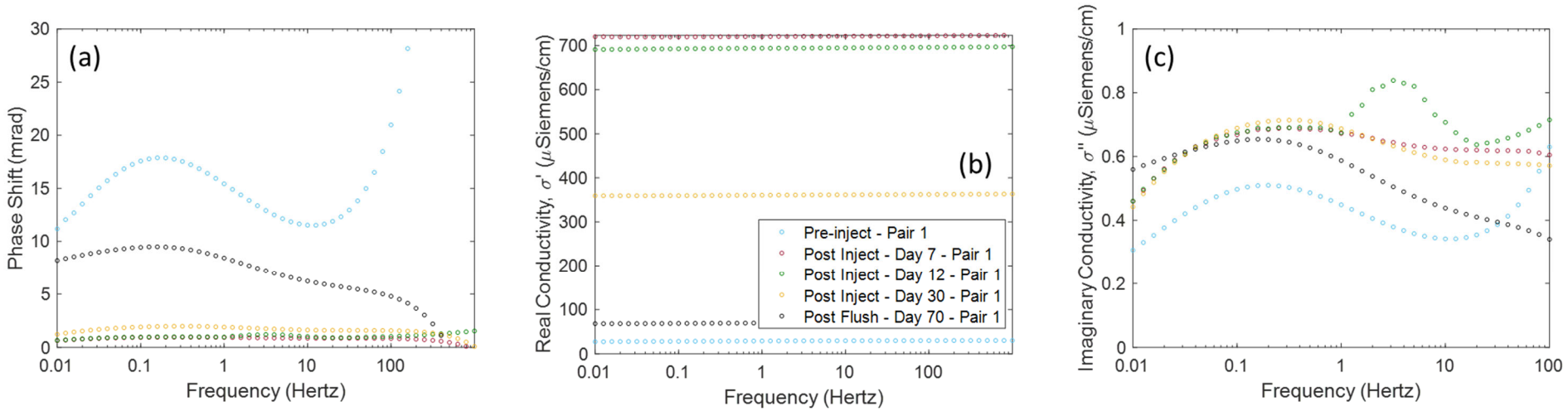

Figure 3.5. SIP results for electrode pair 1 for apatite-1 (inorganic apatite) formed *in situ* over time in 24-in. column packed with Hanford formation sediments and saturated with AGW and apatite-forming solutions with monitoring over time as (a) phase shift in mrad, (b) real conductivity, and (c) imaginary conductivity in µS/cm with respect to initial sediment without amendment (*open yellow circle*), where *circles* represent the average response at each frequency for three loops of data collected.

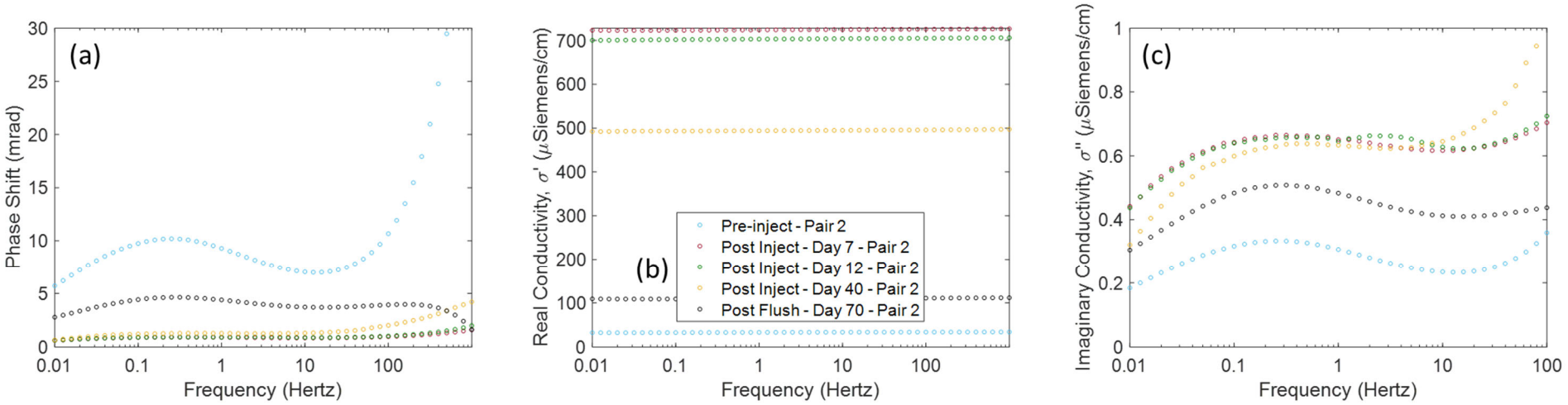

Figure 3.6. SIP results for electrode pair 2 for apatite-1 (inorganic apatite) formed *in situ* over time in 24-in. column packed with Hanford formation sediments and saturated with AGW and apatite-forming solutions with monitoring over time as (a) phase shift in mrad, (b) real conductivity, and (c) imaginary conductivity in µS/cm with respect to initial sediment without amendment (*open yellow circle*), where *circles* represent the average response at each frequency for three loops of data collected.

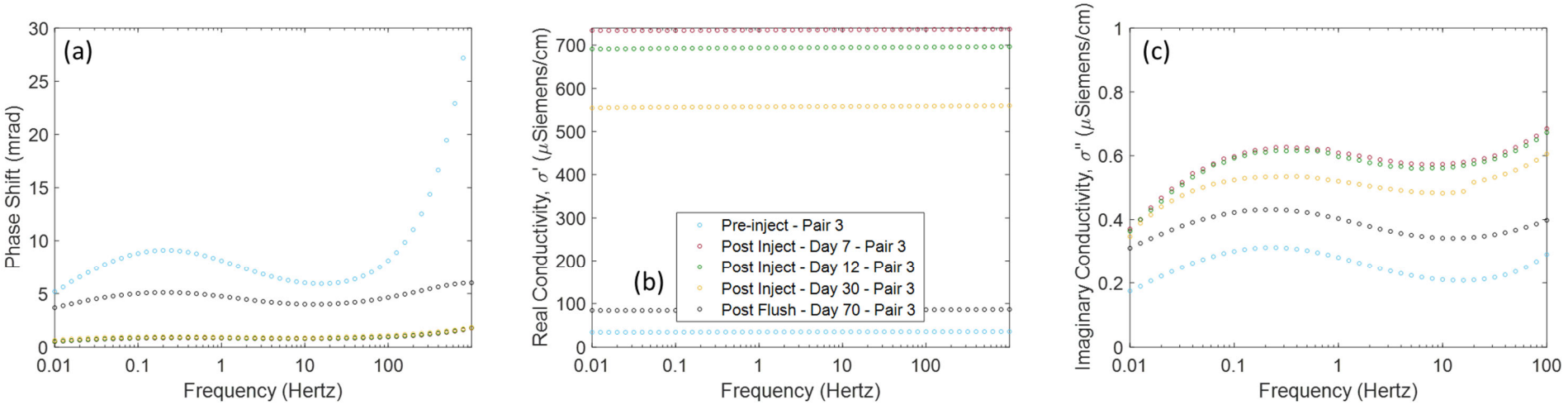

Figure 3.7. SIP results for electrode pair 3 for apatite-1 (inorganic apatite) formed *in situ* over time in 24-in. column packed with Hanford formation sediments and saturated with AGW and apatite-forming solutions with monitoring over time as (a) phase shift in mrad, (b) real conductivity, and (c) imaginary conductivity in µS/cm with respect to initial sediment without amendment (*open yellow circle*), where *circles* represent the average response at each frequency for three loops of data collected.

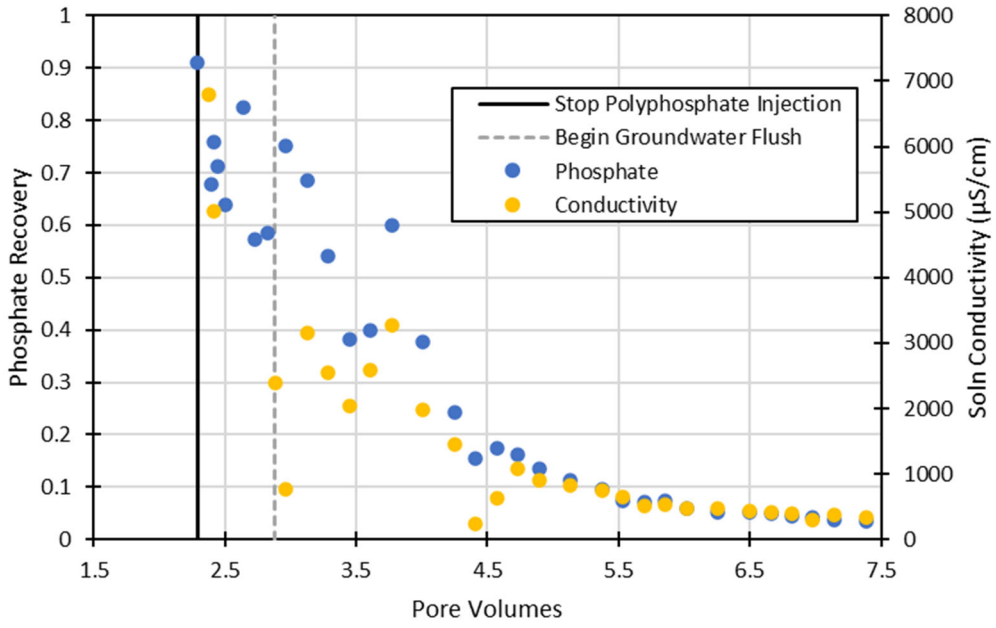

Figure 3.8. Results for effluent monitoring following equilibration of polyphosphate solutions with Hanford formation sediments in 24-in. column for one month and then flushing with AGW for up to 70 days.

Table 3.1. Summary of destructive characterization of polyphosphate column , including solid phase extraction of phosphorus (based on added P as compared to control Hanford sediment without polyphosphate treatment) and moisture content measurements following column sectioning after 70 days.

Column Location	Phosphorus (µg/g)		Phosphate (Ext 6) (wt.%)	Moisture Content (dry wt.%)
	Extract 5	Extract 6		
Inlet	624	772	0.24	28
SIP1	521	577	0.18	27
Space 1	433	662	0.20	28
SIP 2	503	709	0.22	28
Space 2	557	581	0.18	29
SIP 3	565	703	0.22	26

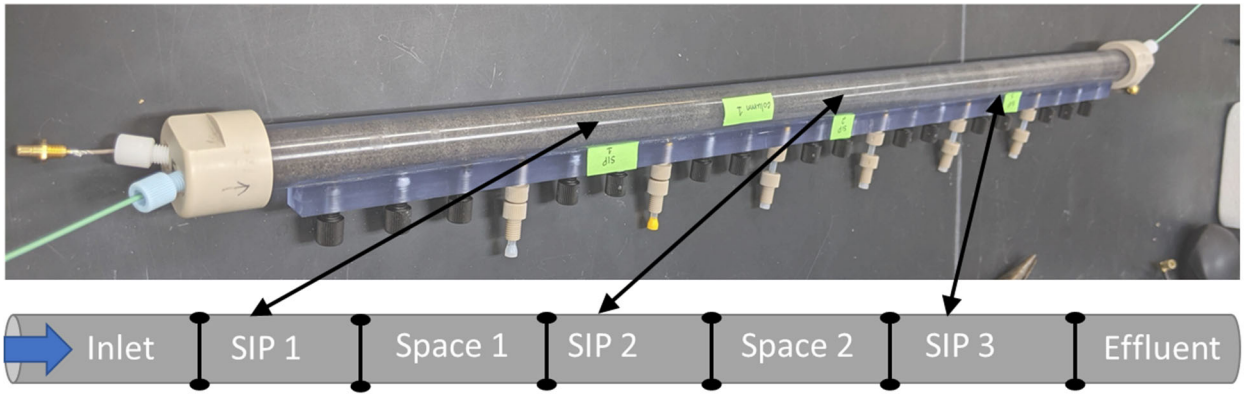

Figure 3.9. Depiction of column and electrode configuration for *in situ* precipitation of apatite from polyphosphate. Note: A similar configuration was used for biotic precipitation from calcium citrate and phosphate solution.

3.2.1.4 Biotic Apatite Mixed with Sand and Hanford Sediments

Apatite-2 was synthesized in the absence of sediments as described in Appendix A, Section A.1.4, for comparison with the apatite-1 standard (Sections 3.2.1.1, 3.2.1.2) and apatite formed *in situ* by polyphosphate (Section 3.2.1.3). The phase shift for 3 wt.% apatite-2 (Figure 3.10a) was < 1.0 mrad over the 0.001 to 10 Hz frequency, which was similar to the phase shift (< 1.1 mrad) over the 0.01 to 10 Hz frequency range for 3 wt.% apatite-1 mixed with sand (Figure 3.2a). Moreover, similar values were observed for imaginary conductivity for apatite-1 and apatite-2 at 1 wt.%. These results suggest that the corresponding changes are similar for apatite-1 and apatite-2 (Figure 3.10b and Figure 3.2b) in the low frequency range, although their genesis and particle size are different (56 vs. 94 m^2/g for apatite-1 versus apatite-2, respectively). However, the increase in higher frequency should be noted for apatite-2.

The 0.5 and 3 wt.% apatite-2 additions to Hanford formation sediments showed a 10 to 15 mrad decrease in the 0.01 to 10 Hz frequency range that was significantly greater than the 95% CIs (*not shown* but less than 27% below 100 Hz, Figure 3.11a) based on data collected for triplicate columns. Apatite-2 in Hanford formation sediment also showed greater SIP phase shifts (Figure 3.11a) compared to addition to sand with maximum phase shifts of approximately 14 mrad as compared to 0.6 mrad in the range of 0.001 to 10 Hz (Figure 3.10a). These phase shifts were somewhat greater than for the abiotic apatite (Figure 3.3a) to Hanford sediment. The difference may be due to the higher surface area for the biotic apatite (94 m^2/g) relative to the abiotic apatite (56 m^2/g), although it is unclear why this trend was not observed in the sand mixed with apatite-1 and apatite-2 and may be related to a different secondary interaction with the sediments.

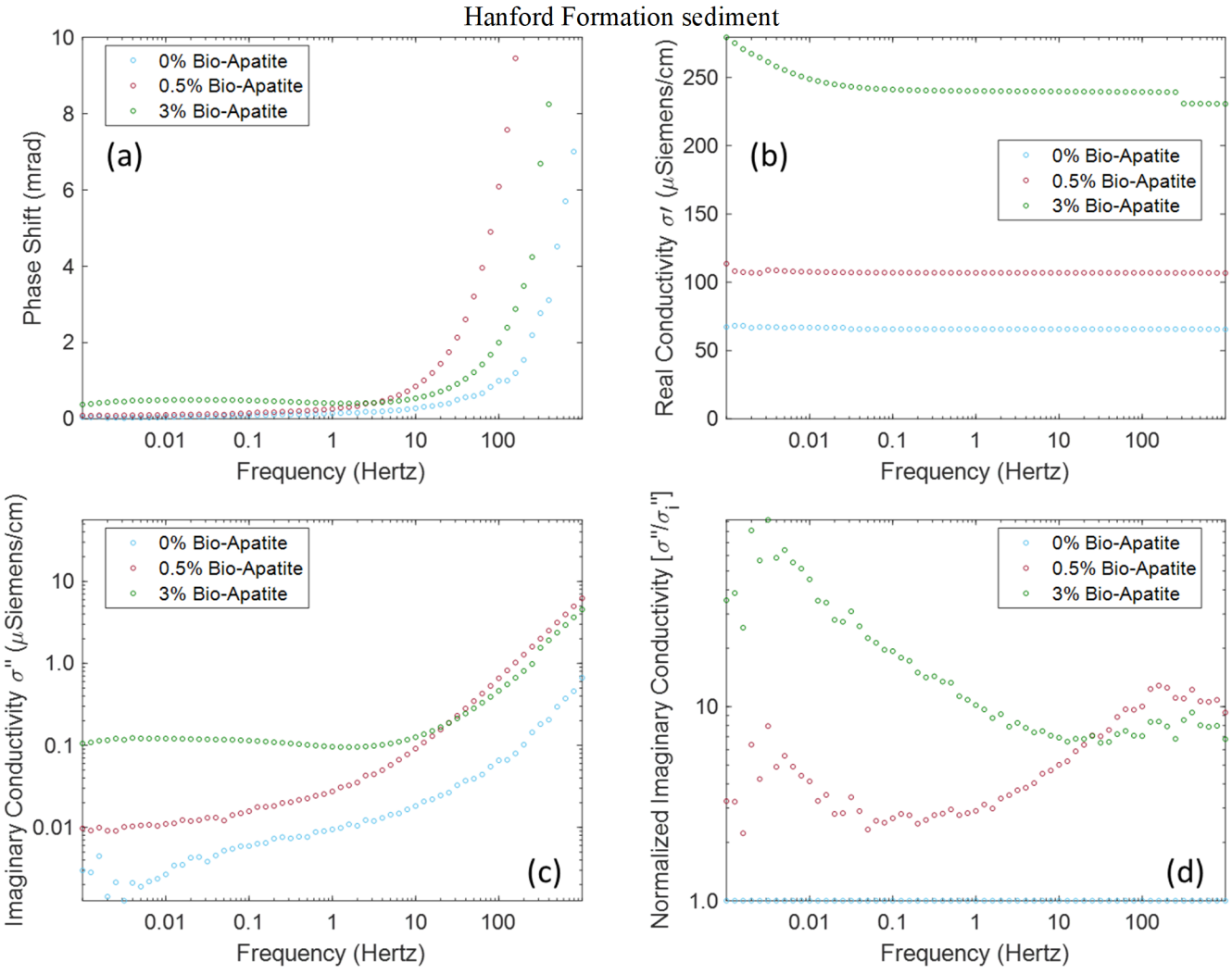

Figure 3.10. Apatite-2 (biotic apatite) at variable wt.% in sand saturated with AGW with (a) phase shift in mrad, (b) real conductivity, (c) imaginary conductivity in µS/cm, and (d) normalized imaginary conductivity with respect to sediment without amendment where *circles* represent the average response for each frequency.

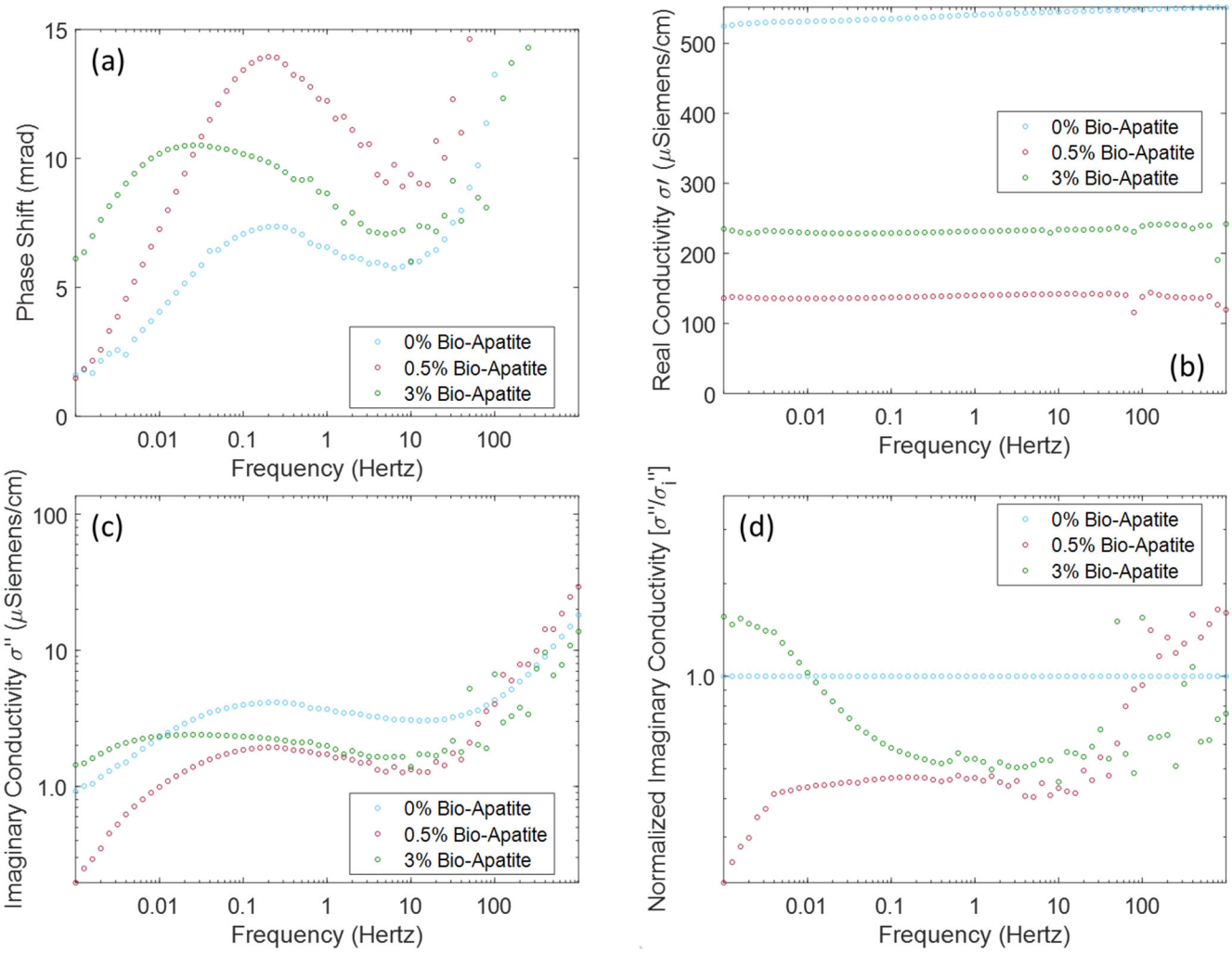

Figure 3.11. Apatite-2 (biotic apatite) at variable wt.% in Hanford formation sediments saturated with AGW with (a) phase shift in mrad, (b) real conductivity, (c) imaginary conductivity in µS/cm, and (d) normalized imaginary conductivity with respect to sediment without amendment where *circles* represent the average response for each frequency.

3.2.1.5 Biotic Apatite *In-Situ* Formation in Laboratory-scale Columns

Bio-precipitated apatite (apatite-2) was formed *in situ* in columns via injection of a Ca-citrate/Na-phosphate solution using unfiltered Columbia River water and Hanford formation sediment so natural soil and river water microbes could biodegrade the citrate (as described in Appendix A, Section A.1.4, with column depiction in Figure 3.9). This results in relatively high surface area apatite (94 m^2/g), which previous studies have shown is a result of 100-nm-sized rods of apatite conglomerated on surfaces (Szecsody et al. 2009). Previous studies have also shown that there is very little inorganic carbon co-precipitated in the apatite (0.02%). However, in the presence of very high microbial biomass concentrations (10^9 cells/mL), the organic carbon fraction in the apatite was up to 0.78%. Although this is small, there is potential to observe signatures from bacteria in the SIP response in the low frequency range (0.1 – 100 Hz) as illustrated by previous work (e.g., Revil et al. 2012).

Approximately five pore volumes of apatite-forming solutions (as described in Appendix A, Section A.1.4) were injected into a 24-in. length by 0.5-in. ID column and allowed to precipitate in the absence of flow over 2 weeks. After this period, the column was flushed with several pore volumes of AGW. The sediments reached relatively consistent loadings of phosphate (max of 0.1 wt.%), biomass (up to 10^7 CFU/g), and organic carbon (up to 0.09 wt.%) across the column (Table 3.2). The biomass and organic carbon content indicate microbial growth occurred over the time of the experiment.

Over time, there were significant changes in the SIP response, including a slow decrease in imaginary conductivity (or surface conductivity) and phase shift, which reached a maximum after 3 days with a peak of approximately 11 µS/cm at 0.001 Hz and 7 µS/cm at 1 Hz, although significant increases were also observed at higher frequencies similar to other amendments (Figure 3.12). The response is decreasing at 7 and 10 days and decreases more after flushing with AGW at 14 days. These results are similar to those observed in data for smaller columns with apatite-2 mixed with Hanford formation sediments (e.g., Figure 3.5), which suggests that apatite formation may decrease conductivity of sediment surfaces when formed *in situ*. Previous studies have shown that the Ca and phosphate initially precipitate as an amorphous phase, then progress to mono-calcium phosphate, di-calcium phosphate, and finally hydroxyapatite over the course of weeks to months (Moore et al. 2007; Sumner 2000). These results highlight that the SIP response changes with respect to both phase shifts and imaginary conductivity over time as the apatite precipitates, although additional work may be necessary to identify frequency-specific signals associated with the precipitation and crystallization of hydroxyapatite over time.

It should be noted that the presence of microbial activity may also have impacted the SIP response, as Zhang et al. (2014) previously reported a linear relationship between microbe density in sand and imaginary conductivity at low frequency (0.05-0.1 Hz). However, it is unclear how the bacteria may be impacting the EDL in heterogeneous sediments while apatite is precipitating. A low-frequency response was also observed for apatite in previous experiments in the absence of bacteria. After initial injection of apatite-forming solutions, the real conductivity increases significantly, consistent with the high ionic strength of the solutions. However, it does not return to the AGW baseline during flushing, suggesting that remaining apatite continues to undergo slow dissolution.

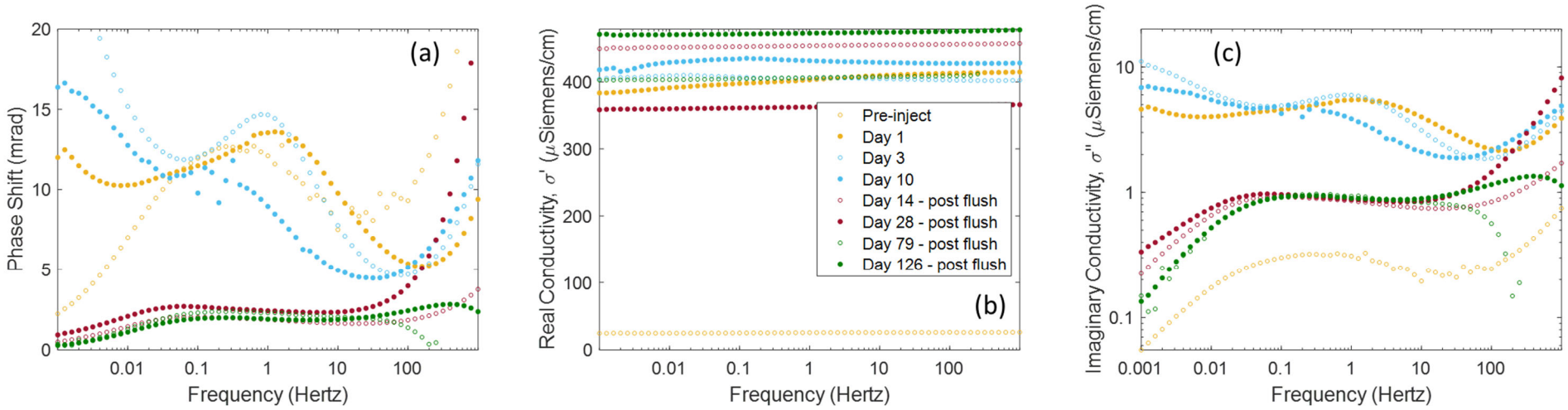

Figure 3.12. Apatite-2 (biotic apatite) formed *in situ* over time in 24-in. length by 0.5-in. ID column packed with Hanford formation sediments and saturated with AGW and apatite-forming solutions with monitoring over time as (a) phase shift in mrad, (b), real conductivity, and (c) imaginary conductivity in µS/cm with respect to initial sediment without amendment (*open, yellow circle*), where *circles* represent the average response at each frequency for three loops of data collected.

Table 3.2. Summary of destructive characterization of apatite-2 column after 130 days of reaction (with the first 14 days in the absence of flow with apatite forming solutions).

	Phosphorus (µg/g)		Phosphate (wt.%)	Biomass	Organic Carbon	Moisture Content
Sample ID	Extract 5	Extract 6	Extract 6	(CFU/g)	(dry wt.%)	(dry wt.%)
Inlet	824	1001	0.10	1000	0.073	19.5
SIP 1	807	866	0.05	10000	0.094	22.5
Space 1	755	920	0.07	1000000	0.071	20.9
SIP 2	537	856	0.05	1000000	0.080	19.8
Space 2	536	825	0.04	10000	0.087	18.9
SIP 3	518	816	0.05	10000	0.088	14.2

3.2.1.6 Apatite Summary and Comparison

For all experiments, the observed phase shifts and imaginary conductivity values were relatively low due to the low polarizability and conductivity of apatite minerals as summarized in Table 3.1. When an apatite standard material (apatite-1) was mixed with sand or Hanford sediments, little change was observed for 0.1 and 1.0 wt.% additions, with a decrease in phase shift and imaginary conductivity in some cases when compared to sand or sediment without apatite. However, the 10 wt.% apatite always increased in phase shift and imaginary conductivity in the low frequency range (< 10 Hz). In Hanford sediments, the peak for the imaginary conductivity also shifted for the highest apatite loading when mixed, suggesting some change the time constant or chargeability of the surfaces, likely due to changes in particle or pore size (Chuprinkov and Titov 2017; Bücker et al. 2018, 2019; Binley and Slater 2020). The real conductivity was strongly dependent on the addition of APW or AGW in mixed columns with little change with apatite, further confirming the low surface conductivity of apatite. Biotic apatite additions (apatite-2, respectively) to the sand resulted in relatively similar phase shift and imaginary conductivity changes in the 0.001 to 10 Hz frequency range than observed for abiotic apatite, although an increased response was observed > 10 Hz.

When apatite was precipitated *in situ*, the changes in phase shift and imaginary conductivity were more visible for a lower wt.% of apatite, as shown by loadings of apatite precipitated from polyphosphate of approximately 0.2 wt.% (Table 3.1) with a decrease in response compared to the control, which was consistent with that observed for apatite mixed in the columns. This is likely due to decreased variability in background sediments during the experiments in the absence of mixing and the potential for apatite to coat sediment surfaces as opposed to mixing with them. Moreover, the overall decrease in response is consistent with the low surface conductivity and polarizability of apatite minerals. However, for biotically precipitated apatite, there are two peaks observed in the phase shift and imaginary conductivity below 10 Hz in the first 10 days of the experiment, which may be due to bacterial growth on surfaces. There is a different mechanism impacting surface polarization and conductivity as the response decreases more slowly than for *in situ* formation of apatite from polyphosphate.

These results indicate promise in using SIP to monitor changes in both the solution phase (real conductivity) and surface polarization (imaginary conductivity) due to delivery of apatite-forming solutions and subsequent mineralization. Additional testing was conducted where apatite was precipitated from polyphosphate in the presence of variable concentrations of SMI and Hanford sediments to consider the potential for two-step remediation with initial delivery of a reductant (SMI) followed by formation of a mineral phase that helps to sequester the reduced contaminants (apatite or calcite) as described in Section 3.4.

Table 3.3. Summary of maximum SIP response for apatite introduced via various methods (mixing of inorganically produced apatite, apatite-1, or biotically produced apatite, apatite-2, or *in situ* precipitation) in columns saturated with AGW.

Experiment	Phase Shift (mrad)	Imaginary Conductivity (µS/cm)	Frequency Range (Hz)
Mixed – Sand – 10 wt.% apatite-1	10	0.6	< 10
Mixed – Hanford sediment – 10 wt.% apatite-1	10	1.5	< 10
In-situ – Hanford sediment – poly[(a)]	10	0.6	< 10
Mixed – Sand – 3 wt.% apatite-2	<1.1; 10	0.1; 8	< 10; > 100
Mixed – Hanford sediment – 3 wt.% apatite-2	14; 18	5;12	< 10; > 100
In-situ – Hanford sediment – apatite-2	20	11	< 10

(a) Poly – Apatite produced from slow precipitation of polyphosphate.

3.2.2 Calcite Amendments

Calcite was precipitated and then added to sand and Hanford formation sediments with different masses. Table 3.4 summarizes the major observations for calcite mixed with sand or Hanford formation sediments. In comparison to apatite additions, calcite addition to sand resulted in a smaller phase shift (< 1 mrad for 10 wt.%) in the mid frequency range (0.01 to 10 Hz, Figure 3.13a) as contrasted to abiotic apatite (< 10 mrad for 10 wt.%) and biotic apatite (< 1.1 mrad for 3 wt.%). The corresponding imaginary conductivity was nearly indistinguishable from the baseline when considering the 95% CIs (*not shown*). For calcite added to Hanford formation sediments (Figure 3.14), the maximum phase shift observed was slightly higher (13 mrad for 1.0 wt.% and 10.5 mrad for 10 wt.%), although likely not significant when accounting for the 95% CIs and the lack of correlation with concentration. Moreover, similar to observations for apatite-2 (biotic apatite) in Hanford formation sediments, a decrease in imaginary conductivity was observed as compared to the baseline sediments without amendments at frequencies > 0.01 Hz. This result highlights that in some cases the amendments may decrease the sediment surface conductivity by coating natural mineral phases (e.g., Fe oxides or clays), although it is within the 95% CIs when mixed with Hanford sediments.

Additional testing of *in situ* calcite precipitation in the presence of sediment, ZVI, and SMI for dual amendment testing is presented in Section 3.4. The *in situ* precipitation and coating of sediments with targeted low-conductivity mineral phases (e.g., calcite and apatite) resulted in different signals as compared to mineral phases mixed with sediments as observed for apatite (Section 3.2.1.3). There is also promise in monitoring calcite precipitation following delivery of a relatively high- conductivity reductant (e.g., ZVI and SMI) based on a reduction in phase shift and imaginary conductivity from relatively low-conductivity calcite coating ZVI and SMI surfaces. This phenomenon has been previously demonstrated, where surface polarization was attributed to both well distributed, discrete precipitates and localized precipitate aggregation and pore clogging in the presence of glass beads (Wu et al. 2009, 2010). Moreover, although the SIP response to calcite is relatively small, it has also been successfully used to monitor microbial induced carbonate precipitation for soil stabilization at the field scale (Saneiyan et al. 2019).

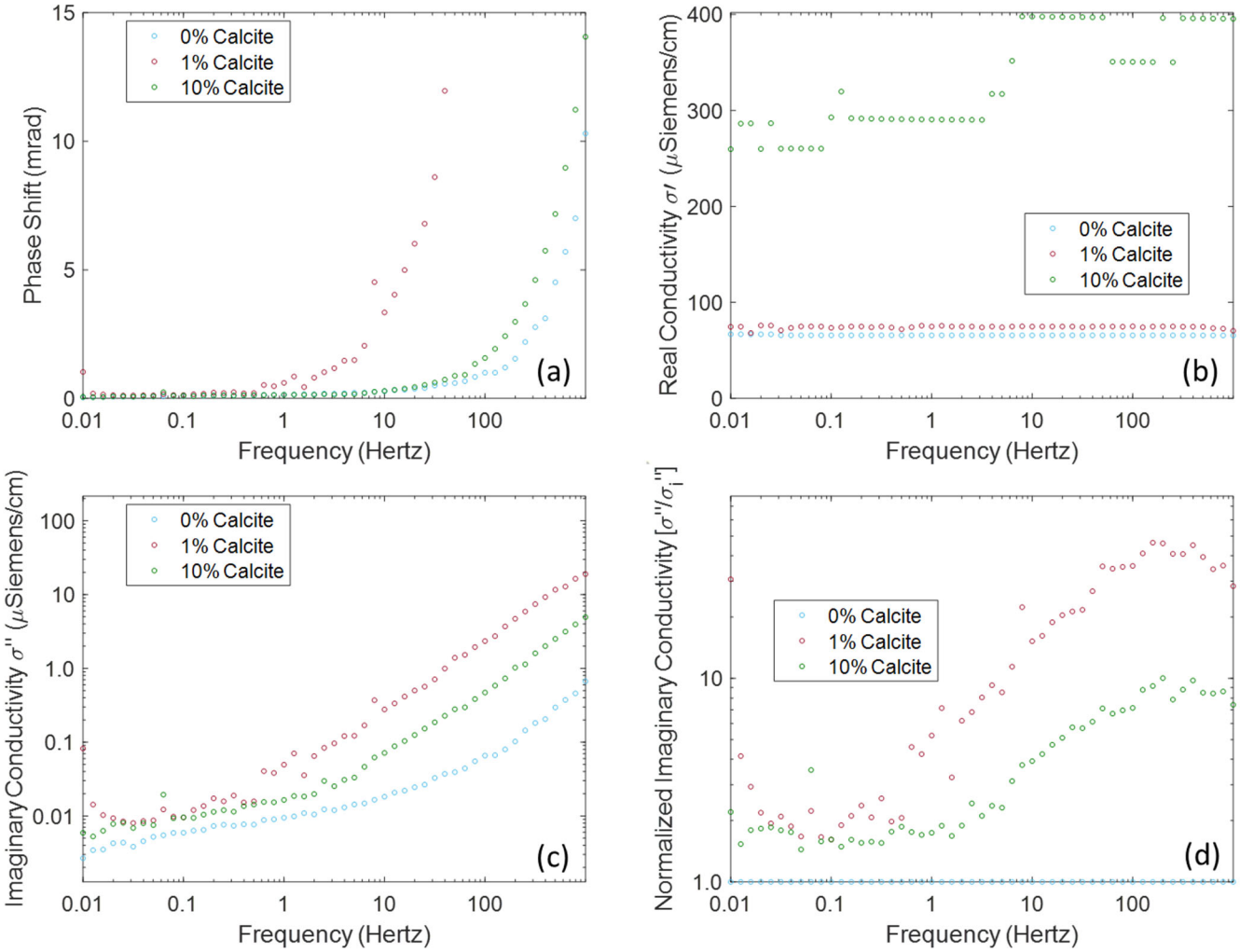

Figure 3.13. Calcite at variable wt.% in sand saturated with AGW with (a) phase shift in mrad, (b) real conductivity, (c) imaginary conductivity in µS/cm, and (d) normalized imaginary conductivity with respect to sediment without amendment, where *circles* represent the average response for each frequency.

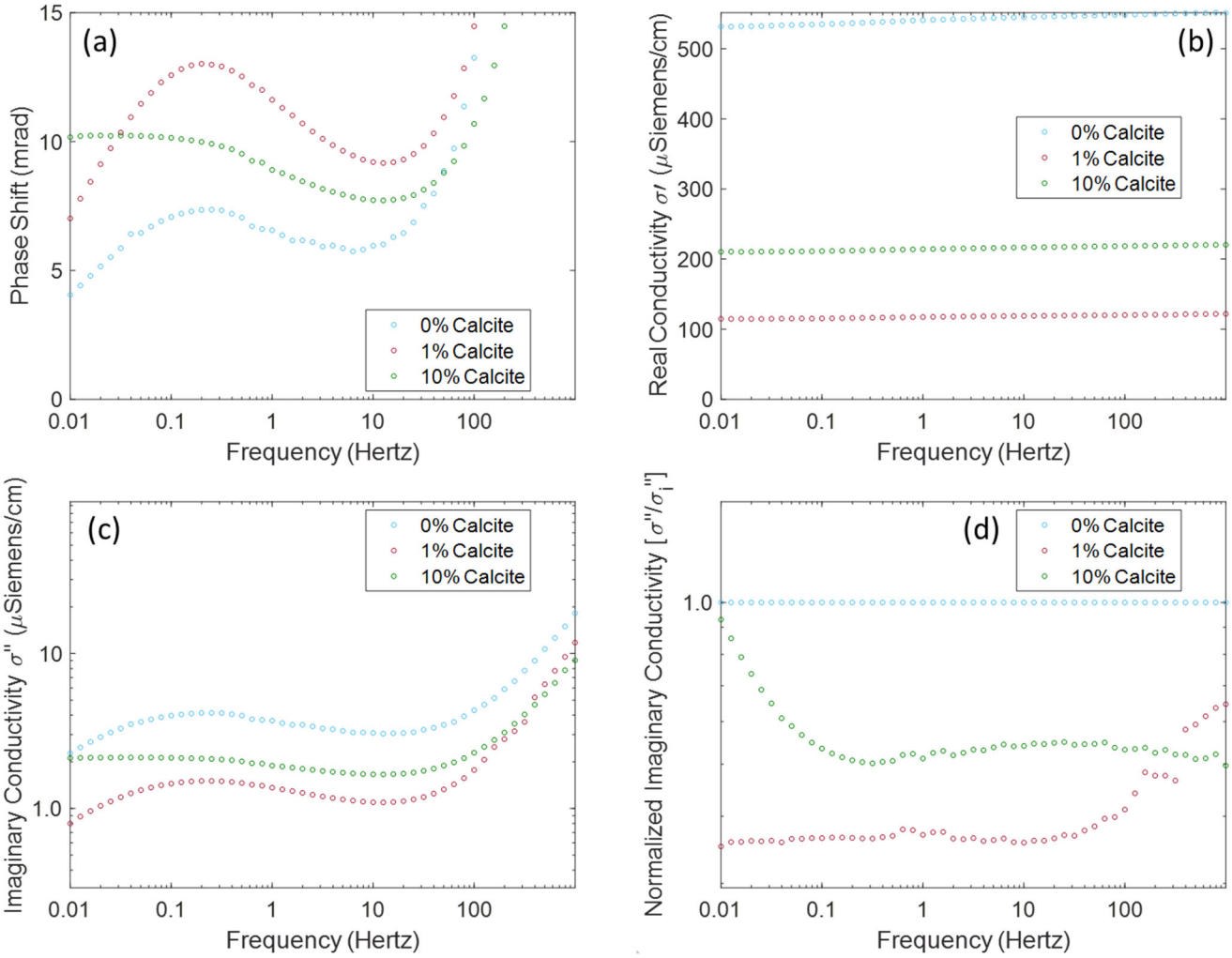

Figure 3.14. Calcite at variable wt.% in Hanford formation sediments saturated with AGW with (a) phase shift in mrad, (b) imaginary conductivity in µS/cm, and (c) normalized imaginary conductivity with respect to sediment without amendment, where *circles* represent the average response for each frequency.

Table 3.4. Summary of SIP response upon calcite addition.

Matrix	Calcite (wt.%)	Phase Shift (mrad)	Imaginary Conductivity (µS/cm)	Frequency Range (Hz)
Sand	10 (mixed)	2	0.3	< 0.1
Hanford sediment	10 (mixed)	10.5	3.0	< 0.1

3.2.3 Bismuth Amendments

Significant phase shifts or changes in imaginary conductivity were not observed for bismuth added to sand and Hanford formation sediments up to 10 wt.%. Although the phase shifts look significant for sand (Figure 3.15a), they are within the 95% CIs (*not shown*, ± 52% below 1 Hz and 86% above 100 Hz for triplicate columns). Although there appears to be a small decrease in phase shifts and imaginary conductivity for bismuth mixed with Hanford formation sediments, they may not be significantly

different due to the variability in SIP signals of Hanford sediments only (Figure 3.1 and Figure 3.16; 95% CIs for bismuth are approximately ± 7% below 1 Hz and 27% above 100 Hz). In addition, significant changes in imaginary conductivity were not observed (Figure 3.15b,c,d and Figure 3.16b,c). These results indicate that the bismuth sub-nitrate material does not have a significant surface conductivity or capacitance. Moreover, it likely did not coat sediments within the timescale of experiments as it was added as a solid material, which can impact the SIP response from sediments. However, it is also possible that the small bismuth particles were partially flushed from the columns during saturation. Other bismuth materials may have a detectable signal due to physical changes upon addition (e.g., particle size or surface area) or the presence of high-conductivity impurities.

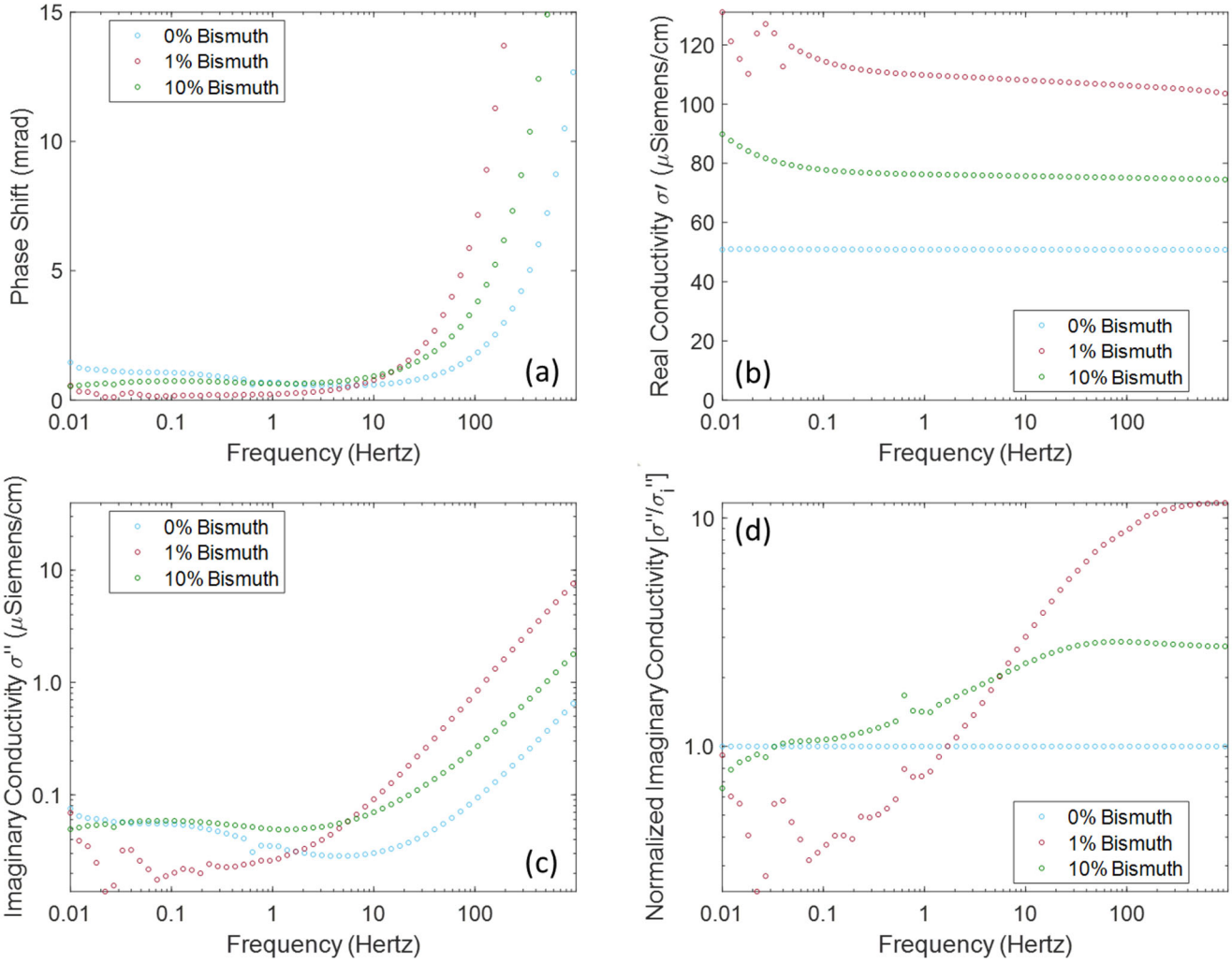

Figure 3.15. Bismuth at variable wt.% in sand saturated with AGW with (a) phase shift in mrad, (b) real conductivity, (c) imaginary conductivity, and (d) normalized imaginary conductivity with respect to sediment without amendment, where *circles* represent the average response for each frequency.

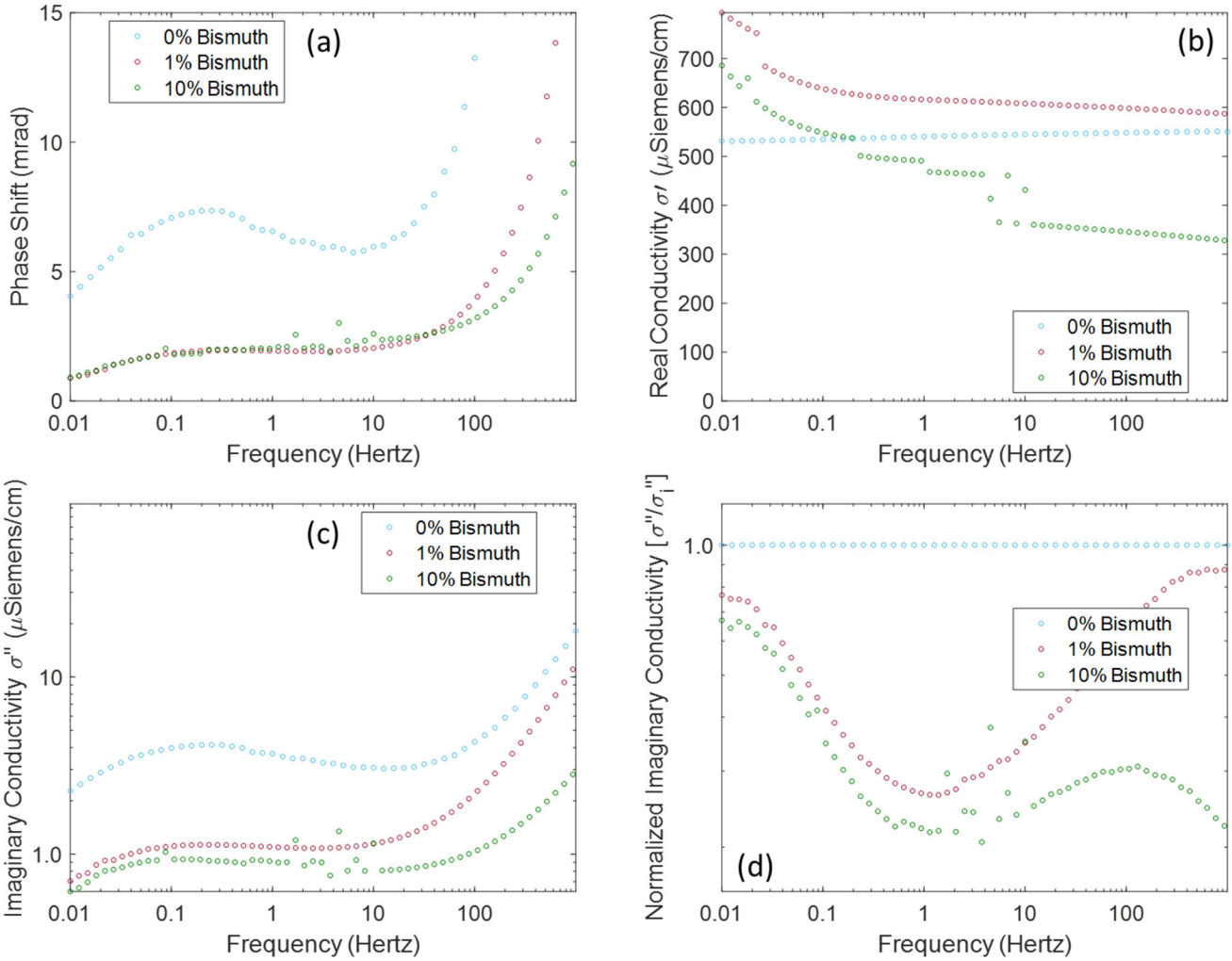

Figure 3.16. Bismuth at variable wt.% in Hanford formation sediments saturated with AGW with (a) phase shift in mrad, (b) real conductivity, (c) imaginary conductivity, and (d) normalized imaginary conductivity, where *circles* represent the average response for each frequency.

3.3 Iron and Sulfur Amendments

3.3.1 Zero Valent Iron Amendments

3.3.1.1 Zero Valent Iron Detection in Sand

The addition of increasing concentrations of ZVI to silica sand resulted in a decrease in phase shifts across the frequency range (Figure 3.17a). Moreover, these phase shifts resulted in a significant increase in imaginary conductivity of about two to three orders of magnitude greater than the untreated silica (Figure 3.17b and c). These phase and imaginary conductivity changes in the AGW (Figure 3.17) were consistent with that observed in the APW (Figure 3.18). Significant phase shifts were observed above 10 Hz, which is consistent with previous research (Abdel Aal et al. 2014; Mellage et al. 2018; Szecsody et al. 2020a). In addition, increases in phase shift and imaginary conductivity were observed in the low frequency range (< 10 Hz) for the highest ZVI concentration (10 wt.%). These changes in SIP response have previously been suggested to be due to adsorption of Fe^{2+} (Orozco et al. 2011; Szecsody et al.

2020a) or changes in particle or pore sizes (Chuprinkov and Titov 2017; Bücker et al. 2018, 2019) and their subsequent impacts to the EDL. For example, Chang and Sposito (1994) modeled the EDL in different clay particle sizes with negatively charged basal planes and a positively charged surface. Their results showed that the anion exclusion zone is determined by the individual particle's radius. However, experiments measuring ZVI particles of variable particle size and surface area did not exhibit clear trends as shown in Figure 3.19 based on the ZVI materials listed in Table 2.1. It is possible that there were other factors impacting the SIP signal, including varying levels of iron oxidation products or impurities. Importantly, similar ZVI amendments were also detected at field-scale remediation concentrations in relatively non-conductive sediments as shown in previous work (Orozco et al. 2015).

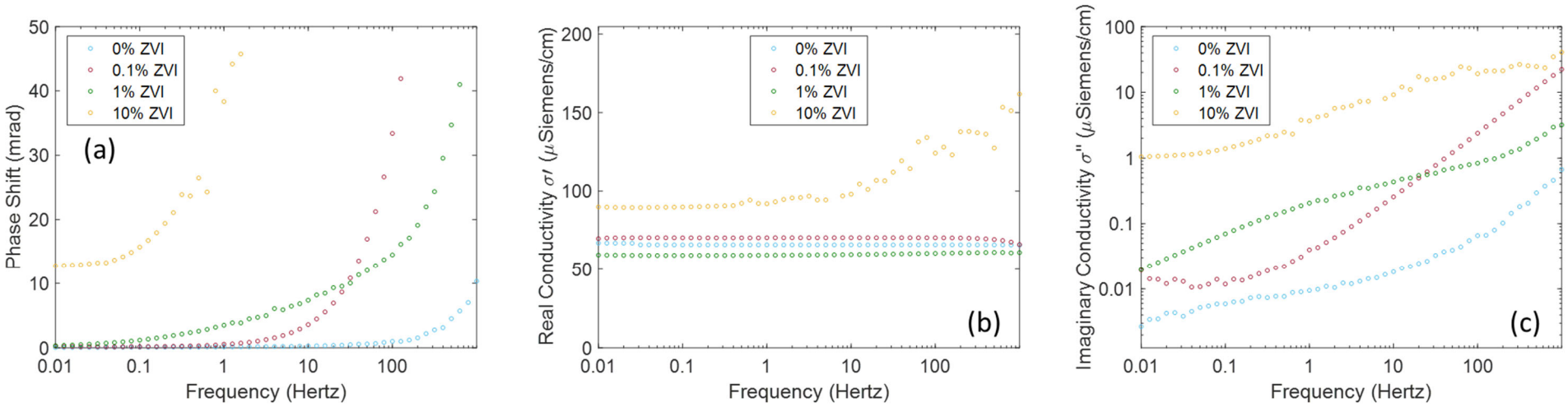

Figure 3.17. ZVI-1 (< 44 µm) at variable wt.% in sand saturated with AGW with (a) phase shift in mrad, (b) real conductivity, and (c) imaginary conductivity in µS/cm, where *circles* represent the average response for each frequency.

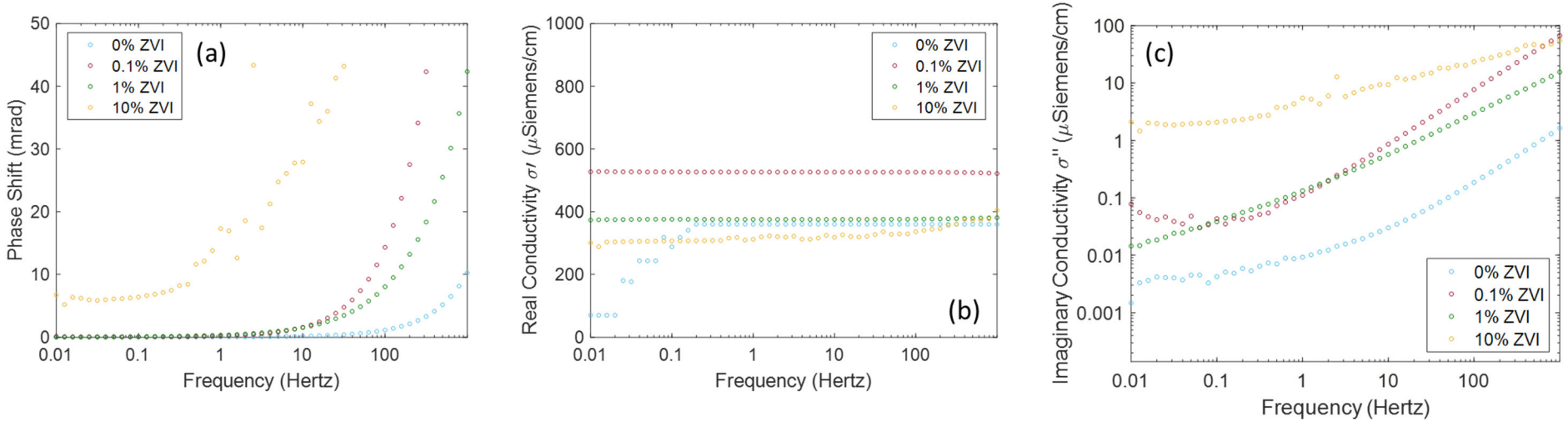

Figure 3.18. ZVI-1 (< 44 µm) at variable wt.% in sand saturated with APW with (a) phase shift in mrad, (b) real conductivity, and (c) imaginary conductivity in µS/cm, where *circles* represent the average response for each frequency.

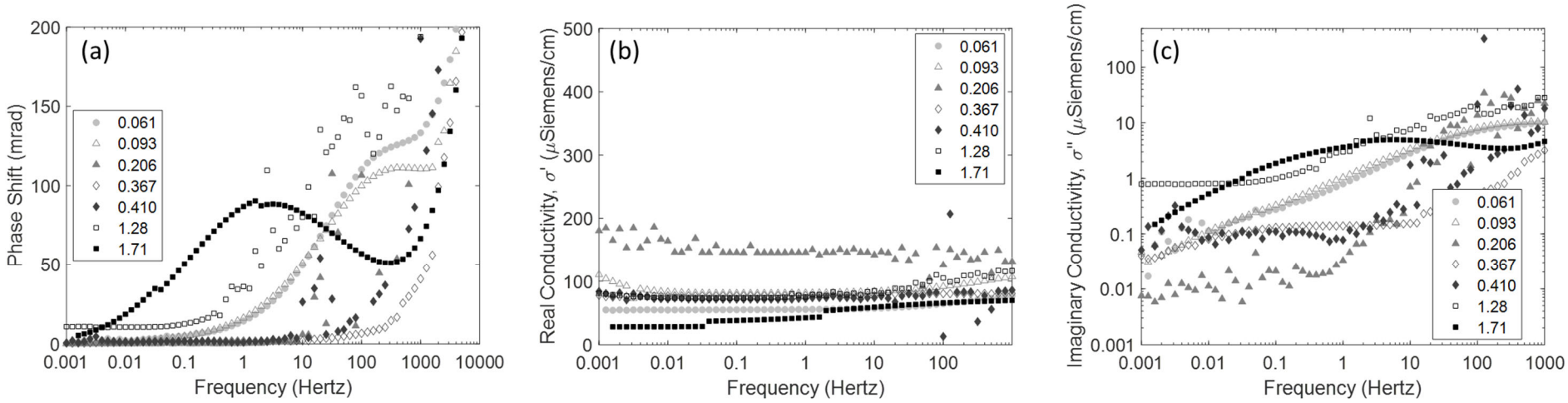

Figure 3.19. Variable ZVI based on surface area (m^2/g, *increasing* from gray to black with series) packed at 10 wt.% in sand saturated with AGW with (a) phase shift in mrad, (b) real conductivity, and (c) imaginary conductivity in µS/cm, where *circles* represent the average response for each frequency.

3.3.1.2 Xanthan Gum Detection in Sediments

To effectively deliver particulate amendments in the subsurface, sheer thinning fluids are used to increase the mobility of reactive particles. Previous research identified xanthan gum as the optimal additive for delivery of ZVI (Truex et al. 2011; Zhong et al. 2013). Figure 3.20 shows that there is not a significant impact of xanthan gum on the SIP response (phase shift or imaginary conductivity) of Ringold Formation sediments. Therefore, additional testing was not conducted with other sediments (e.g., Hanford formation or sand). It is possible that xanthan gum could coat ZVI and decrease its response as observed previously for other carrier solutions (e.g., P104 surfactant) (Mellage et al. 2018); however, the lack of observed changes in sediments in this work suggests this is unlikely. Notably, previous research suggests that there may be some slow, long-term degradation of polymers like xanthan gum, which may impact SIP response and the ability for multiple amendment injections at a site (Muller et al. 2021a,b).

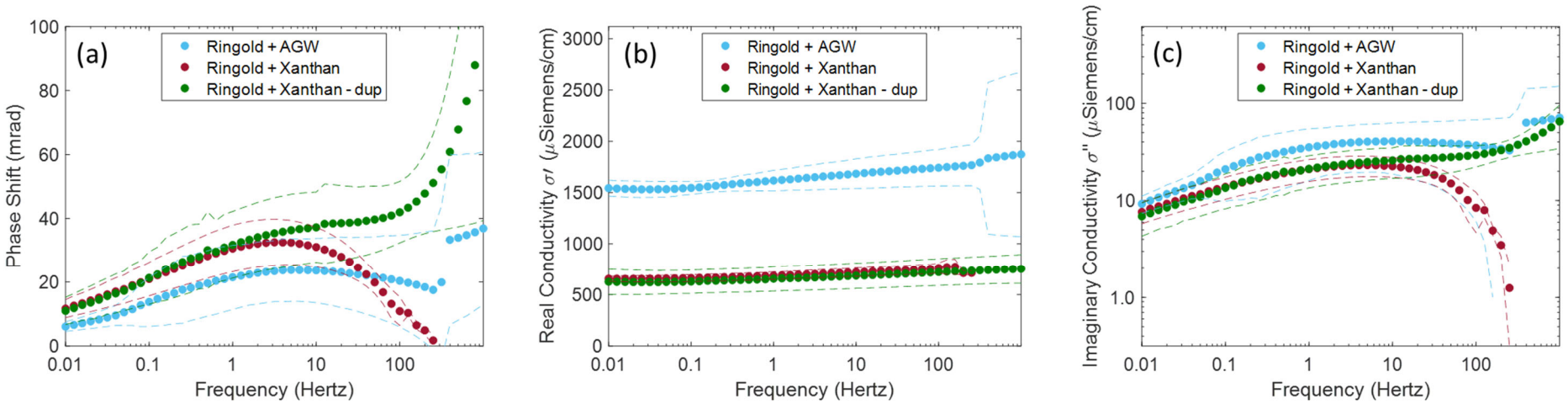

Figure 3.20. Ringold Formation sediments were saturated with xanthan gum (800 mg/L) in AGW with added nitrate with (a) phase shift in mrad, (b) real conductivity, and (c) imaginary conductivity in µS/cm, where *circles* represent the average response for each frequency and *dashed lines* represent 95% confidence intervals based on collection of triplicate loops across the frequency for each column.

3.3.1.3 *In Situ* Injection of Zero Valent Iron with Xanthan Gum into Sand

A micron-sized ZVI (ZVI-2) was injected into duplicate 2.5 cm (1 in.) diameter columns packed with sand with and without 800 mg/L xanthan gum dissolved in AGW at a 1 mL/min flow rate (Figure 3.22 and Figure 3.22). SIP electrodes were installed as described in Section 2.3. Prior to injection of ZVI-2, a tracer test was conducted on both columns with injection of 1000 mg/L Br^- with similar breakthrough. Then, approximately five pore volumes of ZVI-2 were injected in suspension with AGW and 800 mg/L xanthan gum followed by flushing of the column with AGW. Effluent was collected with monitoring of the mass of ZVI-2 remaining in suspension based on the mass recovered after drying at 105°C (Figure 3.23). The reproducibility between the duplicate columns highlights that the brass mesh (for current electrodes) and side body ports (for potential electrodes) did not impact injection of ZVI-2. Following this experiment, the column with SIP electrodes was allowed to remain static with subsequent monitoring up to 130 days. The column was sectioned into 1-in. sections and homogenized, and significant alteration of ZVI over time was observed but not quantified (Appendix E, Figure E.1).

SIP measurements were also collected repeatedly during ZVI and xanthan gum injection at select points (0.1, 1.0, 10, 100, and 1000 Hz, Figure 3.21), beginning approximately 15 minutes after injection started. Similar to long-term monitoring, these values did not change significantly over time for the potential electrode pair near the influent end cap (pair 1 – near the influent). The imaginary conductivity and phase shift increased over time in the effluent potential electrode pair (pair 3). Based on this result, it is likely that the imaginary conductivity and phase shifts are impacted by removal of xanthan gum coatings on ZVI in the short term.

Data show that the ionic strength in solution remained elevated following ZVI and xanthan gum injection and flushing with AGW based on real conductivity (Figure 3.22b) for the third pair of electrodes. The results for pairs 1 and 2 are in Appendix E in Figure E.2 and Figure E.3. However, after 5 days the ionic strength dropped significantly to reach values similar to AGW as shown by the comparison prior to ZVI injection. Over time, the phase shift increased at lower frequency (Figure 3.22a). An increase in phase shift over time may indicate an increase in surface capacitance, which may be due to polarization of ZVI or secondary iron oxides forming as the ZVI oxidizes. Because significant changes in SIP over time were observed in pair 3 of electrodes (near the effluent side of the column) but not in pairs 1 and 2 (Figure E.2 and Figure E.3), it is suggested that changes are primarily due to formation of iron oxidation products. In addition, though some fluctuations in the imaginary conductivity were observed in the first five days (Figure 3.22c), these are likely not due to xanthan gum. Although previous teams have noted changes due to carrier solutions including guar gum and mineral oil in association with ZVI injections (Orozco et al. 2015; Shi et al. 2015), no significant impact of xanthan gum on SIP was observed in different sediments. Previous work has shown changes in phase shift and imaginary conductivity after ZVI aging and oxidation within columns (Szecsody et al. 2020a). Therefore, it is likely that additional frequency-specific changes will occur over time, especially in the presence of groundwater flow, where oxygen can be more quickly reintroduced to the system.

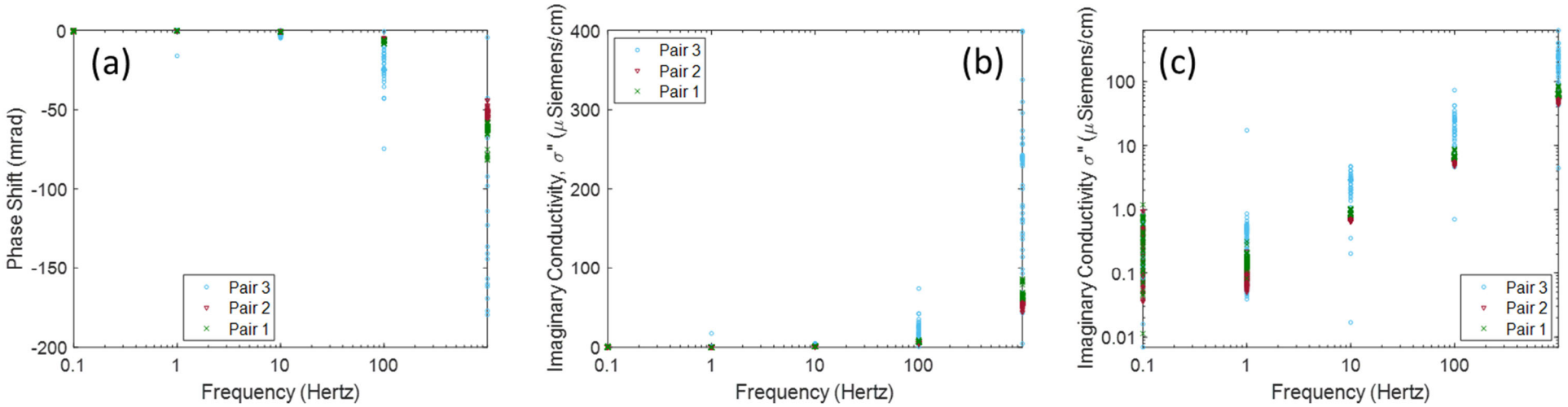

Figure 3.21. SIP response over time during 1.5 wt.% ZVI-2 (1-5 µm) injection with AGW and 800 mg/L xanthan gum at 1 mL/min into sand with five frequencies measured repeatedly across the duration of injection with (a) phase shift in mrad and (b-c) imaginary conductivity in µS/cm on semi-log and log-log scales, respectively. Note: The phase shift and imaginary conductivity increased with time in pair 3 as the data was continuously collected across the five frequencies.

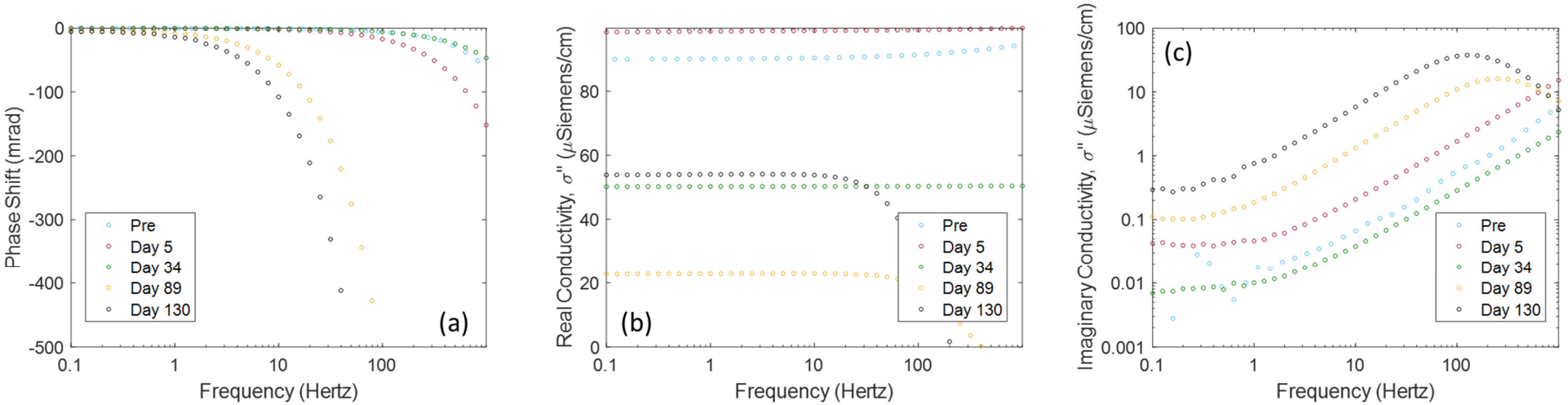

Figure 3.22. Pair 3 SIP response before and after injection of 1.5 wt.% ZVI-2 (1-5 µm) with AGW and 800 mg/L xanthan gum at 1 mL/min into sand with (a) phase shift in mrad, (b) real conductivity in µS/cm, and (c) imaginary conductivity in µS/cm, where pair 1 is the electrode potential pair closest to the influent end cap and pair 3 is the electrode potential pair closest to the effluent end cap, with *points* and circles representing the average of three loops of data collected on one column.

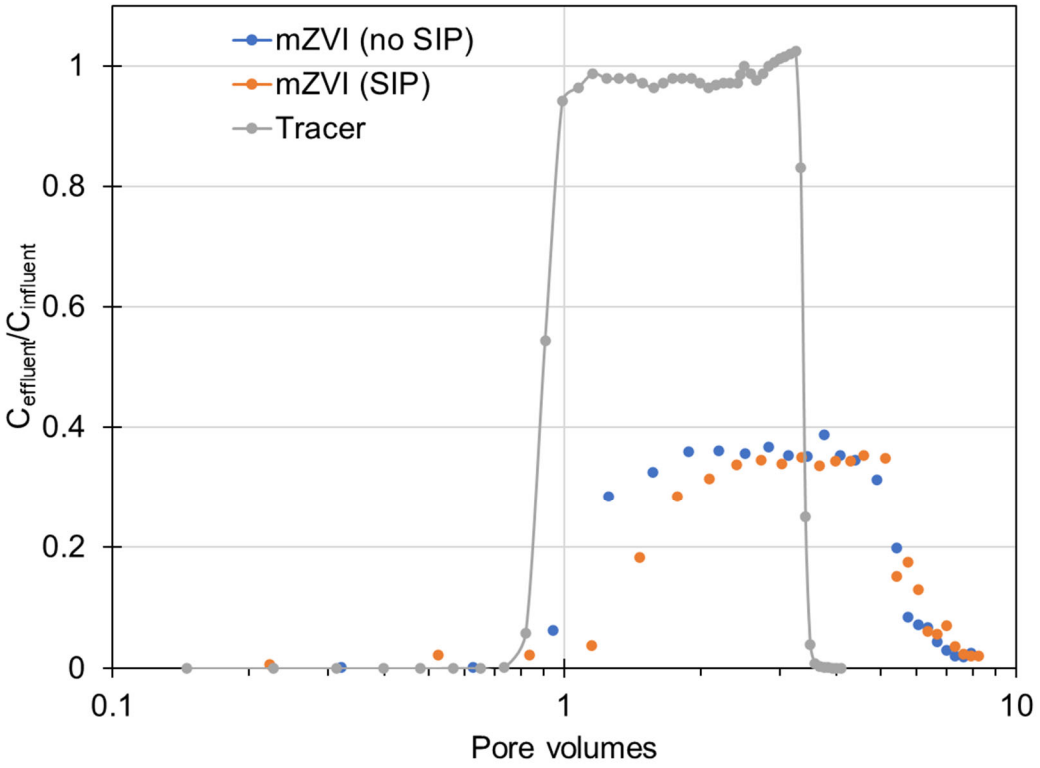

Figure 3.23. Effluent recovery of a 1000 mg/L Br^- tracer injection overlaid with subsequent ZVI injection at 1.5 wt.% (ZVI-2) with AGW and 800 mg/L xanthan gum at 1 mL/min based on mass recovery for duplicate columns, one with and one without SIP electrodes.

3.3.1.4 Zero Valent Iron Detection in Hanford Formation Sediments

In Figure 3.24, there is a significant phase shift observed as compared to Hanford sediments without ZVI for all amendments across the frequency range, although the greatest shift occurs for 10% ZVI above 1 Hz. The imaginary conductivity is significantly increased only for the 10% ZVI above 10 Hz, with all other results falling within the 95% CIs for the baseline (*blue*). However, the imaginary conductivity for Hanford formation sediments with ZVI appears to be slightly decreased (although within CIs) as compared to the baseline in the low frequency range, although the 10 wt.% ZVI increased above the baseline below 10 Hz. The phase shift changes allow for differentiation from the sediment baseline at concentrations sufficient for field-scale remediation (as low as 0.1 wt.% at frequencies > 0.1 Hz), while the imaginary conductivity response is not significantly different due to the variability in the Hanford formation sediment baseline with the exception of 10 wt.% ZVI.

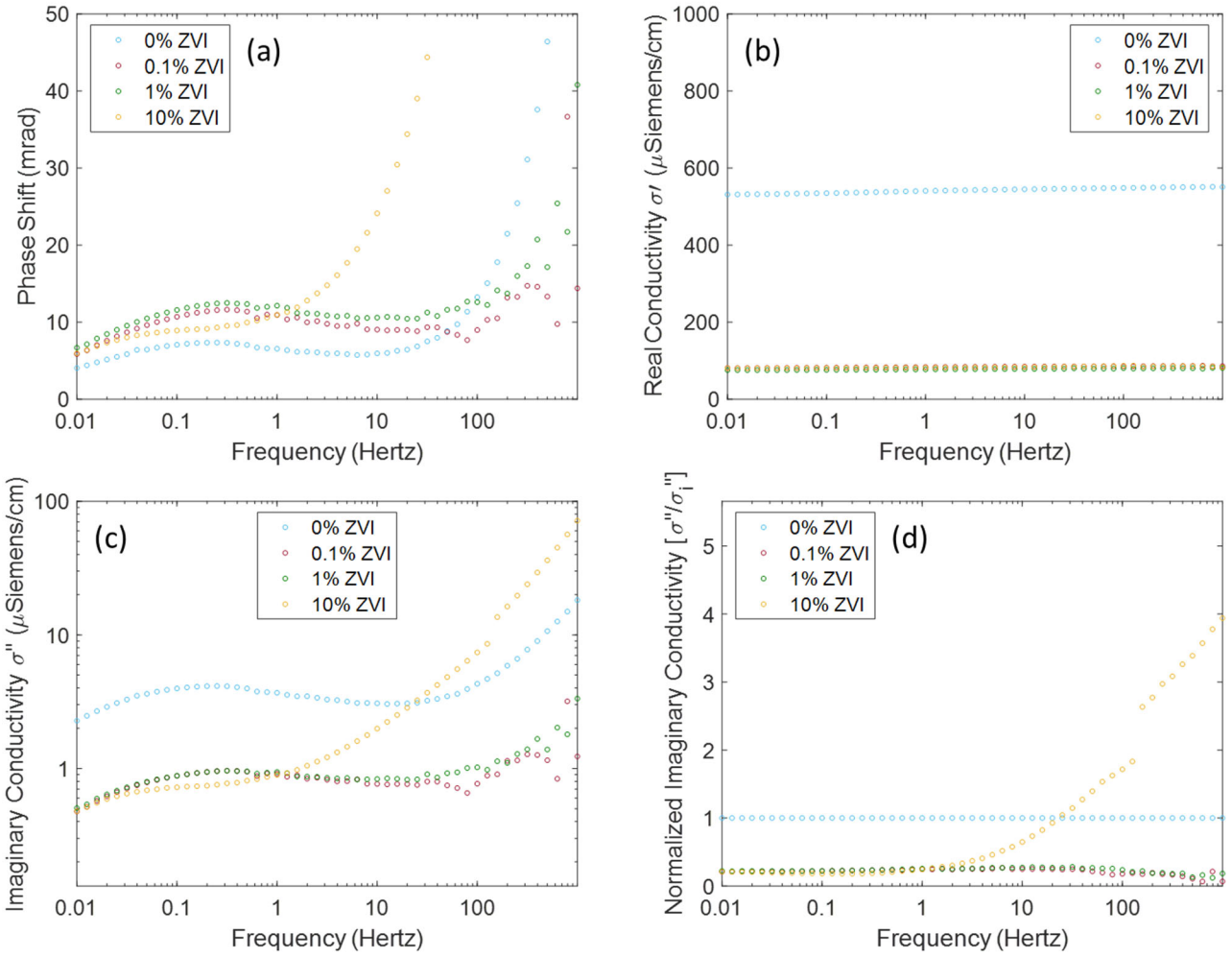

Figure 3.24. ZVI-1 (< 44 µm) at variable wt.% in Hanford formation sediments saturated with AGW with (a) phase shift in mrad, (b) real conductivity, (c) imaginary conductivity in µS/cm, and (d) normalized imaginary conductivity with respect to sediment without amendment, where *circles* represent the average response for each frequency.

3.3.1.5 SIP Response for Zero Valent Iron in Hanford Formation Sediments over Time

SIP measurements were collected up to 43 days in the columns to track changes in signals due to oxidation and secondary precipitation of iron. In Figure 3.25, the day 43 results show two distinct shifts: (1) the phase shift increases with time for both 1 and 10 wt.% ZVI and (2) the imaginary conductivity in the low frequency range decreases more with time for the 10 wt.% ZVI. The phase shifts indicate an increase is surface capacitance over time, potentially due to changes in iron speciation as iron oxidizes and forms secondary phases. These changes are most pronounced > 1 Hz. However, the imaginary conductivity changes are less significant in the higher frequency range and more prounounced in the low frequency for 10 wt.% ZVI. As ZVI ages (oxidizes), ferrous iron is created, which can form adsorbed ferrous iron (on sediment minerals) or ferrous iron phases such as siderite or green rust. Further oxidation of ferrous iron phases results in ferric oxides such as goethite. The imaginary conductivity changes may indicate changes in adsorbed and structural Fe^{2+}, as previous work has indicated that SIP signals for Fe^{2+} adsorption and structural changes occur across lower frequencies (< 10 Hz) as compared with direct identification of iron materials at higher frequency (Orozco et al. 2011; Williams et al. 2009; Szecsody et

al. 2020a). Therefore, low-frequency imaginary conductivity increases may also be caused by the formation of these other phases.

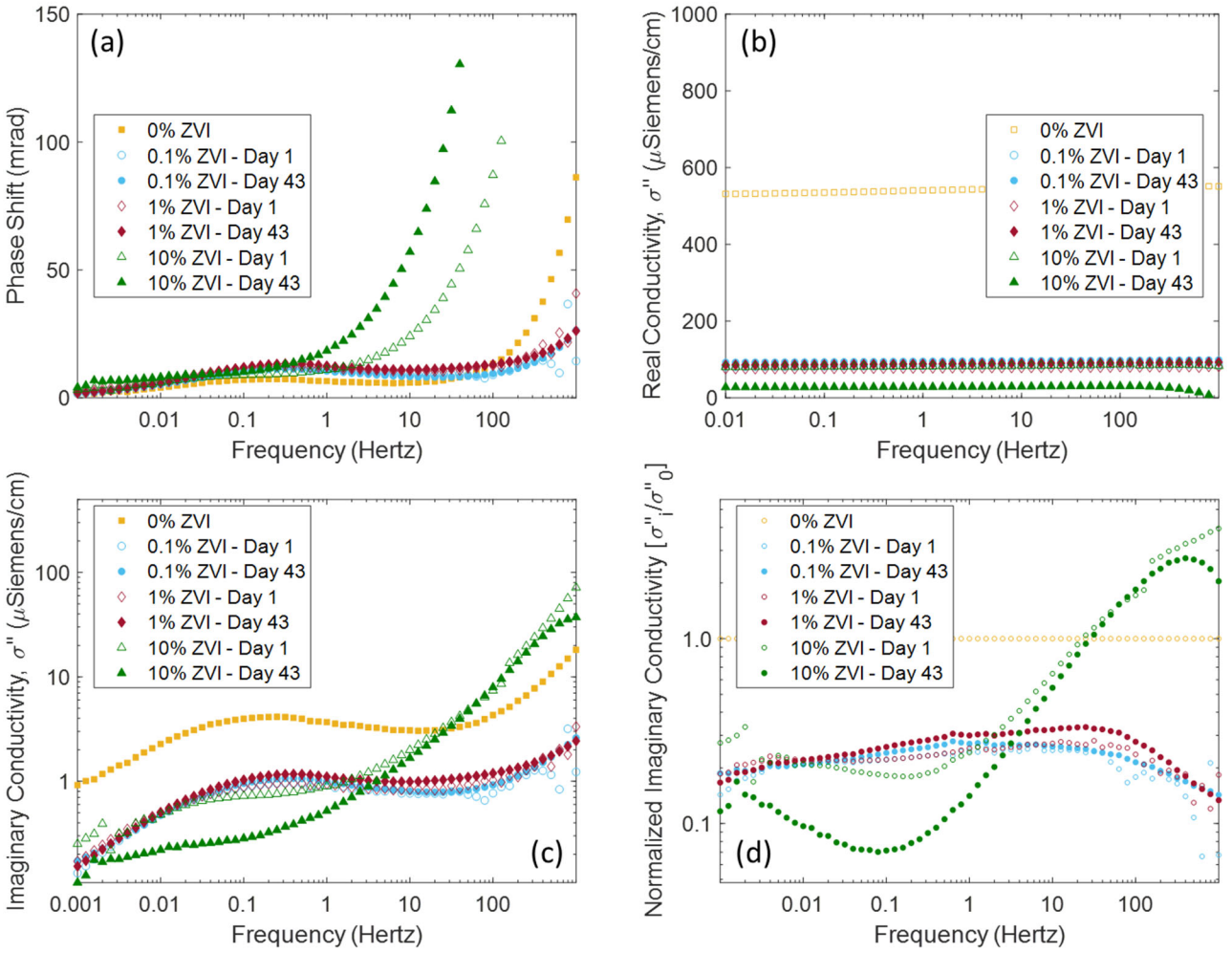

Figure 3.25. ZVI-1 (< 44 µm) before and after aging for 43 days, packed at variable wt.% in Hanford formation sediments saturated with AGW with (a) phase shift in mrad, (b) real conductivity, (c) imaginary conductivity in µS/cm, and (d) normalized imaginary conductivity with respect to sediment without amendment, where *circles* represent the average response for each frequency.

3.3.1.6 Summary of SIP Response for Zero Valent Iron

The results for sand (Figure 3.17 and Figure 3.18) are significantly different with respect to the ZVI amendments (Table 3.5). In these results, there is a significant increase in the phase shift above 10 Hz for 0.1 wt.% and 1.0 wt.% ZVI and across the range of frequency for 10 wt.% ZVI with similar trends for imaginary conductivity. These results are significant as compared to the relatively non-conductive silica sand highlighting that the Hanford formation sediment with ZVI does not behave the same as the sand with ZVI. The impact of ZVI on the SIP response is greater in the sand as compared to the heterogeneous Hanford formation sediments. This is hypothesized to result from (1) lower initial SIP response from sand as compared to Hanford formation sediments and (2) the presence of more fine mineral phases (e.g., clays, trace magnetite) in Hanford formation sediments that may quickly coat the surfaces of ZVI and reduce surface conduction.

Moreover, there are changes in phase shift and imaginary conductivity observed in the low frequency range, which are likely due to adsorption, secondary mineral formation, and/or changes in particle size and porosity. It is likely that different secondary interactions will continue to occur in each background material over time (e.g., Fe^{2+} adsorption or precipitation). For example, the sand may have fewer adsorption sites available for Fe^{2+}, leading to greater precipitation or coating of surfaces causing a difference in SIP signal over time in the sand as compared to the Hanford formation sediments, where adsorption may be more significant. These results indicate that, in the presence of sand, the ZVI can be observed through SIP measurements at significantly lower concentrations than in the Hanford formation sediments. These results indicate the the ZVI can be observed in sediments with relatively low surface conductivity and capacity (i.e., sand) down to 0.1 wt.%; however, ZVI was only observable based on phase shifts in Hanford formation sediments as the variability in the imaginary conductivity was too large to differentiate from the baseline.

Table 3.5. Summary of SIP response upon ZVI addition.

Matrix	ZVI (wt.%)	Phase Shift (mrad)[(a)]	Imaginary Conductivity (µS/cm)[(a)]	Frequency Range (Hz)
Sand	10 ZVI-1 (<44 mm)	150	19.3	0.001 – 1000[(b)]
Hanford fm	10 ZVI-1 (<44 mm)	87	7.4	0.001 – 1000[(b)]

(a) Phase shift and imaginary conductivity reported at 100 Hz.
(b) Significant increases in phase shift and imaginary conductivity above 10 Hz and broad increases above baseline for 10 wt.% ZVI across the entire frequency range.

3.3.2 Sulfur Modified Iron Amendments

Chemically, SMI was characterized by XRD as primarily ZVI (60%) and iron oxides (33% magnetite and 7% FeO). Previous characterization also confirmed the XRD results via Mossbauer (Lawter et al. 2018). Trace sulfur was observed by XRD but not quantified. Because of the large ZVI content, the SMI should behave similarly to ZVI, although iron sulfides have been shown previously to have a strong SIP response in the low frequency range (Williams et al. 2009, Orozco et al. 2011; Placencia-Gómez et al. 2013, 2015; Placencia-Gómez and Slater 2016). The surface area of the SMI was 1.54 m^2/g, or about double that of ZVI-1 (0.852 m^2/g, Table 2.1).

3.3.2.1 SIP Response for Sulfur Modified Iron Addition to Sand and Hanford Formation Sediments

SMI additions to sand showed large (10 to 100 mrad, Figure 3.26a) phase shifts and imaginary conductivity changes (100 times higher than sand with no SMI, Figure 3.26b). With 10 wt.% SMI addition, the normalized phase shift ranged from 10 (at 0.01 Hz) to 100 times (at 1 Hz) higher than the untreated sediment (Figure 3.26c), and the normalized imaginary conductivity was 100 times (at 0.01 Hz) to 1000 times (at 1 Hz) higher than the untreated sediment (Figure 3.26d). SMI was easily quantified by SIP because the mixed iron phases had a high polarizability as has been observed previously in acid mine drainage and for minerals like pyrite (Placencia-Gómez et al. 2013, 2015; Placencia-Gómez and Slater 2016). Even at 0.3 wt.%, phase and imaginary conductivity shifts were easily quantified, with the SIP signal being linearly correlated with SMI content in sand across the frequency range (Table 3.6). The largest phase and imaginary conductivity values were at 1 Hz but the signal remained almost as high in the 1 to 100 Hz range. Further, unlike all other amendments tested, there was a frequency-specific increase in the real conductivity for the 10 wt.% SMI, which may be due to increasing surface conductivity as the solution conductivity signal in the real conductivity value is not frequency dependent (Figure 3.26b). Previous research measured adsorption of sodium to a high-surface-area silica gel and

reported an increase in real conductivity due to increases in the surface conductivity of as much as 70% (Hao et al. 2015).

SMI additions to Hanford formation sediment showed similar large (10 to 90 mrad, Figure 3.27a) phase shifts, with the normalized phase increase of 100 times (at 0.01 Hz) to 1000 times (at 100 Hz). In contrast, the increases in the imaginary conductivity were not as large and were predominantly in the 0.01 to 10 Hz range (Figure 3.27c) at up to 20 times the control sediment. However, the increases were also linearly correlated from 0.01 to 100 Hz (Table 3.7). The normalized imaginary conductivity showed an increase for the 1 wt.% and 10 wt.% SMI additions in the 0.01 to 1 Hz frequency range, then a decrease for all additions at a frequency of 1 to 10,000 Hz (Figure 3.27d). This was caused by the untreated Hanford sediment imaginary conductivity being greater than the SMI additions for frequencies above 10 Hz (Figure 3.27b), although the variability in the Hanford sediment background should be considered (Figure 3.1). Lastly, similar frequency-specific increases in the real conductivity for the 10 wt.% SMI were observed in both Hanford sediments and in sand.

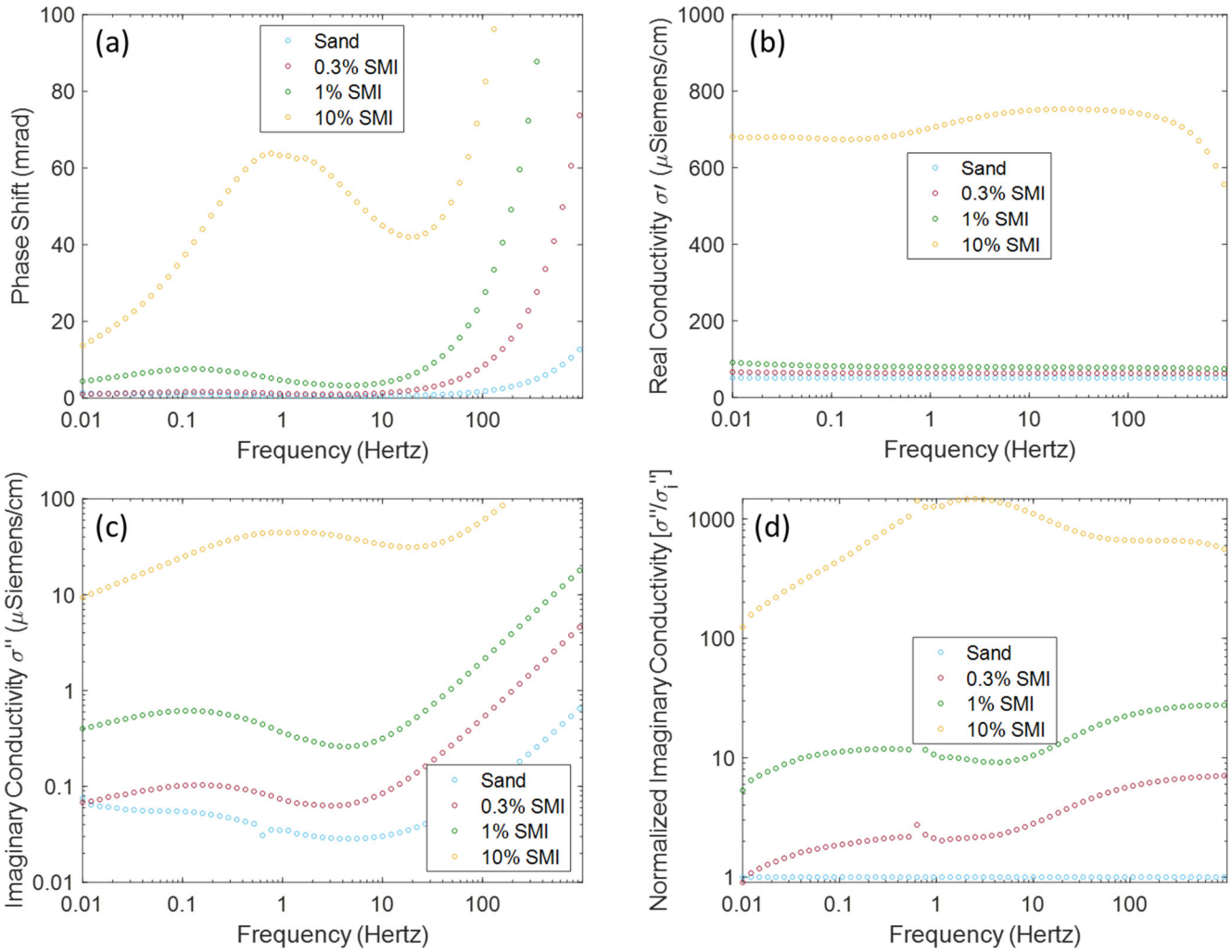

Figure 3.26. SIP measurements of SMI at variable wt.% added to sand saturated with AGW , as shown by (a) phase shift, (b) real conductivity, (c) imaginary conductivity, and (d) normalized imaginary conductivity, where *circles* represent the average response for each frequency.

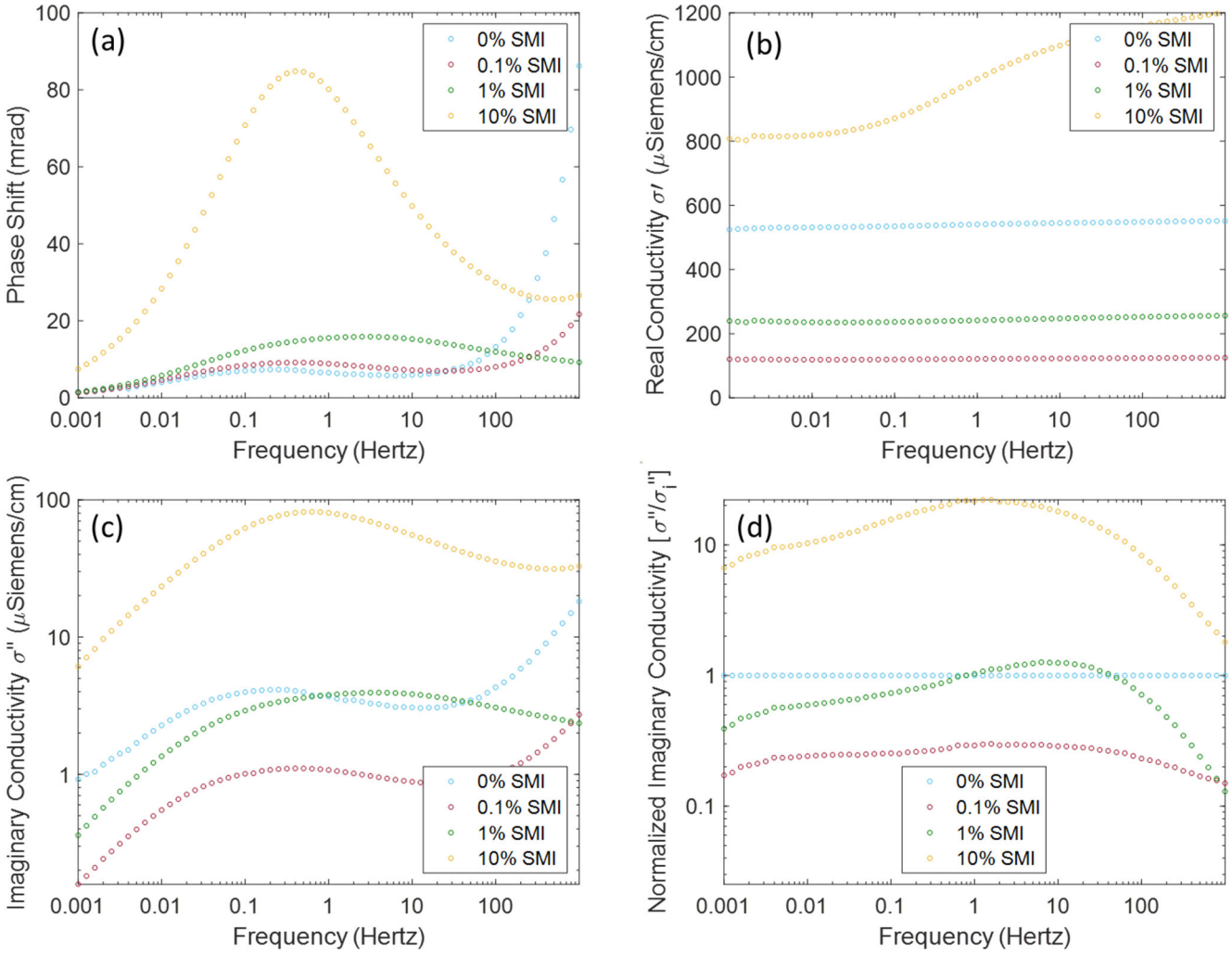

Figure 3.27. SIP measurements of SMI at variable wt.% added to Hanford formation sediment saturated with AGW, as shown by (a) phase shift, (b) real conductivity, (c) imaginary conductivity, and (d) normalized imaginary conductivity, where *circles* represent the average response for each frequency.

Table 3.6. Correlation of imaginary conductivity with variable wt.% of SMI mixed with sand or Hanford sediment across frequencies based on a linear fit, including the baseline without SMI.

Frequency (Hz)	Imaginary Conductivity (µS/cm) 0%	0.30%	1%	10%	R^2	Y=mX+B
Sand						
0.01	0.003	0.07	0.40	9.35	0.998	95.6x-0.2
0.1	0.006	0.10	0.62	25.4	0.996	261.1x-0.9
1	0.009	0.07	0.37	44.3	0.994	457.9x-1.8
10	0.018	0.08	0.32	33.4	0.994	344.8x-1.3
100	0.066	0.55	2.19	62.4	0.997	639.2x-1.8
1000	0.667	4.60	17.92	363	0.998	3700.8x-8.0
Hanford sediment						
0.01	2.28	0.55	1.35	23.4	0.986	226.6x+0.6
0.1	3.97	1.01	2.91	62.2	0.990	613.7x+0.5
1	3.69	1.08	3.79	80.3	0.993	798.1x+0.1
10	3.07	0.88	3.84	55.5	0.995	545.6x+0.7
100	4.31	1.00	3.07	35.7	0.985	338.6x+1.6
1000	18.2	2.72	2.36	32.9	0.690	249.9x+7.1

3.3.2.2 Changes in Sulfur Modified Iron Amendments over Time

SMI additions to both sand and Hanford formation sediments showed a consistent and strong SIP response after aging for 77 days in the absence of flow, as summarized in Figure 3.28 and Figure 3.29, and for Hanford sediments in shorter term experiments (up to 16 days) in Figure 3.30 and Figure 3.31. The most significant increases were observed in the 0.3 and 1.0 wt.% SMI (Table 3.7). The phase shift or imaginary conductivity changes show that the initial polarization increases with SMI additions. The exception for increasing surface polarization with time was for the 10 wt.% SMI with Hanford formation sediments, for which the imaginary conductivity decreased after 77 days, although an increase was observed in the short term (16 days). Furthermore, the frequency at which the maximum shifts and imaginary conductivity values were measured shifts to lower frequency with time (from approximately 1-3 to 0.2-0.5 Hz, Table 3.7) which is consistent with a change in mineralogy, adsorption of iron, or physical changes in particle size and porosity.

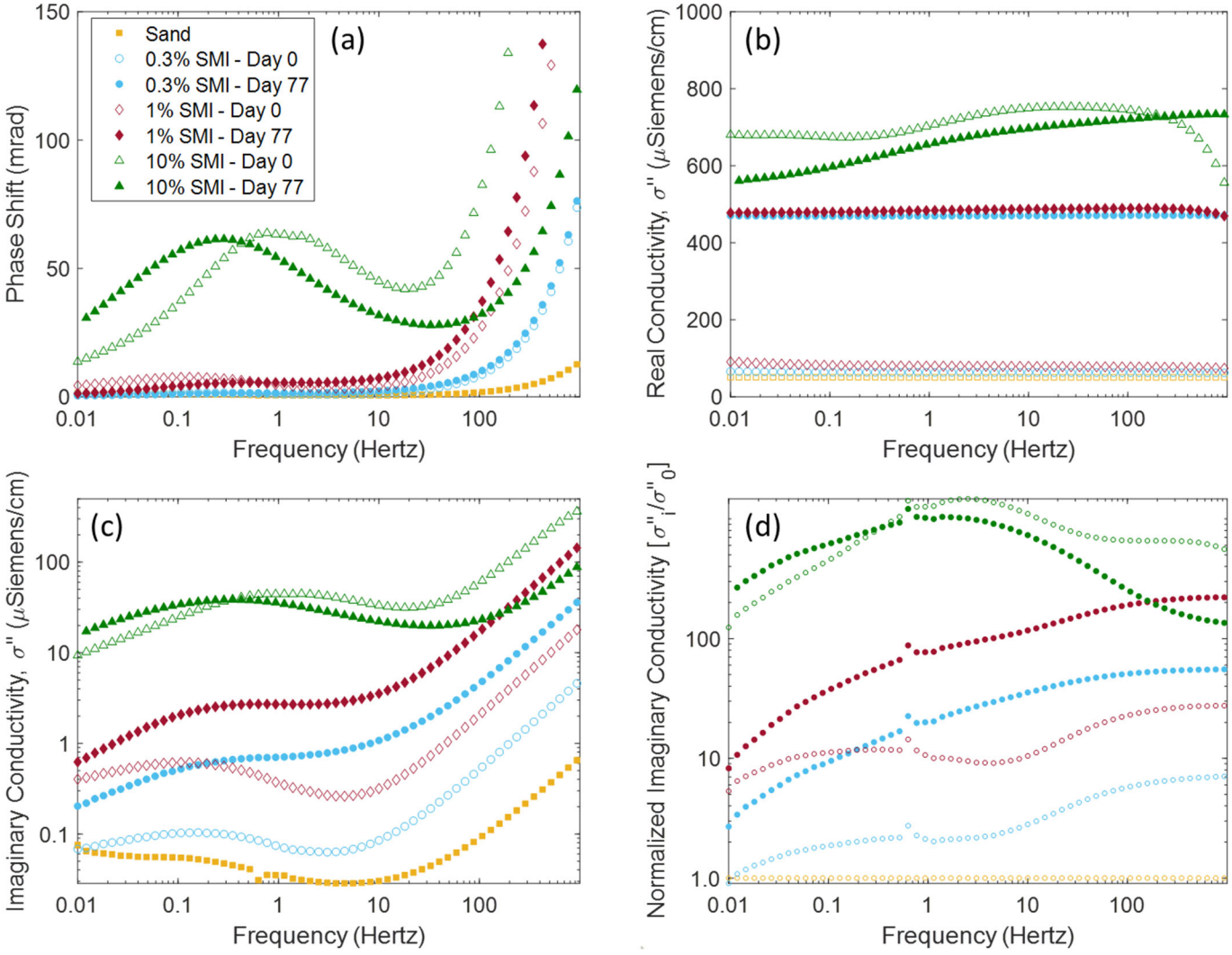

Figure 3.28. SMI in sand saturated with AGW with measurements at time zero and after 77 days of aging in the absence of water flow with (a) phase shift in mrad, (b) real conductivity, (c) imaginary conductivity, and (d) normalized imaginary conductivity with respect to sediment without amendment, where *circles* represent the average response for each frequency.

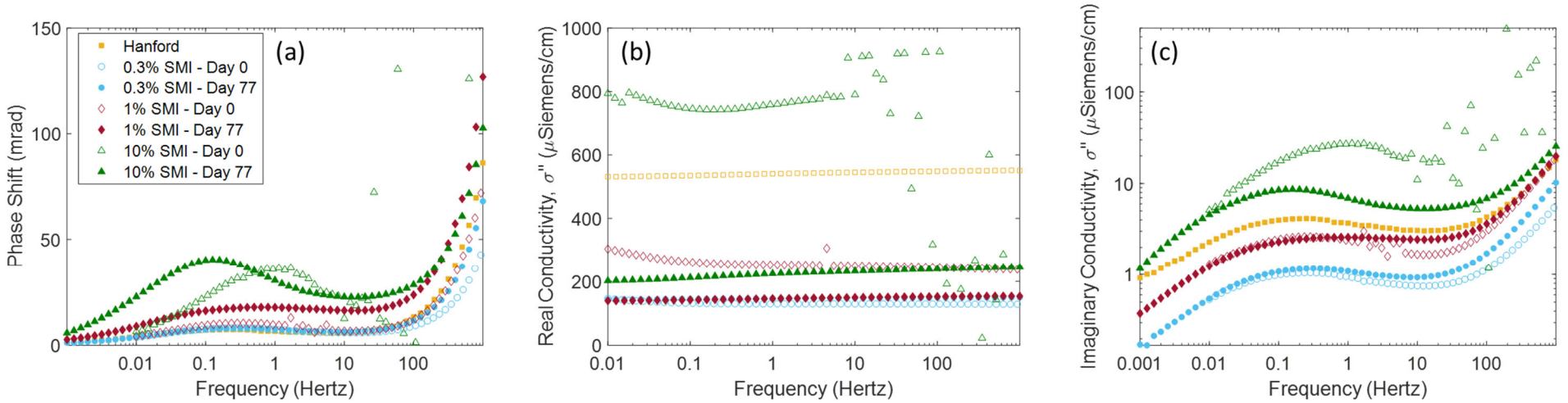

Figure 3.29. SMI in Hanford formation sediments saturated with AGW with measurements at time zero and after 77 days of aging in the absence of water flow with (a) phase shift in mrad, (b) real conductivity, and (c) imaginary conductivity in µS/cm, where *circles* represent the average response for each frequency.

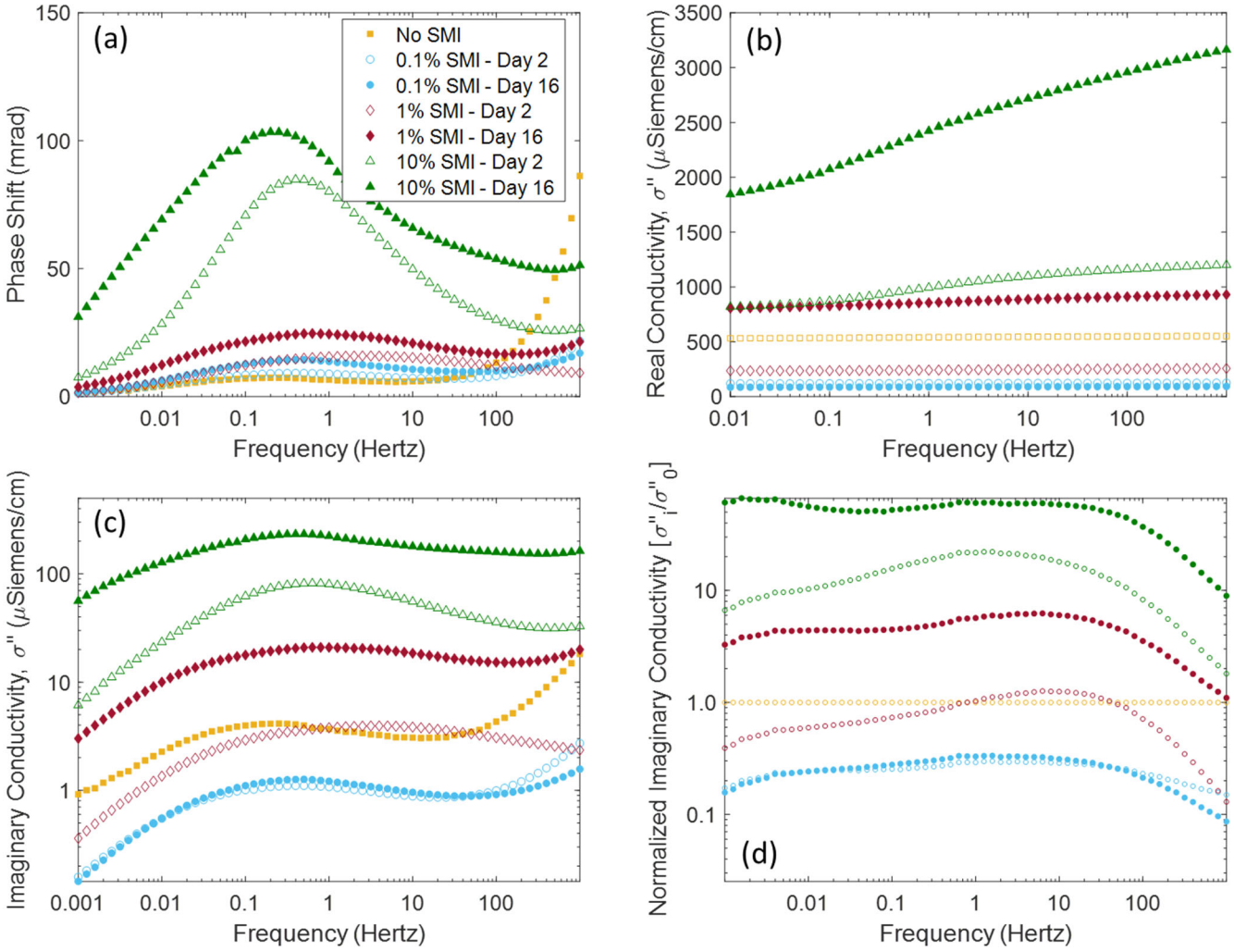

Figure 3.30. SMI in Hanford formation sediments saturated with AGW with measurements over short-term aging up to 16 days in the absence of water flow with (a) phase shift in mrad, (b) real conductivity, (c) imaginary conductivity in µS/cm, and (d) normalized imaginary conductivity, where *circles* represent the average response for each frequency.

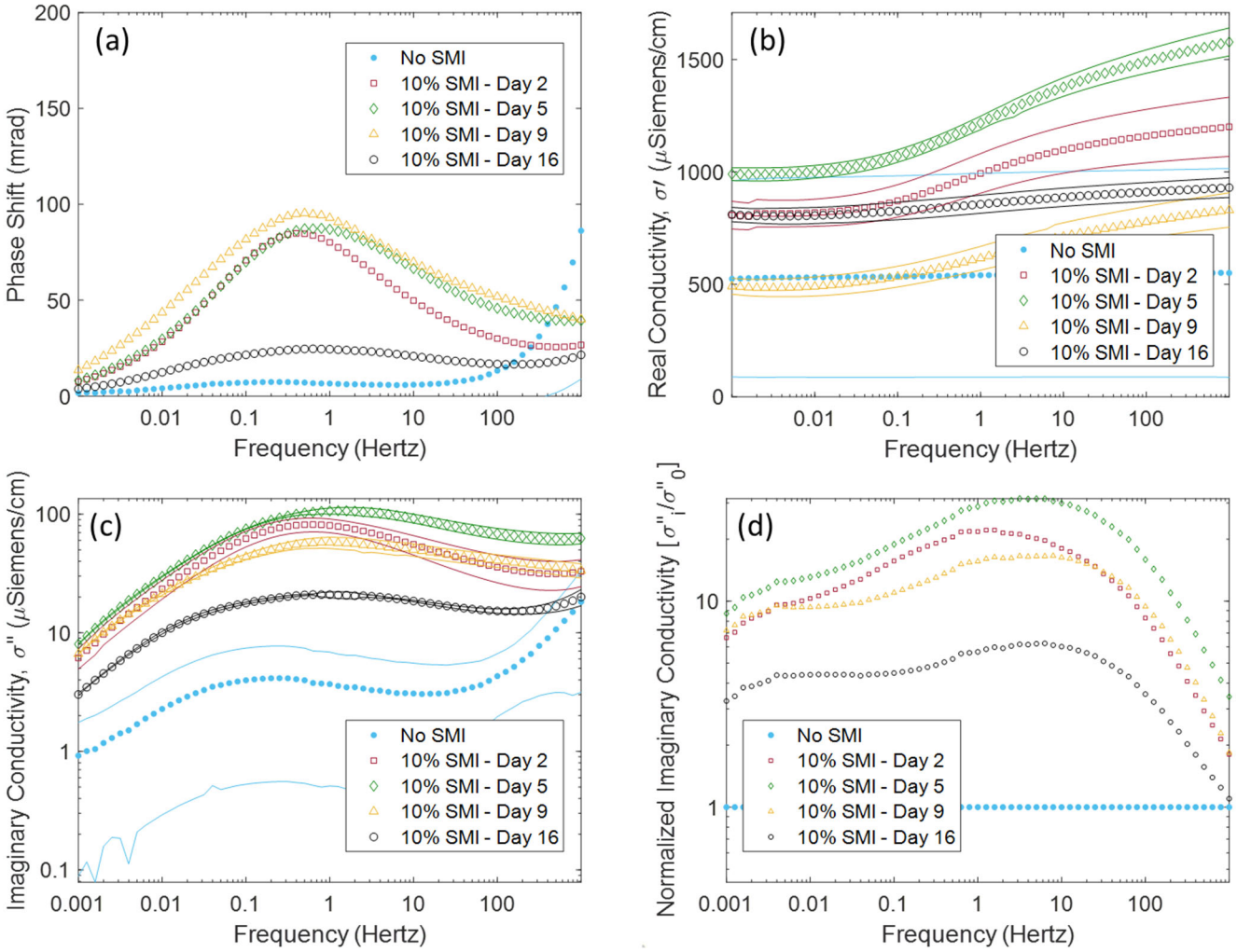

Figure 3.31. SMI at 10 wt.% as monitored for change over time with short term aging for 16 days, packed in Hanford formation sediments saturated with AGW with (a) phase shift in mrad, (b) real conductivity, (c) imaginary conductivity in µS/cm, and (d) normalized imaginary conductivity, where *lines* represent 95% CIs from triplicate loops of data across frequency (triplicate columns and loops for the control without SMI) for each column and *circles* represent the average response for each frequency.

Table 3.7. Summary of SIP changes over time to SMI additions to sediments.

Matrix	Amendment, wt.%	Phase Shift (mrad)[a]	Imaginary Conductivity (µS/cm)[a]	Frequency of Maxima (Hz)
Sand	0.3 SMI, 77 days	40% increase	1100% increase	0.3/1.0[b]
	1 SMI, 77 days	80% increase	1000% increase	0.3
	10 SMI, 77 days	No change	No change	1/0.3[b]
Hanford formation	0.1 SMI, 16 days	60% increase	20% increase	0.5
	0.3 SMI, 77 days	No change	No change	0.3
	1 SMI, 16 days	50% increase	400% increase	3/0.5[b]
	1 SMI, 77 days	70% increase	No change	0.5
	10 SMI, 16 days	20% increase	180% increase	0.4/0.2[b]
	10 SMI, 77 days	15% increase	65% decrease	1/0.4[b]

(a) Maximum phase shift and conductivity as observed below 10 Hz.
(b) Two values listed if frequency of maxima changed over time (time zero/day 77).

3.3.3 Summary of Iron and Sulfur Amendment Responses Observed via SIP

Two different amendments used in this study (ZVI and SMI) exhibited significant phase shift and imaginary conductivity responses upon addition to silica sand and Hanford formation sediments. These SIP changes differed between the amendments, which reflected the amendment mineralogy (and intrinsic electrical semi-conductor properties) as well as physical differences in particle size and porosity. Iron sulfide minerals have previously been noted as having high sensitivity for detection at field scale (Orozco et al. 2011; Placencia-Gómez et al. 2015; Williams et al. 2009), and ZVI had high sensitivity for detection in laboratory experiments (Mellage et al. 2018; Wu et al. 2009). Preliminary results for FeS detection by SIP are also included in Appendix D compared to other work.

The ZVI used in this study was 79% ZVI, 9% magnetite, 8% quartz, and 4.4% wüstite (Table 2.2). In aqueous solution, the ZVI oxidizes over time, forming mixed ferrous and ferric iron minerals. The SMI has a similar mineralogy to ZVI, with 60% ZVI, 33% magnetite, and 7% FeO (with a trace of sulfur on the surface that was not detectable by XRD but was previously characterized by Mossbauer – Lawter et al. 2018). In this study, the observed phase shift associated with SMI addition was greater than that for ZVI addition to sand or Hanford formation sediment. Under ideal conditions with closely spaced electrodes, the detection limit was previously estimated at 0.5 mrad (Szecsody et al. 2020a), so ZVI and SMI might be detected to 0.05 wt.% in sand. The detection limits in Hanford formation sediments are more challenging to estimate due to the greater background SIP signal. For the ZVI and SMI samples used in this study, the frequency range of the SIP response differed. For ZVI, the > 100 Hz frequency range was most sensitive, whereas for the SMI, the lower frequency range from 0.01 to 10 Hz was most sensitive. In all cases, ZVI and SMI resulted in a positive increase in the imaginary conductivity at some point in the frequency range investigated, meaning the amended sediment had a greater surface polarization that could be detected via SIP.

3.4 Dual Amendment Testing

3.4.1 Batch *In Situ* Calcite Co-precipitation with Sediments and ZVI

Batch precipitation experiments were conducted in which ammonium carbonate [$(NH_4)_2CO_3$] and calcium chloride [$CaCl_2$] were mixed in the presence of Hanford formation sediments with or without ZVI-1 (1 wt.%) to form 16 wt.% calcite. Due to the presence of the high ionic strength solution, the phase shift at high frequencies (> 100 Hz) was likely due to Maxwell Wagner polarization and parasitic capacitive coupling of the SIP instrument (Figure 3.32a) and therefore not related to the sediment or calcite

precipitates. However, the phase shift is clearly decreased for both samples with calcite co-precipitated (Figure 3.32a – 'Sediment + Calcite' and 'Sediment + ZVI + Calcite'). This could be attributed to calcite coating sediment minerals decreasing the surface capacitance. These results are consistent with a study that observed that calcite precipitation over long periods of time (laboratory experiments with > 400 pore volumes of injection of calcite-saturated groundwater) on the ZVI surface decreased the electrical conductivity (Wu et al. 2009). This phenomenon was not apparent in samples where calcite is separately precipitated and then mixed with Hanford formation sediments (Section 3.2.2, Figure 3.14). While the imaginary conductivity decreased slightly with calcite, these data were not significantly different considering the 95% CIs, nor did they correlate with added calcite concentrations.

The imaginary conductivity showed that, for calcite precipitation, there was an increase of 0.2 to 2 µS/cm in the 0.001 to 0.01 Hz range (Figure 3.32b), although this increase was not observed with ZVI and calcite. The increase in low-frequency conductivity is consistent with previous work that noted a similar change in imaginary conductivity due to an increase in surface area from calcite precipitation (Saneiyan et al. 2018). There was also a significant increase in the imaginary conductivity at frequencies > 1 Hz for the sediment with ZVI and similar but slightly less for sediment with ZVI and calcite (Figure 3.32b,c). However, these results are different than reported for *in situ* precipitation of calcite with and without ZVI where a decrease in imaginary conductivity was observed (Wu et al. 2009, 2010). Moreover, these results are consistent with previous work reporting a higher frequency response for ZVI in both the nano and micron size fraction (Abdel Aal et al. 2014; Szecsody et al. 2020a), although the significant increases in the kHz range may be due to capacitive coupling of the SIP instrument (Wang and Slater 2019).

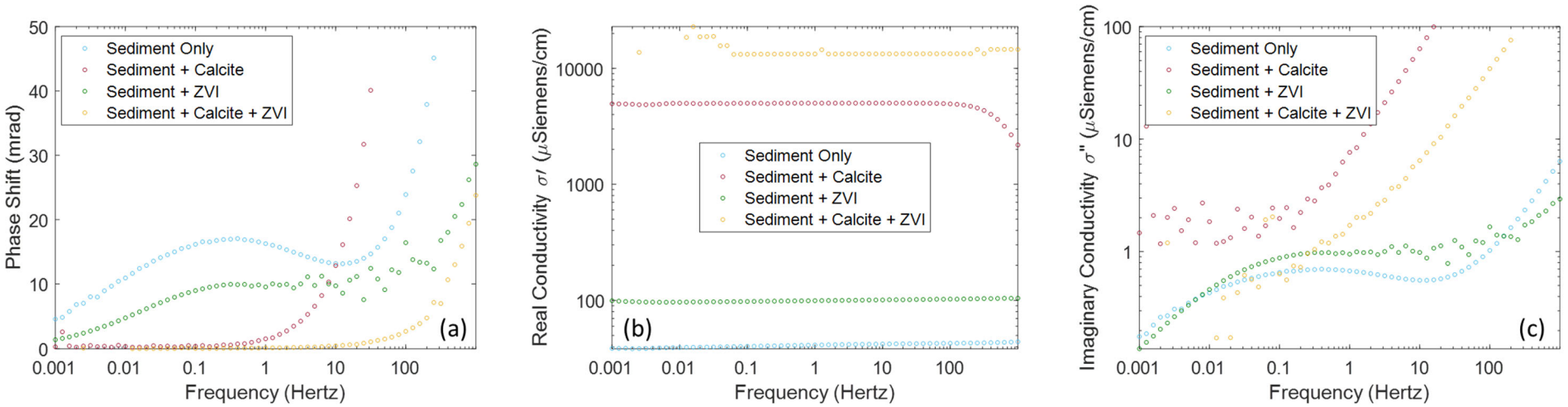

Figure 3.32. Calcite co-precipitated (16 wt.%) in the presence of Hanford formation sediments saturated with AGW with and without 1 wt.% ZVI with (a) phase shift in mrad, (b) real conductivity, (c) imaginary conductivity in µS/cm, where *circles* represent the average response for each frequency for three loops of data collected.

Table 3.8. Post characterization results for total inorganic carbon and water content from *in situ* precipitation of calcite with and without ZVI in a batch setup where calcite content is estimated based on total inorganic carbon measurements assuming all is present as calcite.

Description	Inorganic Carbon (%)	Calcite (%)	Water Content (%)
Sediment + Calcite	1.24	10.33	14.4
Sediment + Calcite + ZVI	1.3	10.83	14.8
Sediment + ZVI	0.05	0.42	13.2
Sediment control	0.05	0.42	16.6

3.4.2 Batch *In Situ* Calcite Co-precipitation with Sediments and SMI

Similar to Section 3.4.1, calcite was precipitated from solution in the presence of sediment and SMI as described in Appendix A, Section A.1.2. As observed with ZVI, the phase shift decreased when calcite was present both with and without SMI (Figure 3.33). In addition, SMI with calcite initially exhibited the largest imaginary conductivity as compared to without calcite and without SMI. Although less pronounced, increases were also observed for imaginary conductivity when reacted with calcite-forming solutions.

Once the solids were packed into columns, they were monitored over 32 days in the absence of flow. It should be noted that changes were also not observed in the sediment control with time (*not shown*). For the 1% SMI in sediments, significant changes were not observed in real and imaginary conductivity. However, the phase shifts suggest some changes in surface polarization based on changes in magnitude and peak frequency. These results were consistent with previous results where changes were most pronounced for 10 wt.% SMI (Figure 3.29 to Figure 3.31).

For calcite precipitated in the presence of sediment, little change was observed with time for phase shift and conductivity (Figure 3.34). However, the real conductivity decreased by almost an order of magnitude, suggesting that additional precipitation, potentially of calcite, occurred within the column. For the calcite precipitated in the presence of SMI and sediment (Figure 3.36), a more significant decrease to that observed without SMI (almost two orders of magnitude) was observed in both real and imaginary conductivity with time, suggesting precipitation of calcite continued to occur in the column during monitoring. These results are consistent with previous observations for calcite precipitated in a ZVI barrier material (Wu et al. 2009).

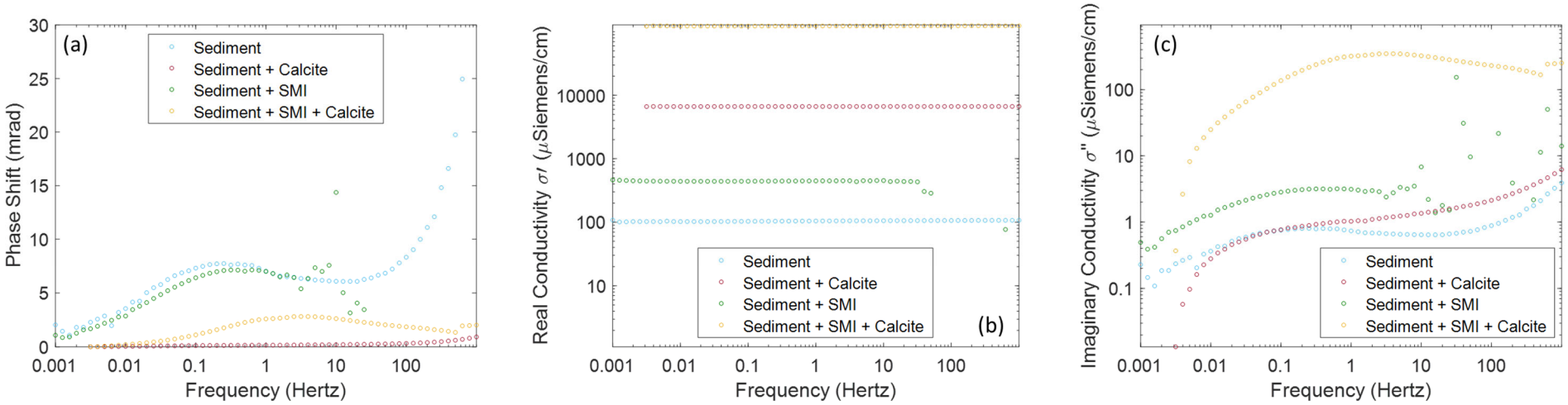

Figure 3.33. Calcite co-precipitated (16 wt.%) in the presence of Hanford formation sediments saturated with AGW with and without 1 wt.% SMI after three days of reaction with (a) phase shift in mrad, (b) real conductivity, (c) imaginary conductivity in µS/cm, where *circles* represent the average response for each frequency for three loops of data collected.

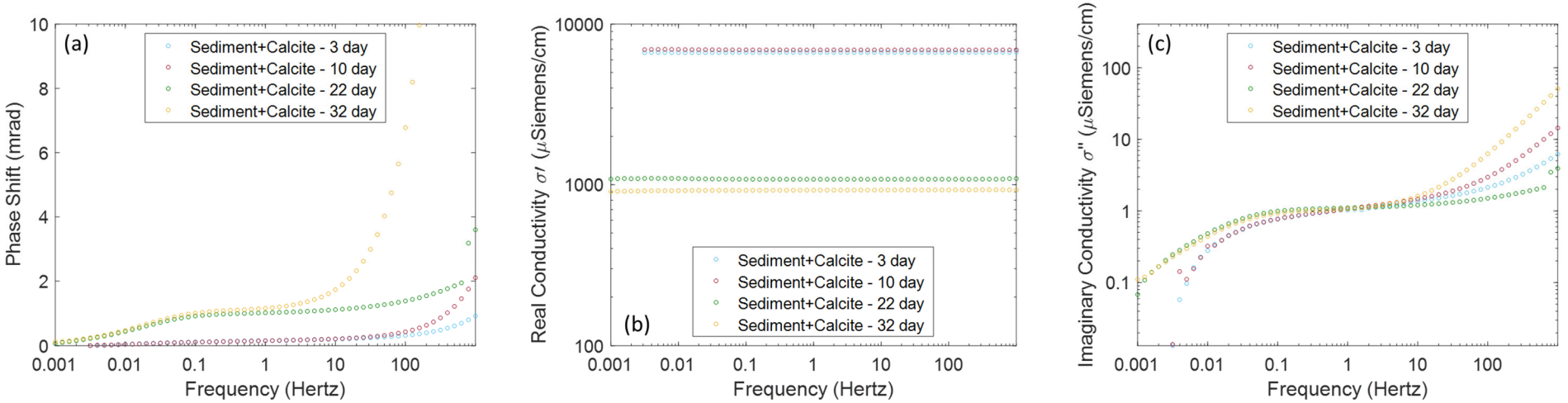

Figure 3.34. Calcite co-precipitated (16 wt.%) in the presence of Hanford formation sediments saturated with AGW over one month of reaction with (a) phase shift in mrad, (b) real conductivity, (c) imaginary conductivity in µS/cm, where *circles* represent the average response for each frequency for three loops of data collected.

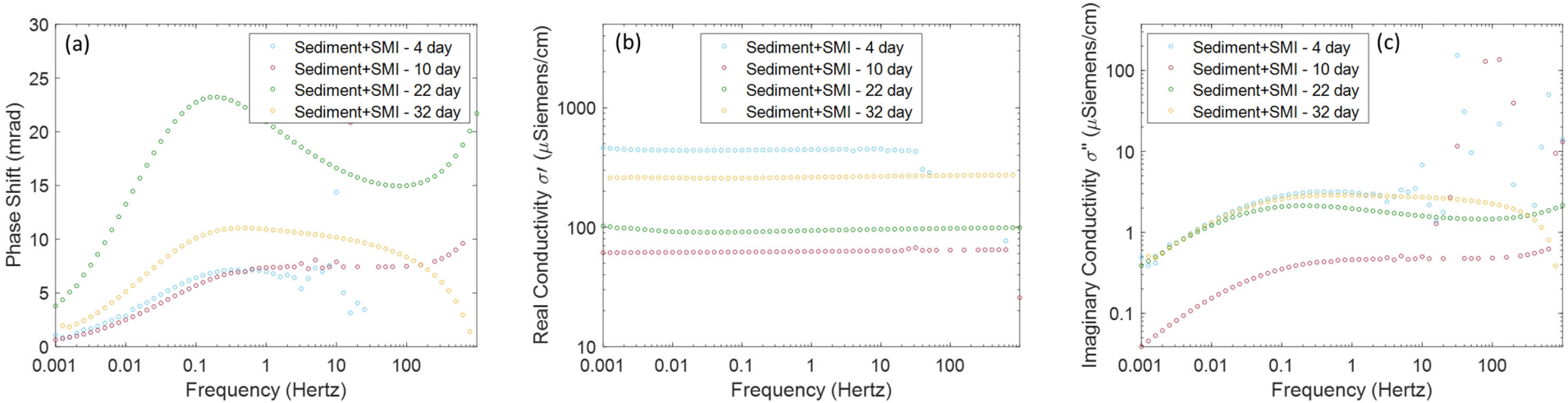

Figure 3.35. 1% SMI in the presence of Hanford formation sediments saturated with AGW over one month of reaction with (a) phase shift in mrad, (b) real conductivity, (c) imaginary conductivity in µS/cm, where *circles* represent the average response for each frequency for three loops of data collected.

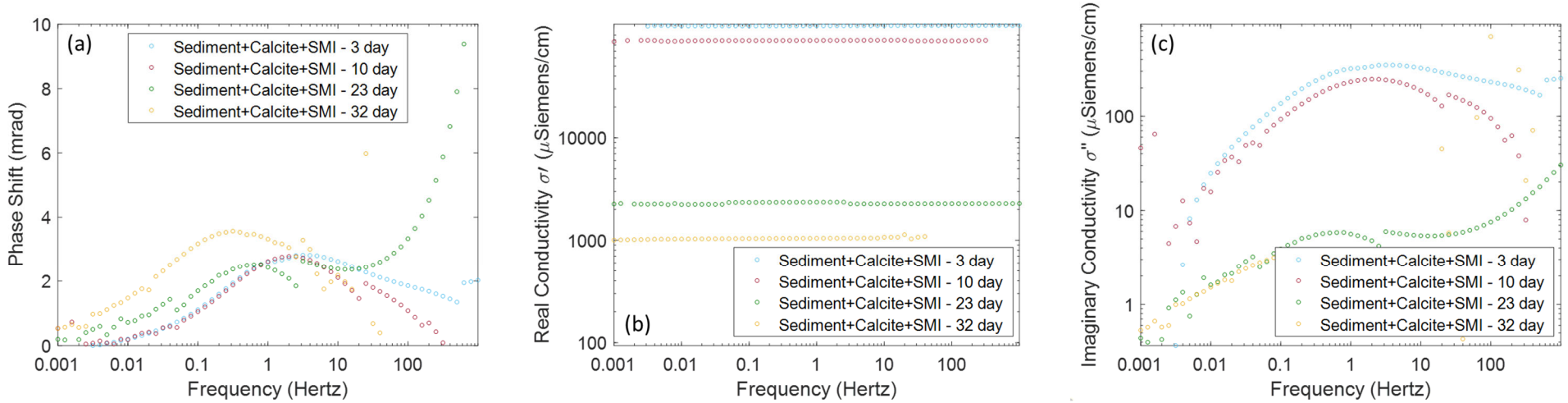

Figure 3.36. Calcite co-precipitated (16 wt.%) in the presence of Hanford formation sediments with 1% SMI saturated with AGW over one month of reaction with (a) phase shift in mrad, (b) real conductivity, (c) imaginary conductivity in µS/cm, where *circles* represent the average response for each frequency for three loops of data collected.

Table 3.9. Post characterization results from *in situ* precipitation of calcite with and without SMI in a batch setup where calcite content is estimated based on total inorganic carbon measurements assuming all is present as calcite.

Sample ID	Inorganic Carbon (%)	Calcite (%)	Moisture Content (%)
Sediment	0.056±0.004	0.47	20.9
Sediment + Calcite	1.18±0.42	9.83	18.6
Sediment + SMI	0.055±0.013	0.46	20.9
Sediment + SMI + Calcite	1.02±0.09	8.5	19

3.4.3 Column *In Situ* Calcite Co-precipitation with Sediments and SMI

To further test the difference between pre-mixing and coating sediment and SMI particles with calcite, an experiment was conducted over 130 days where changes in variable concentrations of SMI packed in layers in a column (as shown in Figure 3.37) were first monitored for approximately 60 days under constant injection of AGW prior to injection of calcite-forming solutions as described in Appendix A, Section A.1.3. Initial measurements of SMI were similar to that observed in smaller columns from 0.1 to 10 wt.% (Figure 3.27). Although the 100 wt.% SMI was not measured in previous experiments in small columns, the increase is approximately an order of magnitude (1000 μS/cm) as shown in Figure 3.38, highlighting that significant polarization occurs with increasing concentration as shown previously for ZVI and iron sulfide (Joyce et al. 2012; Wu et al. 2005; Placencia-Gomez et al. 2013, 2015). For the 100 wt.% SMI, there is also a significant increase in real conductivity, suggesting an increase in surface conductivity as compared to the sediment and mixtures of sediment with SMI. Lastly, in the additional initial measurements taken five days after saturation, each of the sediment layers exhibit a similar small response for phase shifts and imaginary conductivity (Figure 3.39).

Based on the previous SMI data, the range of frequency of data collection was shortened from 0.001 to 10,000 Hz to 0.01 to 10,000 Hz as peaks were generally observed above 0.01 Hz. However, as shown in Figure 3.40, some of the features are lost for 10 wt.% SMI in the low frequency range as it is unclear if the peaks are reached for phase shifts at 0.01 Hz. It should be noted that the features seem to be covered for 1.0 and 0.1 wt.% SMI as shown in Appendix F in Figure F.1 and Figure F.2. Regardless, significant changes in phase shift or imaginary conductivity are not observed over the course of these experiments with the exception of a significant increase in real and imaginary conductivity immediately following injection of calcite-forming solutions. This is consistent with the measured increase in solution conductivity in effluent samples (Figure 3.42), with the increase in imaginary conductivity likely due to additional ions in the EDL from the increased bulk solution conductivity.

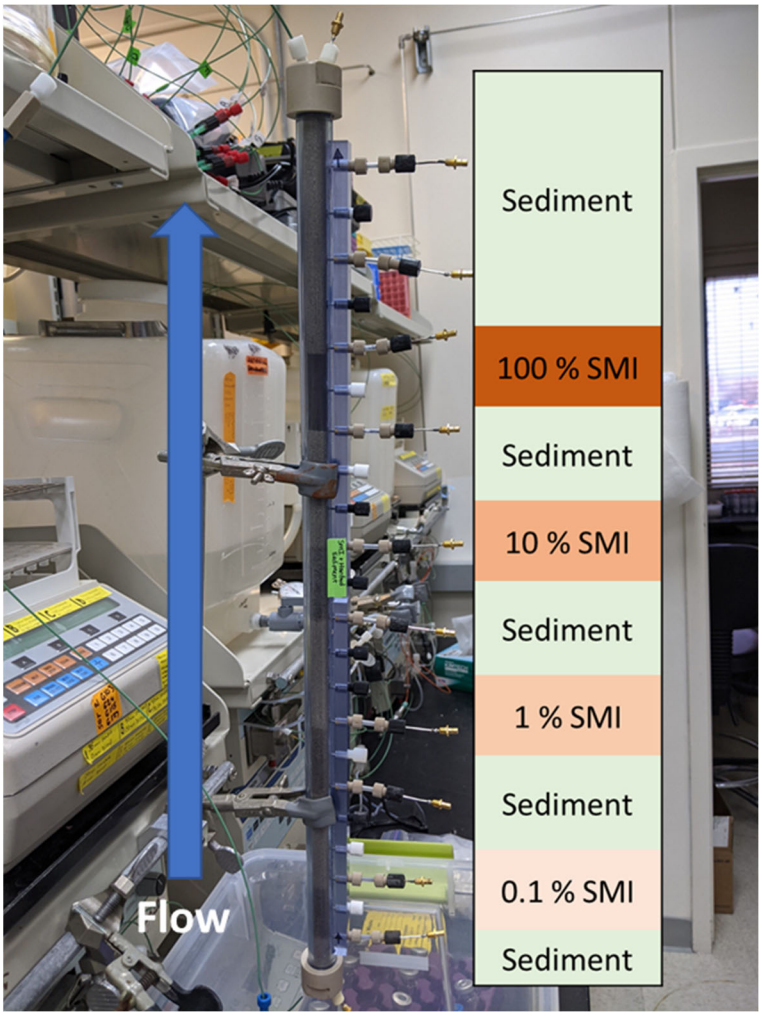

Figure 3.37. Photograph of column with variable concentrations of SMI packed with Hanford sediments as shown in layer descriptions on the left with pairs of SIP electrodes across each layer.

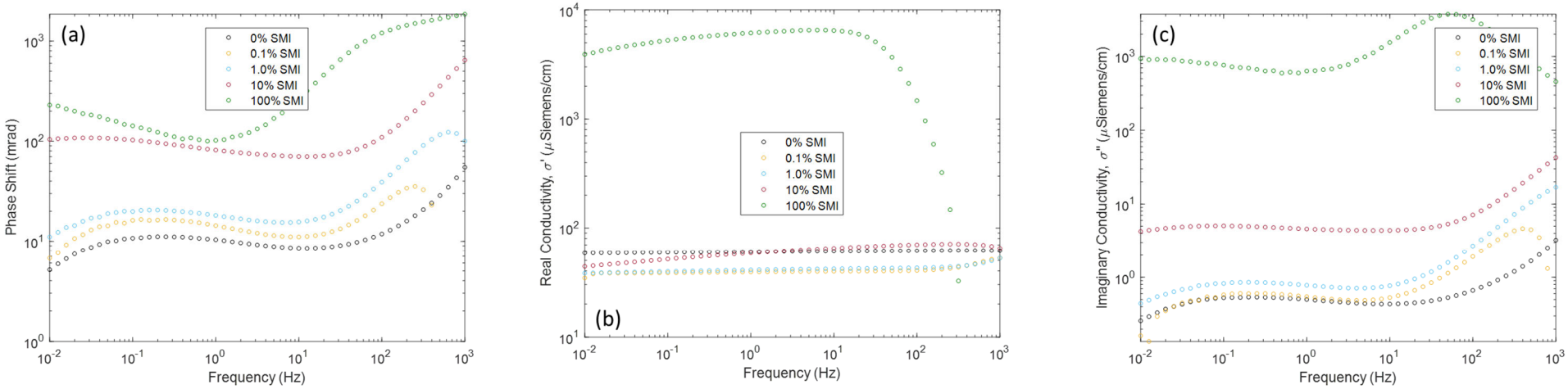

Figure 3.38. Hanford formation sediments in layers with variable wt.% of SMI saturated with AGW in a 24-in. length by 0.5-in. ID column with (a) phase shift in mrad, (b) real conductivity, (c) imaginary conductivity in µS/cm, where *circles* represent the measurement for each frequency at five days after saturation.

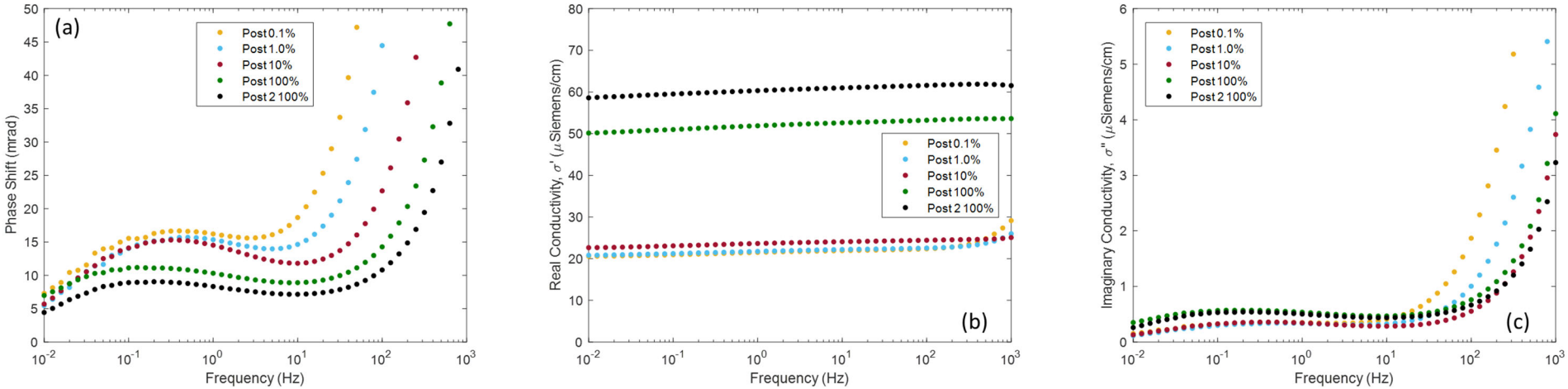

Figure 3.39. Hanford formation sediment layers following the variable wt.% of SMI layers saturated with AGW in a 24-in. length by 0.5-in. ID column with (a) phase shift in mrad, (b) real conductivity, (c) imaginary conductivity in µS/cm, where *circles* represent the measurement for each frequency at five days after saturation.

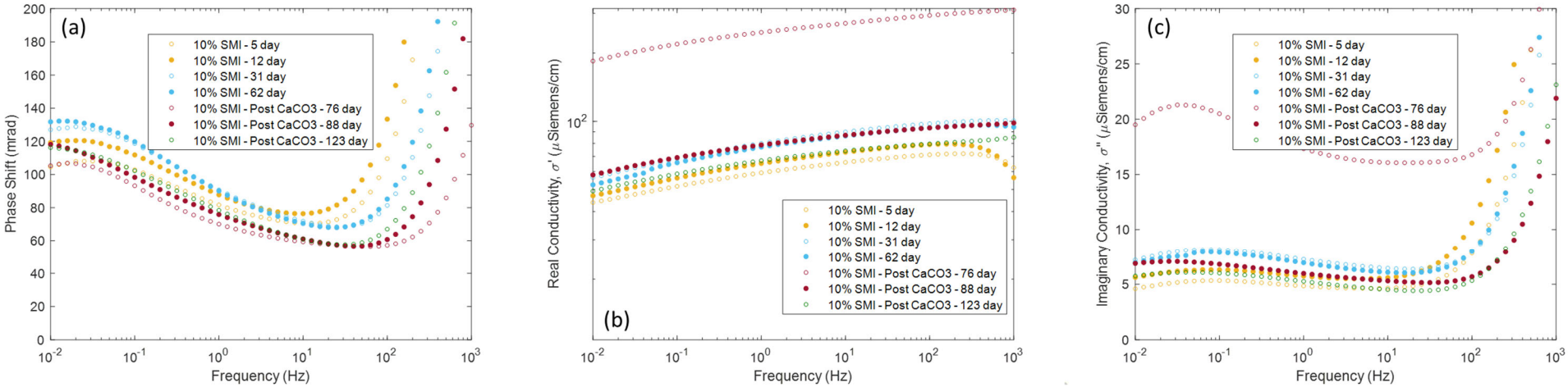

Figure 3.40. Change in SIP response over time for 10 wt.% SMI with Hanford sediment saturated with AGW followed by injection of calcite forming solutions (70-75 days) and then flushing with AGW in a 24-in. length by 0.5-in. ID column with (a) phase shift in mrad, (b) real conductivity, (c) imaginary conductivity in µS/cm, where *circles* represent the measurement for each frequency at five days after saturation.

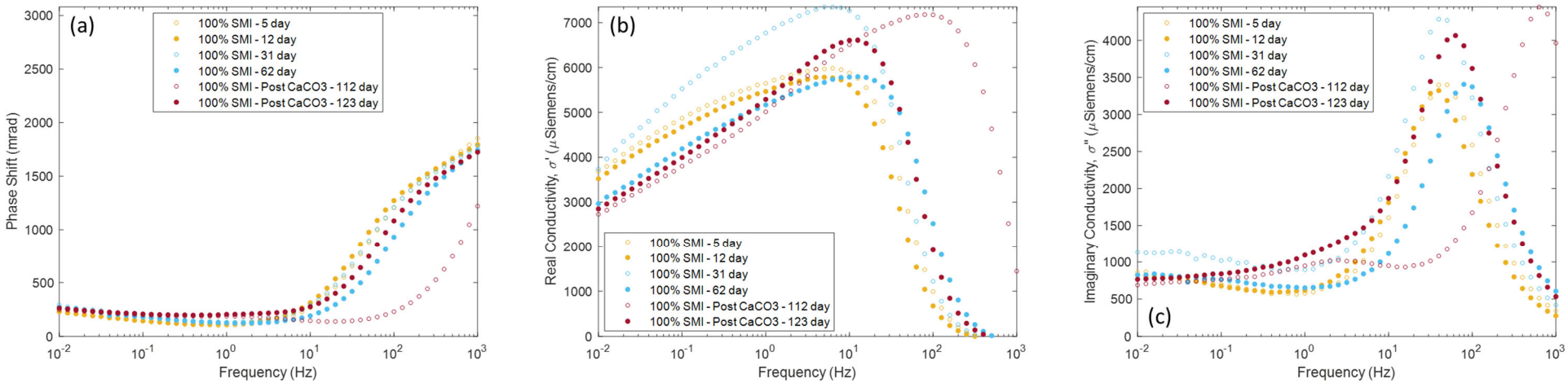

Figure 3.41. Change in SIP response over time for 100 wt.% SMI with Hanford sediment saturated with AGW followed by injection of calcite forming solutions (70-75 days) and then flushing with AGW in a 24-in. length by 0.5-in. ID column with (a) phase shift in mrad, (b) real conductivity, (c) imaginary conductivity in µS/cm, where *circles* represent the measurement for each frequency at five days after saturation.

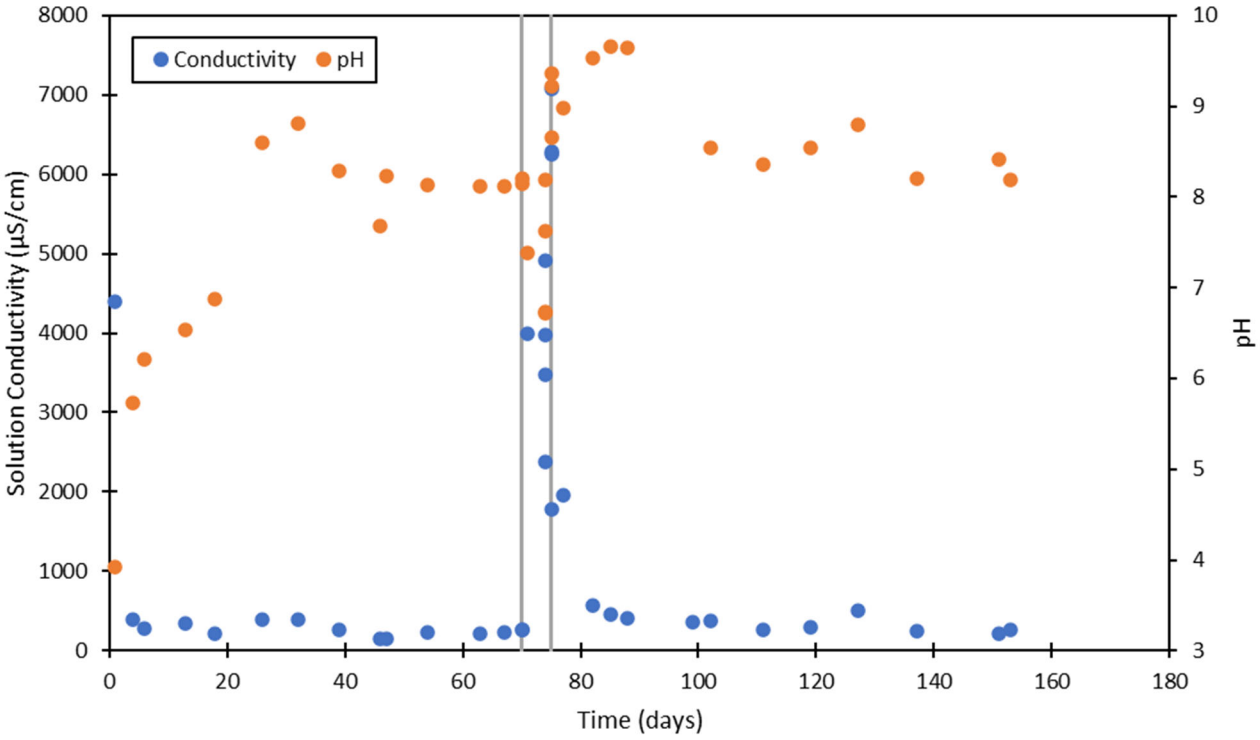

Figure 3.42. Effluent monitoring of solution conductivity (µS/cm) and pH over time following collection in anaerobic bottles where AGW was continuously injected for 69 days, followed by injection of calcite forming solutions (70-75 days, in between *gray* lines), followed by flushing with AGW.

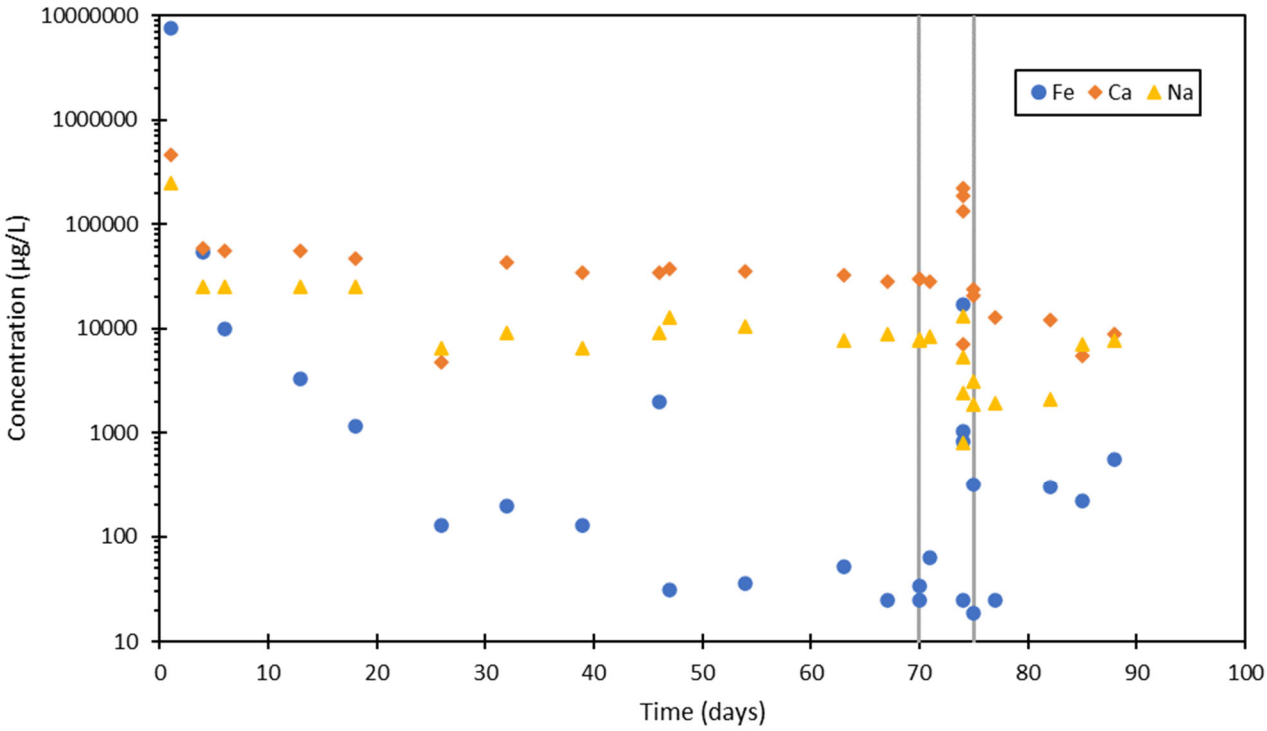

Figure 3.43. Effluent monitoring of major elements in solution (µg/L) over time following collection in anaerobic bottles where AGW was continuously injected for 69 days, followed by injection of calcite-forming solutions (70-75 days, in between *gray* lines), followed by flushing with AGW.

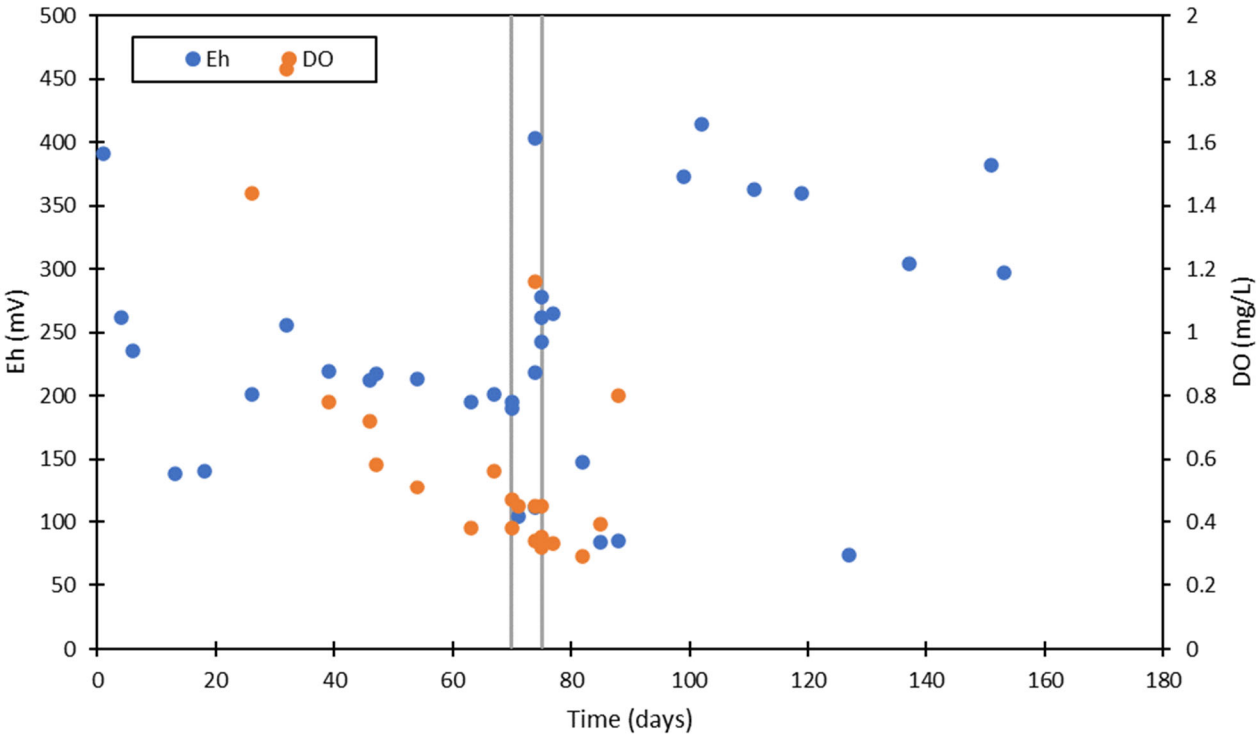

Figure 3.44. Effluent monitoring of redox conditions over time following collection in anaerobic bottles where AGW was continuously injected for 69 days, followed by injection of calcite-forming solutions (70-75 days, in between *gray* lines), followed by flushing with AGW.

3.4.4 Column *In Situ* Apatite Co-precipitation with Sediments and SMI

In situ injection of polyphosphate in a column packed with variable wt.% SMI with Hanford sediments (as depicted in Figure 3.37) was conducted to investigate the potential for monitoring dual remediation with SMI followed by polyphosphate injection and is compared with previous data, including the polyphosphate injection into a 24-in. column conducted only with sediments described in Section 3.2.1.3 and the variable SMI experiments conducted in 4-in. columns as described in Section 3.3.2.

Initially, the response was linearly correlated for variable wt.% of SMI as shown for previous results with 4-in. columns (Table 3.6). Prior to injection of polyphosphate solutions at 62 days, sediment and SMI layers were monitored as shown in Figure 3.46 to Figure 3.49. Little change was observed for lower SMI concentrations (Appendix F, Figure F.6 and Figure F.7) and for sediment layers following the lower concentrations of SMI (Figure F.8 and Figure F.9). However, similar to results reported in Section 3.3.2.2, a change in the magnitude and frequency of the maximum was observed for 10 wt.% SMI with a shift to lower frequency over time (Figure 3.46). An increase in the magnitude was also observed for 100 wt.% SMI in the low frequency (< 1 Hz), although a peak maximum was not observed as the phase shifts increased with decreasing frequency below 1 Hz. The imaginary conductivity also increased some across the frequency range. For the two sediment layers following the 100 wt.% SMI, an increase in phase shift and imaginary conductivity was also observed with time, likely due to oxidation, dissolution, and secondary precipitation of iron from SMI in the preceding 100 wt.% SMI layer (Figure 3.48 and Figure 3.49). These results are consistent with the significant increase in surface area of 10 and 100 wt.% SMI

(Table 3.10) in sediments characterized post experiments as compared to baseline sediment and SMI surface area (Table 2.1 and Table 2.3) prior to column experiments.

After addition of polyphosphate solutions, the real and imaginary conductivity increased significantly in the 10 wt.% SMI layer consistent with an increase in solution conductivity (Figure 3.50). This is consistent with the high conductivity of the polyphosphate solution, although the major release of ions in effluent was not observed until flushing with AGW was initiated at 102 days. After injection of polyphosphate solutions, phase shifts and imaginary conductivity decreased significantly in the low frequency range, consistent with formation of a low-conductivity mineral phase. These results are different from those observed on sediments without SMI (Figure 3.7) where phase shifts and imaginary conductivity increased slightly with apatite treatment, highlighting that the coating of sediment versus SMI with apatite affects the EDL in different ways.

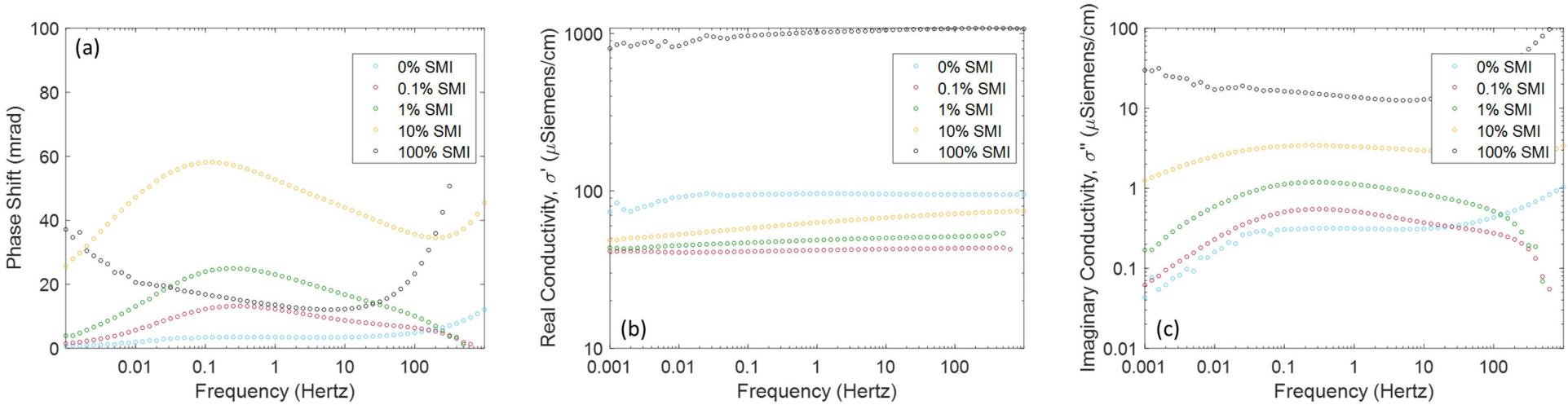

Figure 3.45. Hanford formation sediments in layers with variable wt.% of SMI saturated with AGW in a 24-in. length by 0.5-in. ID column with (a) phase shift in mrad, (b) real conductivity, (c) imaginary conductivity in µS/cm, where *circles* represent the measurement for each frequency at 3 days after saturation.

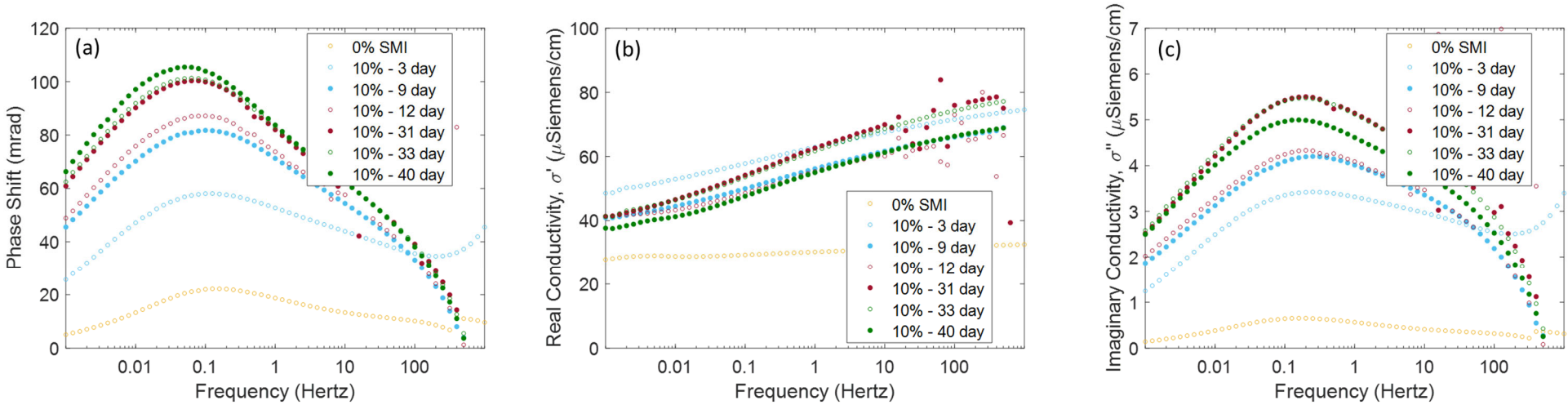

Figure 3.46. Layer of Hanford formation sediments with 10 wt.% of SMI saturated with AGW in a 24-in. length by 0.5-in. ID column as measured over 40 days with constant flow at 0.025 mL/min prior to injection of polyphosphate solutions, with (a) phase shift in mrad, (b) real conductivity, (c) imaginary conductivity in µS/cm, where *circles* represent the measurement for each frequency.

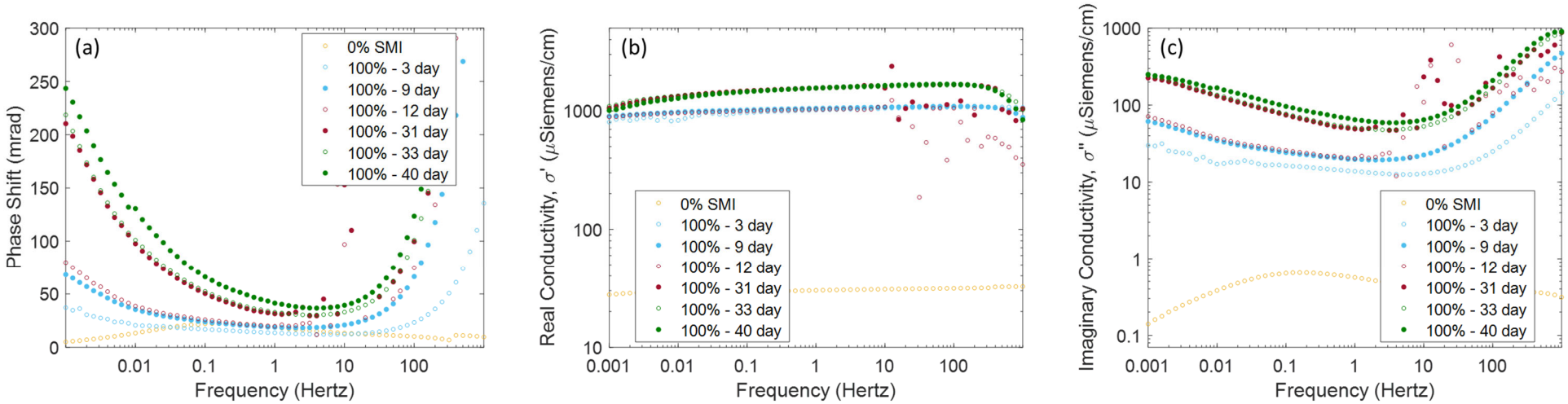

Figure 3.47. 100 wt.% of SMI layer saturated with AGW in a 24-in. length by 0.5-in. ID column as measured over 40 days with constant flow at 0.025 mL/min prior to injection of polyphosphate solutions, with (a) phase shift in mrad, (b) real conductivity, (c) imaginary conductivity in µS/cm, where *circles* represent the measurement for each frequency.

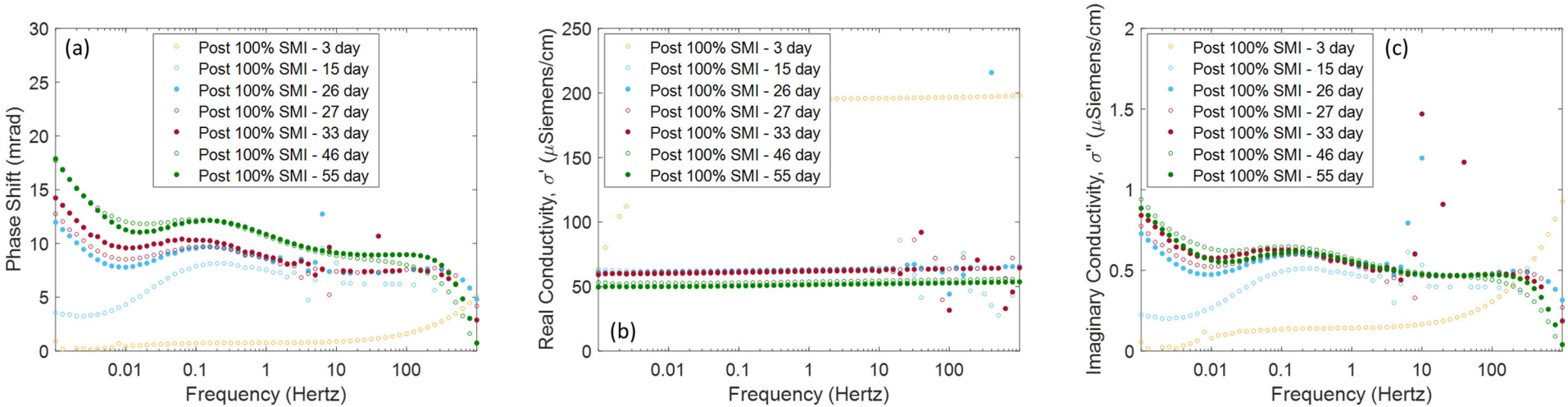

Figure 3.48. Hanford sediment layer directly after 100 wt.% of SMI layer saturated with AGW in a 24-in. length by 0.5-in. ID column as measured over 55 days with constant flow at 0.025 mL/min, with (a) phase shift in mrad, (b) real conductivity, (c) imaginary conductivity in µS/cm, where *circles* represent the measurement for each frequency.

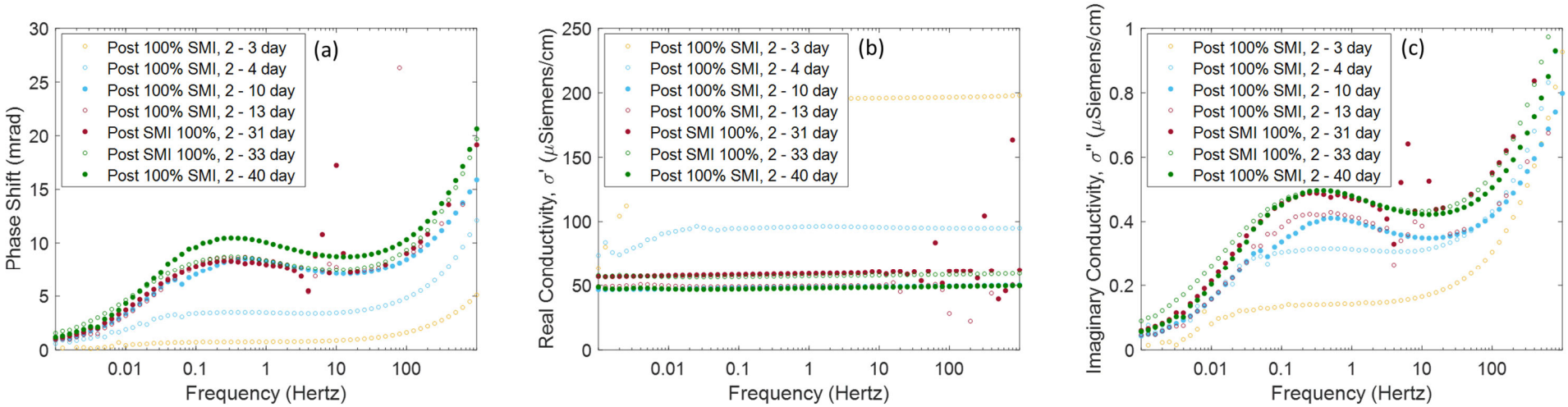

Figure 3.49. Second Hanford sediment layer after 100 wt.% of SMI layer saturated with AGW in a 24-in. length by 0.5-in. ID column as measured over 55 days with constant flow at 0.025 mL/min prior to injection of polyphosphate solutions, with (a) phase shift in mrad, (b) real conductivity, (c) imaginary conductivity in µS/cm, where *circles* represent the measurement for each frequency.

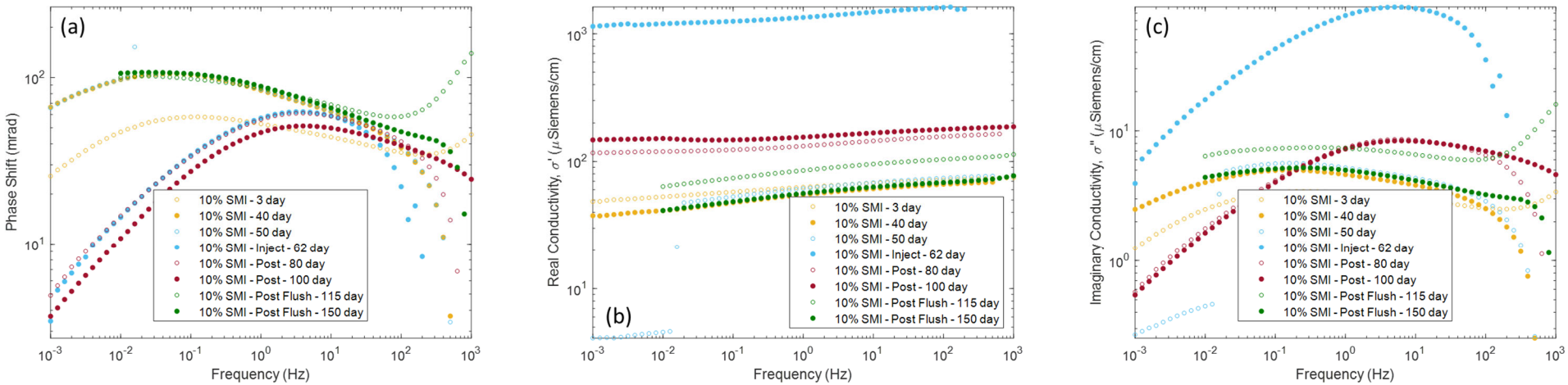

Figure 3.50. Layer of Hanford formation sediments with 10 wt.% of SMI saturated with AGW in a 24-in. length by 0.5-in. ID column as measured over 150 days with constant flow at 0.025 mL/min before and after injection of polyphosphate solutions, with (a) phase shift in mrad, (b) real conductivity, (c) imaginary conductivity in µS/cm, where *circles* represent the measurement for each frequency.

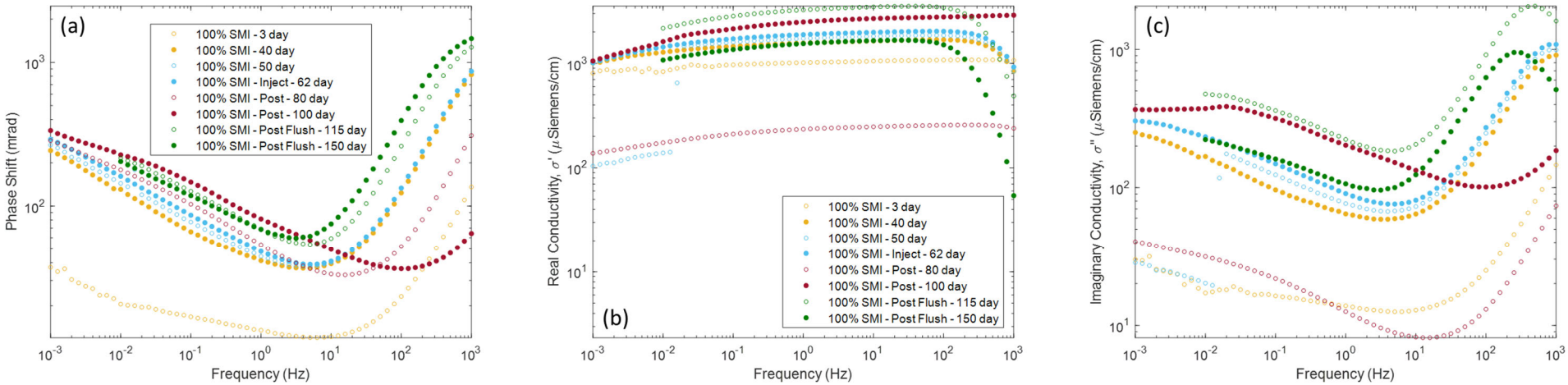

Figure 3.51. Layer of Hanford formation sediments with 100 wt.% of SMI saturated with AGW in a 24-in. length by 0.5-in. ID column as measured over 150 days with constant flow at 0.025 mL/min before and after injection of polyphosphate solutions, with (a) phase shift in mrad, (b) real conductivity, (c) imaginary conductivity in µS/cm, where *circles* represent the measurement for each frequency.

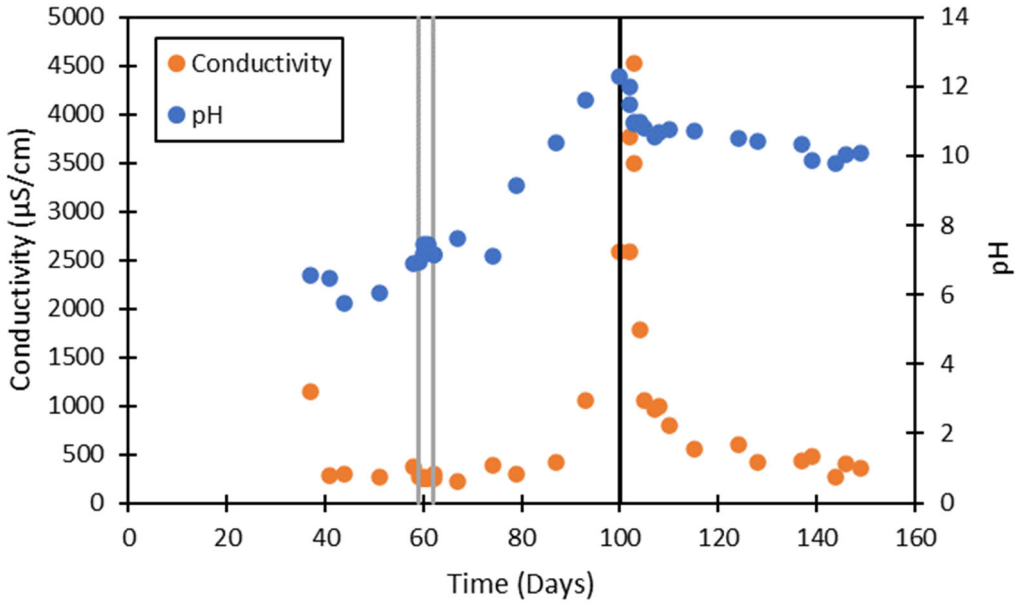

Figure 3.52. Effluent monitoring of solution conductivity (µS/cm) and pH over time following collection in anaerobic bottles where AGW was continuously injected for 58 days, followed by injection of polyphosphate solutions (59-62 days, in between *gray* lines), then no flow from 67 to 100 days followed by flushing with AGW beginning at 102 days (*black* line).

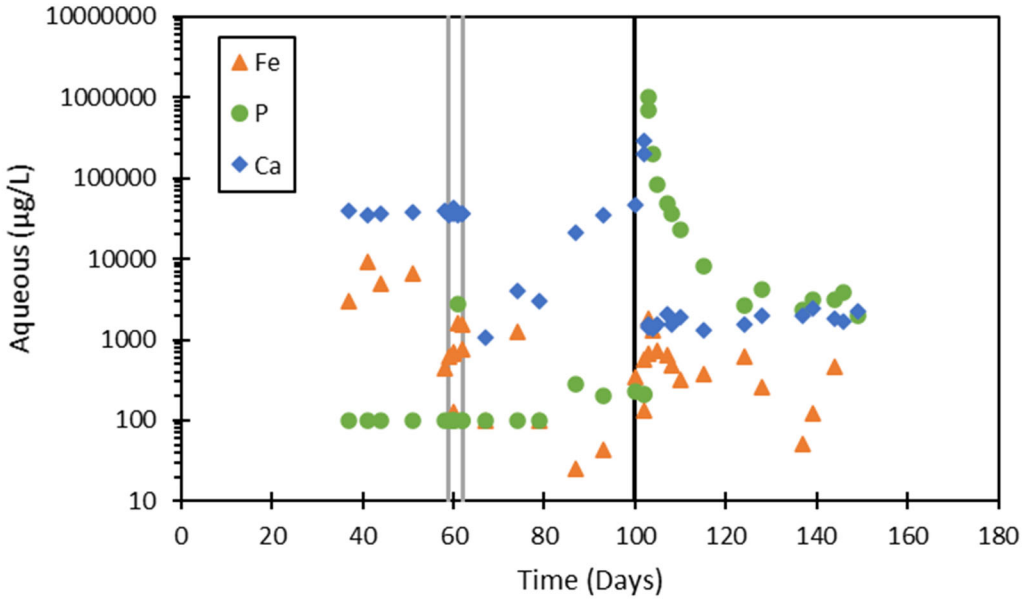

Figure 3.53. Effluent monitoring of elements of interest in solution conductivity (µg/L) over time following collection in anaerobic bottles where AGW was continuously injected for 58 days, followed by injection of polyphosphate solutions (59-62 days, in between *gray* lines), then no flow from 67 to 100 days followed by flushing with AGW beginning at 102 days (*black* line).

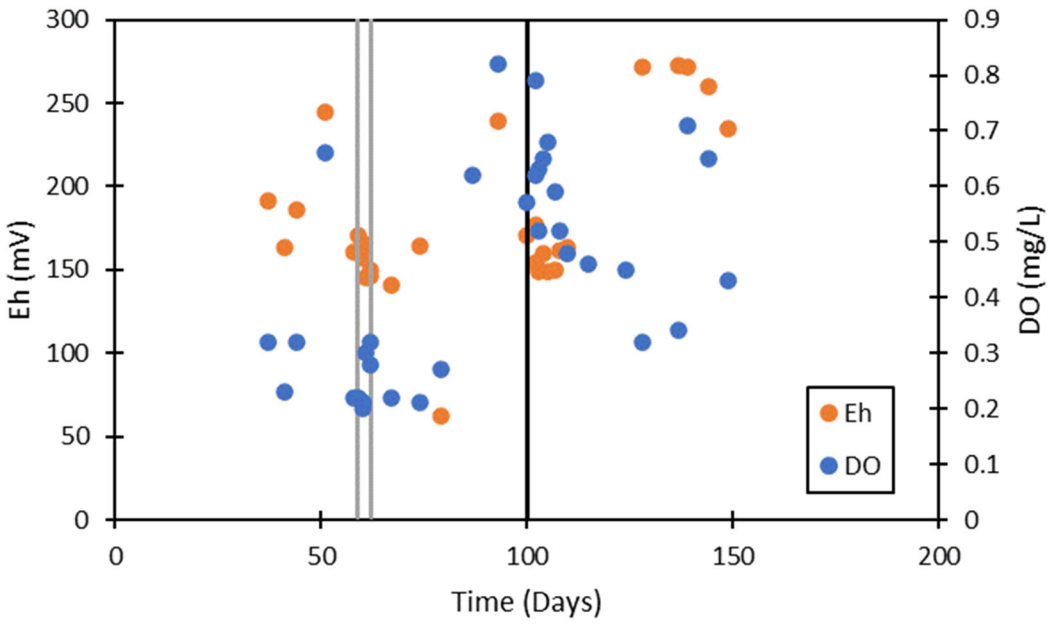

Figure 3.54. Effluent monitoring of redox conditions over time following collection in anaerobic bottles where AGW was continuously injected for 58 days, followed by injection of polyphosphate solutions (59-62 days, in between *gray* lines), then no flow from 67 to 100 days followed by flushing with AGW beginning at 102 days (*black* line).

Table 3.10. Summary of destructive characterization of SMI and apatite column after 150 days.

Column Layer	Moisture Content (dry wt.%)	BET Surface Area (m^2/g)
1 – No SMI	25	5.34 ± .03
2 – 0.1 wt.% SMI	25	NM
3 – No SMI	24	NM
4 – 1.0 wt.% SMI	26	5.55 ± 0.04
5 – No SMI	27	NM
6 – 10 wt.% SMI	27	5.96 ± 0.07
7 – No SMI	25	5.45 ± 0.03
8 – 100 wt.% SMI	11	7.82 ± 0.02
9 – No SMI	26	3.18 ± 0.13
10 – No SMI	23	5.79 ± 0.04

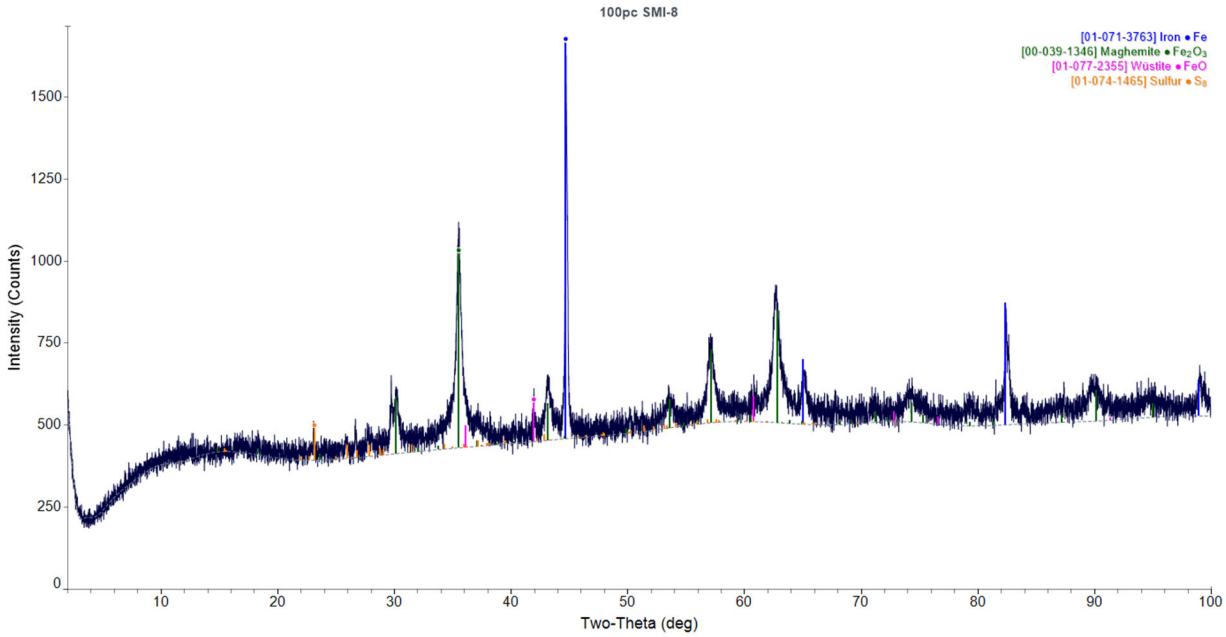

Figure 3.55. XRD for 100 wt.% SMI layer after continuous injection of AGW for 58 days, followed by injection of polyphosphate solutions (59-62 days), then no flow from 67 to 100 days followed by flushing with AGW from 102 to 150 days.

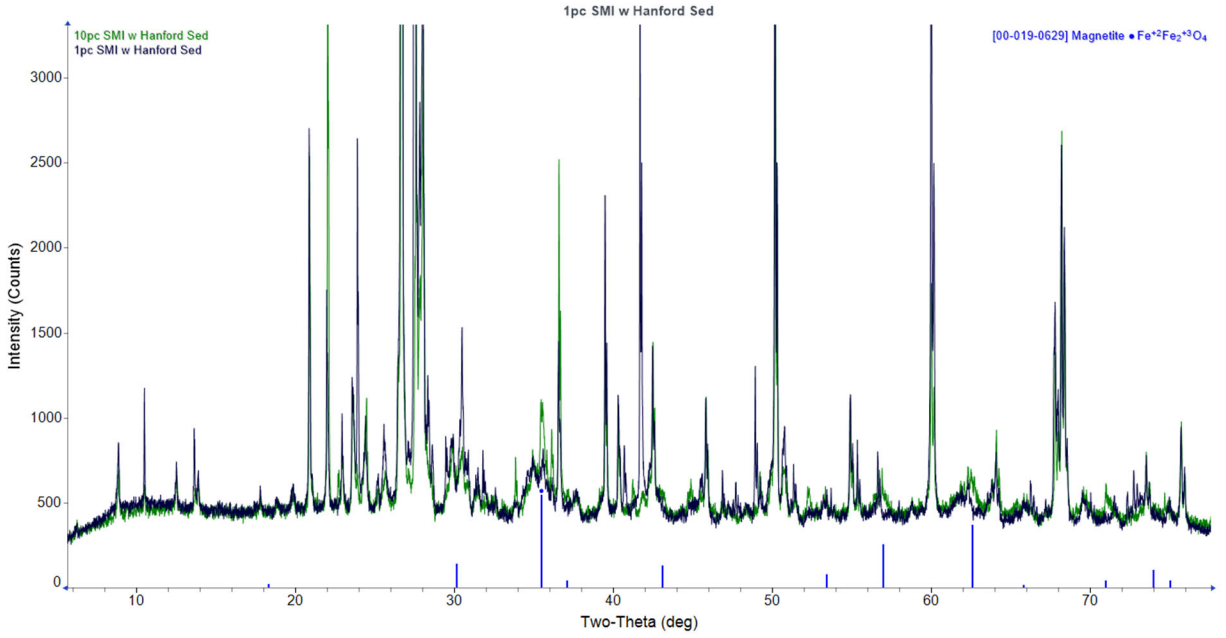

Figure 3.56. XRD for 10 and 1 wt.% SMI layers after continuous injection of AGW for 58 days, followed by injection of polyphosphate solutions (59-62 days), then no flow from 67 to 100 days followed by flushing with AGW from 102 to 150 days.

4.0 Discussion and Conclusions

The purpose of this scoping study was to evaluate if minimally invasive SIP could be used to monitor (a) amendment delivery and (b) precipitation and reactivity of the intended amendment in fully saturated laboratory columns. The primary focus was to assess the frequency-specific phase shift and imaginary conductivity associated with the mineral surfaces targeted by amendments to monitor processes impacting amendment delivery and reactivity. The SIP response to the remediation amendment will change with time after the injection of a precipitate-forming solution (e.g., calcite or apatite forming solutions). In addition, iron-bearing compounds ZVI and SMI are not immediately redox reactive upon injection into porous media but can take days to weeks to form a rind of redox-reactive ferrous phases on the iron surface which impacts the efficacy of the amendment to treat a contaminant.

The amendment technologies tested in this report are currently under consideration for remediation of the Hanford Site's Central Plateau based on a previous review of available technologies for deep vadose zone remediation (DOE/RL 2019). This includes technologies for reduction (e.g., ZVI and SMI) as well as sequestration by sorption, co-precipitation, and coating (e.g., calcite, apatite, and bismuth). The amendments could be delivered as particles in carrier solutions (e.g., ZVI, SMI, and bismuth) or in solutions that form the intended precipitates over time (e.g., calcite and apatite). Remediation may also include delivery of multiple amendments in multiple phases (e.g., ZVI delivery followed by calcite-forming solution injection). As the first phase of evaluation of SIP response for these amendments, they were tested under simplified conditions (i.e., fully saturated with mixing with sediments at variable weight percent). Then, select technologies were investigated in laboratory-scale *in situ* experiments, including injection of biotic apatite forming solutions and ZVI delivery in xanthan gum as well as co-precipitation of calcite or apatite in the presence of Hanford formation sediments and ZVI or SMI. The following amendments were added to fully saturated columns packed with sand or Hanford formation sediments: (a) high-conductivity materials with significant capacitance (ZVI, SMI) or (b) low-conductivity materials with a small capacitance (calcite, apatite, bismuth).

The SIP phase shift or imaginary conductivity change for the high-conductivity amendments was more than 10 times that of the low-conductivity amendments (Table 4.1) suggesting that they could be relatively easily monitored. Moreover, ZVI and SMI were detected at different frequencies (ZVI at > 100 Hz and SMI from 0.01 to 10 Hz). Additional changes in ZVI and SMI were observed with time potentially allowing for monitoring of changes in amendment reactivity that may impact treatment efficacy. The injection of ZVI in sand was shown to alter phase and imaginary conductivity in > 100 Hz (upon initial injection) over time as the ZVI hydrolyzes in water. In addition, ferrous iron phases were created (e.g., adsorbed ferrous iron and green rust) and observed at lower frequencies based on small shifts observed over 43 days. In addition, signal shifts were unlikely to be due to carrier solutions (e.g., xanthan gum) coating sand particles in the *in situ* particle delivery column (Section 3.3.1.2). After injection of SMI, SIP signals increased over time and shifted to lower frequencies (Table 3.7). These changes over time may be due to the ZVI or SMI creating a reducing environment, which may result in the reduction of structural iron in clays over time and formation of secondary products from ZVI and SMI. Magnetite was the major phase identified post SMI experiments via XRD (Figure 3.56). However, previous work has suggested that adsorbed ferrous iron may be present and increases the phase shift and imaginary conductivity in the 0.1 to 10 Hz range (Orozco et al. 2011; Szecsody et al. 2020a; Williams et al. 2009), although the imaginary conductivity change for structural ferrous iron in clays has been observed from 0.001 to 0.1 Hz (Slater and Lesmes 2002; Szecsody et al. 2020a).

The low-conductivity amendments (calcite, abiotic and biotic apatite, bismuth subnitrate) exhibited small phase and imaginary conductivity changes with amendment addition that may allow for monitoring of

their *in situ* delivery and formation. The changes were above minimum detection limits (0.5 mrad for phase shift, 0.03 µS/cm for imaginary conductivity) for the highest concentration except for the commercial bismuth material, although the ability to detect these amendments will likely be sediment specific. In addition, phase shifts were detected at specific frequencies which may allow for differentiation between amendments (Table 4.1). Note that these amendments were also detectable due to their ability to decrease the phase shift and imaginary conductivity as observed in some conditions for *in situ* formation of calcite and apatite amendments in Hanford sediments with and without SMI or ZVI. Therefore, possible combinations of amendments including a reductant (i.e., ZVI, SMI) and a low-conductivity precipitate that would coat a reduced/precipitated contaminant (i.e., apatite or calcite) could likely be monitored with SIP.

This work measured SIP signals for apatite and bismuth materials for the first time and extends previous work with ZVI, SMI, and calcite to Hanford Site relevant conditions while considering aging and oxidation processes at the laboratory scale. However, these experiments were conducted under fully saturated conditions, so additional work is necessary to understand the utility of this technique in the vadose zone at the Hanford Site for the next phase of experiments. These experiments highlight that SIP could improve our ability to quantify formation of certain precipitates targeted by remediation activities as compared to ER methods. Therefore, SIP may be a valuable tool for monitoring and characterization during active remediation for a variety of technologies. In addition, the simultaneous collection of both ER and SIP should be considered in the future for optimization of monitoring in the field. There is potential for collection of ER and SIP data as part of a comprehensive monitoring plan (e.g., SIP for monitoring of secondary reactions at sediment surfaces in source zones and ER for surveying of larger, surrounding areas). Therefore, future experiments will focus on the following: (1) obtaining SIP signals for Hanford sediments; (2) performing SIP monitoring under unsaturated conditions, utilizing electrodes optimized for this purpose; and (3) scaling up the size of experiments (e.g., meter-scale 2-D flow systems) to identify additional sensitivities associated with electrode configurations.

Table 4.1. Summary of SIP sensitivity to amendments added to sediments.

Amendment	Matrix	Phase Shift (mrad)	Imaginary Conductivity (µS/cm)	Frequency Range (Hz)
10 wt.% ZVI	Sand	150[(a)]	19.3[(a)]	> 100
	Hanford fm	87[a]	7.4[(a)]	> 100
10 wt.% SMI	Sand	64	44	0.1 - 10
	Hanford fm	36	27	0.01 - 10
10 wt.% abiotic apatite	Sand	10	0.5	< 10
	Hanford fm	10	2.0	< 10
3 wt.% biotic apatite	Sand	1.1	0.5	< 1
	Hanford fm	10	4	< 1
10 wt.% calcite	Sand	2	0.3	< 0.1
	Hanford fm	10.5	3.0	< 1.0
10 wt.% bismuth	Sand	0.7	0.06	< 1.0[(b)]
	Hanford fm	2	1.5	<10[(b)]
No amendment	Sand	0.05-1.0	0.002-0.05	0.001-100
	Hanford fm	1.5-10	1.0-4.5	0.001-100

(a) Value at 100 Hz to estimate high frequency ZVI signal.
(b) Broad signal across frequency, no clear maxima.

5.0 Quality Assurance

This work was performed in accordance with the Pacific Northwest National Laboratory Nuclear Quality Assurance Program (NQAP). The NQAP complies with the DOE Order 414.1D, *Quality Assurance*. The NQAP uses NQA-1-2012, *Quality Assurance Requirements for Nuclear Facility Application,* as its consensus standard and NQA-1-2012 Subpart 4.2.1 as the basis for its graded approach to quality.

This work emphasized acquiring new theoretical or experimental knowledge. The information associated with this report should not be used as design input or operating parameters without additional qualification.

6.0 References

Abdel Aal G, E Atekwana, S Radzikowski, and S Rossbach. 2009. "Effect of bacterial adsorption on low frequency electrical properties of clean quartz sands and iron-oxide coated sands." *Geophysical Research Letters* 36.

Abdel Aal GZ, EA Atekwana, and A Revil. 2014. "Geophysical signatures of disseminated iron minerals: A proxy for understanding subsurface biophysicochemical processes." *Journal of Geophysical Research: Biogeosciences* 119:1831-1849.

Abdel Aal GZ, EA Atekwana, LD Slater, and EA Atekwana. 2004. "Effects of microbial processes on electrolytic and interfacial electrical properties of unconsolidated sediments." *Geophysical Research Letters* 31.

Archie GE. 1942. "The electrical resistivity log as an aid in determining some reservoir characteristics." *Transactions of the AIME* 146:54-62.

Atekwana EA, WA Sauck, GZ Abdel Aal, and DD Werkema Jr. 2002. "Geophysical investigation of vadose zone conductivity anomalies at a hydrocarbon contaminated site: implications for the assessment of intrinsic bioremediation." *Journal of Environmental and Engineering Geophysics* 7:103-110.

Atekwana EA and LD Slater. 2009. "Biogeophysics: A new frontier in Earth science research." *Reviews of Geophysics* 47.

Binley A and L Slater. 2020. *Resistivity and Induced Polarization: Theory and Applications to the Near-surface Earth*. Cambridge University Press.

Bücker M, AF Orozco, and A Kemna. 2018. "Electrochemical polarization around metallic particles—Part 1: The role of diffuse-layer and volume-diffusion relaxation." *Geophysics* 83(4):E203-E217.

Bücker M, S Undorf, A Flores Orozco, and A Kemna. 2019. "Electrochemical polarization around metallic particles—Part 2: The role of diffuse surface charge." *Geophysics* 84(2): E57-E73.

Chang F-R C and G Sposito. 1994. "The electrical double layer of a disk-shaped clay mineral particle: Effect of particle size." *Journal of Colloid Interface Science* 163: 19-27.

Chuprinko D and K Titov. 2017. "Influence of mineral composition on spectral induced polarization in sediments." *Geophysical Journal International* 209(1):186-191. https://doi.org/10.1093/gji/ggx018

Cordova EA, VA Garayburu-Caruso, CI Pearce, KJ Cantrell, J Morad, E Gillispie, BJ Riley, F Cintron-Colon, TG Levitskaia, and SA Saslow. 2020. "Hybrid Sorbents for ^{129}I Capture from Contaminated Groundwater." *ACS Applied Materials & Interfaces 12(23):26113-26126*.

Davis CA, E Atekwana, E Atekwana, LD Slater, S Rossbach, and MR Mormile. 2006. "Microbial growth and biofilm formation in geologic media is detected with complex conductivity measurements." *Geophysical Research Letters* 33.

DOE/RL. 2019. *Technology Evaluation and Treatability Studies Assessment for the Hanford Central Plateau Deep Vadose Zone* (*draft*). DOE/RL-2017-58. Department of Energy, Richland, WA.

Doetsch J, T Ingeman-Nielsen, AV Christiansen, G Fiandaca, E Auken, and B Elberling. 2015. "Direct current (DC) resistivity and induced polarization (IP) monitoring of active layer dynamics at high temporal resolution." *Cold Regions Science and Technology* 119:16-28.

Fiandaca G, J Raman, A Binley, A Gazoty, AV Christiansen, and E Auken. 2013. "Resolving spectral information from time domain induced polarization data through 2-D inversion." *Geophysical Journal International* 192: 631-646.

Garcia A. 2018. "The effect of microbial growth on the spectral induced polarization response in Hanford vadose zone sediment in the presence of autunite mineral." Thesis for Master of Science in Geoscience, Florida International University, Miami, FL, p. 108.

Hao N, SM Moysey, BA Powell, and D Ntarlagiannis. 2015. "Evaluation of surface sorption processes using spectral induced polarization and a ^{22}Na tracer." *Environmental Science and Technology* 49:9866-9873.

Huisman JA, E Zimmermann, O Esser, F-H Haegel, A Treichel, and H Vereecken. 2016. "Evaluation of a novel correction procedure to remove electrode impedance effects from broadband SIP measurements." *Journal of Applied Geophysics* 135:466-473.

Johnson TC, M Oostrom, MJ Truex, JN Thomle, and TW Wiets. 2013. "Determination of Water Saturation Using Gas Phase Partitioning Tracers and Time-Lapse Electrical Conductivity Measurements." *Vadose Zone Journal* 12.

Johnson T, R Versteeg, F Day-Lewis, W Major, and J Lane Jr. 2014. "Time-Lapse Electrical Geophysical Monitoring of Amendment-Based Biostimulation." *Groundwater* 53(6):920-032.

Joseph S. 2016. "The Application of Spectral Induced Polarization to Determination of Hydraulic Conductivity." Doctoral Thesis, Victoria University of Wellington, Kelburn, Wellington, New Zealand.

Joyce, RA, DR Glaser, DD Werkema, and EA Atekwana. 2012. "Spectral induced polarization response to nanoparticles in a saturated sand matrix." *Journal of Applied Geophysics*, 77:63-71.

Kemna A, A Binley, G Cassiani, E Niederleithinger, A Revil, L Slater, KH Williams, AF Orozco, F-H Haegel, and A Hoerdt. 2012. "An overview of the spectral induced polarization method for near-surface applications." *Near Surface Geophysics* 10:453-468.

Lawter AR, WL Garcia, RK Kukkadapu, O Qafoku, ME Bowden, SA Saslow, and NP Qafoku. 2018. "Technetium and iodine aqueous species immobilization and transformations in the presence of strong reductants and calcite-forming solutions: Remedial action implications." *Science of the Total Environment* 636:588-595.

Lesmes DP and KM Frye. 2001. "Influence of pore fluid chemistry on the complex conductivity and induced polarization responses of Berea sandstone." *Journal of Geophysical Research: Solid Earth* 106: 4079-4090.

Lesmes DP and FD Morgan. 2001. "Dielectric spectroscopy of sedimentary rocks." *Journal of Geophysical Research: Solid Earth* 106:13329-13346.

Marshall DJ and TR Madden. 1959. "Induced polarization, a study of its causes." *Geophysics* 24(4):790-816.

Mellage A, AB Holmes, S Linley, L Vallée, F Rezanezhad, N Thomson, F Gu, and P Van Cappellen. 2018. "Sensing coated iron-oxide nanoparticles with spectral induced polarization (SIP): experiments in natural sand packed flow-through columns." *Environmental Science and Technology* 52:14256-14265.

Moore, R, J Szecsody, M Truex, K Kelean, R Bontchev, C Ainsworth. 2007. "Formation of nano-size apatite crystals in sediments for contaminant and stabilization of contaminants." *Environmental Applications of Nanomaterials, Synthesis, Sorbents, and Sensors* (eds) G. Fryxell and G. Cao. Imperial College Press 89-109.

Muller KA, L Zhong, CE Bagwell. 2021a. "Characterizing the influence of organic polymers on the specific reactivity of particulate remedial amendments." *Frontiers in Environmental Science*. Under Review.

Muller, KA, JM Torgeson, L Zhong, and CE Bagwell. 2021b. "Environmental fate and transport of polymers for subsurface remedial applications." *Polymers and the Environment.* In prep.

Mwakanyamale K, L Slater, A Binley, and D Ntarlagiannis. 2012. "Lithologic imaging using complex conductivity: Lessons learned from the Hanford 300 Area." *Geophysics* 77:E397-E409.

Ntarlagiannis D, J Robinson, P Soupios, and L Slater. 2016. "Field-scale electrical geophysics over an olive oil mill waste deposition site: Evaluating the information content of resistivity versus induced polarization (IP) images for delineating the spatial extent of organic contamination." *Journal of Applied Geophysics* 135:418-426.

Ntarlagiannis D, N Yee, and L Slater. 2005. "On the low-frequency electrical polarization of bacterial cells in sands." *Geophysical Research Letters* 32.

Orozco AF, A Kemna, C Oberdörster, L Zschornack, C Leven, P Dietrich, and H Weiss. 2012. "Delineation of subsurface hydrocarbon contamination at a former hydrogenation plant using spectral induced polarization imaging." *Journal of Contaminant Hydrology* 136:131-144.

Orozco AF, M Velimirovic, T Tosco, A Kemna, H Sapion, N Klaas, R Sethi, and L Bastiaens. 2015. "Monitoring the injection of microscale zerovalent iron particles for groundwater remediation by means of complex electrical conductivity imaging." *Environmental Science & Technology* 49:5593-5600.

Orozco AF, KH Williams, PE Long, SS Hubbard, and A Kemna. 2011. "Using complex resistivity imaging to infer biogeochemical processes associated with bioremediation of a uranium-contaminated aquifer." *Journal of Geophysical Research: Biogeosciences* 116.

Personna, YR, D Ntarlagiannis, L Slater, N Yee, M O'Brien, and S Hubbard. 2008. "Spectral induced polarization and electrodic potential monitoring of microbially mediated iron sulfide transformations." *Journal of Geophysical Research: Biogeosciences* 113(G2).

Placencia-Gómez, E, LD Slater, D Ntarlagiannis, and A Binley. 2013. "Laboratory SIP signatures associated with oxidation of disseminated metal sulfides." *Journal of Contaminant Hydrology* 148:25-38.

Placencia-Gómez E, A Parviainen, L Slater, and J Leveinen. 2015. "Spectral induced polarization (SIP) response of mine tailings." *Journal of Contaminant Hydrology* 173:8-24.

Placencia-Gómez E and LD Slater. 2016. "On the pore water chemistry effect on spectral induced polarization measurements of pyrite." *Journal of Applied Geophysics* 135:474-485.

Prodan C, F Mayo, JR Claycomb, JH Miller, and MJ Benedik. 2004. “Low-frequency, low-field dielectric spectroscopy of living cell suspensions.” *Journal of Applied Physics* 95:3754-3756.Revil A, E Atekwana, C Zhang, A Jardani, and S Smith. 2012. “A new model for the spectral induced polarization signature of bacterial growth in porous media.” *Water Resources Research* 48.

Revil A and P Glover. 1998. “Nature of surface electrical conductivity in natural sands, sandstones, and clays.” *Geophysical Research Letters* 25:691-694.

Revil, A, E Atekwana, C Zhang, A Jardani, and S Smith, S. 2012. “A new model for the spectral induced polarization signature of bacterial growth in porous media.” *Water Resources Research*, 48(9).

Saneiyan S, D Ntarlagiannis, J Ohan, J Lee, F Colwell, and S Burns. 2019. “Induced polarization as a monitoring tool for in-situ microbial induced carbonate precipitation (MICP) processes. *Ecological Engineering* 127:36-47.

Saneiyan S, D Ntarlagiannis, DD Werkema, Jr, and A Ustra. 2018. “Geophysical methods for monitoring soil stabilization processes.” *Journal of Applied Geophysics* 148:234-244.

Schön J. 2011. Electrical Properties. *Handbook of Petroleum Exploration and Production*. Elsevier. 8: 273-336.

Seidel K and G Lange. 2007. “Direct current resistivity methods.” *Environmental Geology*. Springer, pp. 205-237.

Shi Z, D Fan, RL Johnson, PG Tratnyek, JT Nurmi, Y Wu, and KH Williams. 2015. “Methods for characterizing the fate and effects of nano zerovalent iron during groundwater remediation.” *Journal of Contaminant Hydrology* 181:17-35.

Slater LD and D Lesmes. 2002. “IP interpretation in environmental investigations.” *Geophysics* 67:77-88.

Slater, LD, J Choi, and Y Wu. 2005. “Electrical properties of iron-sand columns: Implications for induced polarization investigation and performance monitoring of iron-wall barriers.” *Geophysics*, 70(4):G87-G94.

Sogade JA, F Scira-Scappuzzo, Y Vichabian, W Shi, W Rodi, DP Lesmes, and FD Morgan. 2006. “Induced-polarization detection and mapping of contaminant plumes.” *Geophysics* 71:B75-B84.

Sumner ME. 2000. *Soil Chemistry*. CRC Press. Boca Raton, FL.

Szecsody JE, ML Rockhold, M Oostrom, RM Moore, C Burns, MA Williams, L Zhong, JS Fruchter, J McKinley, J Vermeul, M Covert, TW Wietsma, AT Breshears, and B Garcia. 2009. *Sequestration of Sr-90 Subsurface Contamination in the Hanford 100-N Area by Surface Infiltration of a Ca-citrate-phosphate Solution*. PNNL-18303, Pacific Northwest National Laboratory, Richland, WA.

Szecsody JE, RM Moore, M Rigali, VR Vermelu, and J Luellen. 2016. *Use of Ca-citrate-phosphate solution to form hydroxyapatite for uranium stabilization of Old Rifle sediments: Laboratory proof of principle studies*. PNNL-25303. Pacific Northwest National Laboratory, Richland, WA.

Szecsody JE, PG Tratnyek, TC Johnson, HP Emerson, JL Robinson, E Placencia-Gómez, M Bradley, TN Thomle, MJ Truex, CT Resch, and BN Gartman. 2020a. *Characterization of Enhanced Subsurface Abiotic Reactivity with Electrical Resistivity Tomography/Induced Polarization.* SERDP Project ER-2619

Final Report, Strategic Environmental Research and Development Program (SERDP), Arlington, VA. https://www.serdp-estcp.org/.

Szecsody JE, HP Emerson, RD Mackley, CT Resch, BN Gartman, CI Pearce, SA Saslow, O Qafoku, KA Rod, and MK Nims. 2020b. *Evaluation of the change in uranium mobility in sediments from the Hanford 300-FF-5 Stage B Polyphosphate Field Injection*. PNNL-29650. Pacific Northwest National Laboratory, Richland, WA.

Truex MJ, GB Chronister, CE Strickland, CD Johnson, GD Tartakovsky, M Oostrom, RE Clayton, TC Johnson, VL Freedman, and ML Rockhold. 2018. *Deep Vadose Zone Treatability Test of Soil Desiccation for the Hanford Central Plateau*. PNNL-26902, Pacific Northwest National Laboratory, Richland, WA.

Truex MJ, VR Vermeul, DP Mendoza, BG Fritz, RD Mackley, M Oostrom, TW Wietsma, and TW Macbeth. 2011. "Injection of zero valent iron into an unconfined aquifer using shear-thinning fluids." *Groundwater Monitoring and Remediation* 31:50-58.

Turick CE, S Shimpalee, P Satjaritanun, J Weidner, and S Greenway. 2019. "Convenient non-invasive electrochemical techniques to monitor microbial processes: current state and perspectives." *Applied Microbiology and Biotechnology* 103:8327-8338.

Vermeul VR, JE Szecsody, BG Fritz, MD Williams, RC Moore, and JS Fruchter. 2014. "An injectable apatite permeable reactive barrier for in situ ^{90}Sr immobilization." *Groundwater Monitoring and Remediation* 34:28-41.

Vieira LB, CA Moreira, AR Côrtes, and GL Luvizotto. 2016. "Geophysical modeling of the manganese deposit for Induced Polarization method in Itapira (Brazil)." *Geofísica Internacional* 55:107-117.

Vinegar H and M Waxman. 1984. "Induced polarization of shaly sands." *Geophysics* 49:1267-1287.

Wang C and LD Slater. 2019. "Extending accurate spectral induced polarization measurements into the kHz range: modelling and removal of errors from interactions between the parasitic capacitive coupling and the sample holder." *Geophysical Journal International* 218:895-912.

Weller A, L Slater, A Binley, S Nordsiek, and S Xu. 2015. "Permeability prediction based on induced polarization: Insights from measurements on sandstone and unconsolidated samples spanning a wide permeability range." *Geophysics* 80:D161-D173.

Weller A, L Slater, and S Nordsiek. 2013. "On the relationship between induced polarization and surface conductivity: Implications for petrophysical interpretation of electrical measurements." *Geophysics* 78:D315-D325.

Williams KH, A Kemna, MJ Wilkins, J Druhan, E Arntzen, AL N'Guessan, PE Long, SS Hubbard, and JF Banfield. 2009. "Geophysical monitoring of coupled microbial and geochemical processes during stimulated subsurface bioremediation." *Environmental Science and Technology* 43:6717-6723.

Wu Y, S Hubbard, KH Williams, and J Ajo-Franklin. 2010. "On the complex conductivity signatures of calcite precipitation." *Journal of Geophysical Research: Biogeosciences* 115.

Wu Y, R Versteeg, L Slater, and D LaBrecque. 2009. "Calcite precipitation dominates the electrical signatures of zero valent iron columns under simulated field conditions." *Journal of Contaminant Hydrology* 106:131-143.

Wu, Y, L Slater, R Versteeg, and D LaBrecque. 2008. "A comparison of the low frequency electrical signatures of iron oxide versus calcite precipitation in granular zero valent iron columns." *Journal of Contaminant Hydrology* 95(3-4):154-167.

Wu, Y, LD Slater, and N Korte. 2005. "Effect of precipitation on low frequency electrical properties of zerovalent iron columns." *Environmental Science and Technology* 39(23):9197-9204.

Zhang C, A Revil, Y Fujita, J Munakata-Marr, and G Redden. 2014. "Quadrature conductivity: A quantitative indicator of bacterial abundance in porous media." *Geophysics* 79:D363-D375.

Zhang C, L Slater, and C Prodan. 2013. "Complex Dielectric Properties of Sulfate-Reducing Bacteria Suspensions." *Geomicrobiology Journal* 30:490-496.

Zhong L, M Oostrom, MJ Truex, VR Vermeul, and JE Szecsody. 2013. "Rheological behavior of xanthan gum solution related to shear thinning fluid delivery for subsurface remediation." *Journal of Hazardous Materials* 244-245:160-170.

Zhou F, Q Liu, X Liu, W Li, J Feng, and R-A Chi. 2020. "Surface electrical behaviors of apatite, dolomite, quartz, and phosphate ore." *Frontiers in Materials* 7:35.

Zimmermann E, J Huisman, B Wolters, and S van Waasen. 2012. "Optimal electrode design for improved phase accuracy of spectral EIT images." Proceedings of the 6th International Symposium on Process Tomography, Cape Town, South Africa 26, 2012-2028.2003.

Zimmermann E, A Kemna, J Berwix, W Glaas, H Münch, and J Huisman. 2008a. "A high-accuracy impedance spectrometer for measuring sediments with low polarizability." *Measurement Science and Technology* 19:105603.

Zimmermann E, A Kemna, J Berwix, W Glaas, and H Vereecken. 2008b. "EIT measurement system with high phase accuracy for the imaging of spectral induced polarization properties of soils and sediments." *Measurement Science and Technology* 19:094010.

Appendix A – Amendment Synthesis and Characterization

A.1 Synthesis of Mineral Phases

A.1.1 Batch Calcite Synthesis Method

Calcite was synthesized based on previous research (Saslow et al. 2019; Lawter et al. 2018; Qafoku et al. 2018; Wellman et al. 2008). Briefly, equal parts of 0.1 M $CaCl_2$ (Sigma Aldrich) and 0.1 M $(NH_4)_2CO_3$ (Sigma Aldrich) were mixed slowly and allowed to settle overnight. Solids were separated by centrifugation at approximately 4000 rpm for 10 minutes without washing. Approximately 17.7 grams of calcite was recovered from 2 liters of solution .

A.1.2 Batch Co-precipitation of Calcite with ZVI or SMI and Hanford Formation Sediments

Batch experiments were conducted to produce homogenous calcite precipitation with Hanford formation sediment to test the change in spectral induced polarization (SIP) signal compared to the control sediment (without freshly precipitated calcite). Additional SIP experiments tested calcite, but the precipitated calcite was mixed into the sediment and therefore sediment mineral coatings were not produced. In addition, a set of batch experiments with zero valent iron (ZVI) or sulfur modified iron (SMI) mixed into the sediment were included to compare relatively conductive (ZVI/SMI) and non-conductive (calcite) materials. ZVI/SMI produces a greater SIP signal, and calcite may cover the surfaces of ZVI/SMI during precipitation, dampening the signal leading to unique SIP signal changes that may indicate calcite precipitation.

For each batch test, 25 g of Hanford formation sediment (< 2 mm) was added to a batch reactor. For tests with ZVI or SMI, 0.25 g of ZVI (Hepure) or SMI was added and mixed with the sediment. Calcite forming solutions (1 M $CaCl_2$ and 1 M $(NH_4)_2CO_3$) were prepared in Hanford artificial groundwater (AGW). Forty milliliters of 1 M $CaCl_2$ in Hanford AGW (measured via graduated cylinder) was added to each reactor and gently swirled. Next, 40 mL of 1 M $(NH_4)_2CO_3$ in Hanford AGW (measured via graduated cylinder) was added to each reactor slowly and then swirled. The caps were left loose for several minutes to allow gas to escape. The reactors were then placed on a shaker at 100 rpm overnight. The following day, the contents of the reactors were filtered (0.45 µm Millipore). For each set of batch experiments containing calcite (calcite + sediment; and calcite + sediment + ZVI/SMI), duplicate reactors were prepared for SIP column packing and moisture content determination and two reactors were air-dried over several days to determine calcite content. Two sets of control experiments were also prepared, using sediment only or sediment + ZVI/SMI. For these experiments, 80 mL of Hanford AGW was added to each reactor in lieu of calcite forming solutions.

A.1.3 Column Co-precipitation of Calcite with SMI and Hanford Formation Sediments

After 69 days of continuous flow of AGW at 0.025 mL/min through the 24-in. length by 0.5-in. ID column packed with layers of sediment and variable SMI wt.% as described in Figure 3.37, calcite forming solutions were injected via mixing of $CaCl_2$ and $(NH_4)_2CO_3$ at ports along the column body in between the electrode pairs. The column was initially saturated with 0.1 M $CaCl_2$ from the bottom port of the column at a flow rate of 0.025 mL/min for 96 hours (approximately five pore volumes were flushed). Following saturation with the $CaCl_2$, two Kloehn 8-port syringe pumps (Kloehn, NV, USA) were used to inject 0.1 M $(NH_4)_2CO_3$ nearly simultaneously into 12 ports along the body of the column at a flow rate of 0.04 mL/min (in each port, for a total injection of 0.48 mL/min into the column). After 22 hours, the

influent lines were flushed with double deionized water and then $CaCl_2$, and injection switched to $CaCl_2$ for 3 hours (at the 0.04 mL/hr injection rate, in 11 ports – 1 port clogged). Then, continuous flow of AGW through the main influent line was re-initiated at 0.025 mL/min.

A.1.4 Biotically-Precipitated Apatite Synthesis Method

The synthesis of biotic apatite involved mixing a pH 7.5 phosphate solution with Ca-citrate in the presence of microbes from Hanford formation sediment and the Columbia River water such that as citrate biodegrades, the calcium is released from the complex and slowly forms apatite. The 5 liters of solution had a total of 40 mmol/L phosphate, of which 32.4 mmol/L was Na_2HPO_4, 5.6 mmol/L was NaH_2PO_4, and 2.0 mmol/L was NH_4HPO_4. The solution also contained 100 mM Ca-citrate, and the measured pH was 7.57. The mixture of phosphate compounds buffered the pH to 7.5 and supplied a small amount of nitrogen for the microbes. This 5-liter solution was made in unfiltered Columbia River water with addition of 500 g of Hanford formation sediment suspended in the solution in a woven PTFE bag to supply both microbes from the river water (which previous studies have shown biodegrades most of the citrate) and sediment microbes. The slow formation of apatite, which is optimal at pH 7.5, results in a relatively high surface area apatite (94 m^2/g), composed of 100-nm sized rods of apatite conglomerated on surfaces as shown previously (Szecsody et al. 2009, 2016). The 5 liters of solution was placed in a 35°C oven for approximately 30 days to allow apatite formation. The precipitate was then washed with deionized water using a 0.2-micron suction filter to remove most of the high ionic strength solution and dried at 35°C.

For the 24-in. length by 0.5-in. ID 1-D column in which the Ca-citrate/Na-phosphate was injected into to form apatite *in situ*, a Ca-poor solution was used in order to utilize most of the calcium on sediment ion exchange sites. This solution contained 40 mmol/L phosphate, 3.6 mmol/L calcium, and 9.0 mmol/L trisodium citrate at pH 7.5 mixed up in unfiltered Columbia River water. In that column, a total of 5 pore volumes of the solution was injected over 24 hours and then left static for approximately 4 weeks to allow precipitation to occur following microbial degradation of citrate. The column was initially saturated with AGW prior to injection of Ca-citrate/Na-phosphate.

Following experiments, columns were sectioned and water content, phosphorus by extractions, and total organic carbon were measured in the solid phase as described in Section A.2.

A.1.5 Polyphosphate Method for Synthesis of Apatite

Two experiments were conducted where apatite was precipitated *in situ* from polyphosphate solutions in 24-in. length by 0.5-in. ID columns, including (i) Hanford sediment only and (ii) Hanford sediment layers packed with variable concentrations of SMI as described in Figure 3.37. Polyphosphate solution was prepared at approximately half of the concentration used in the 300-FF-5 Stage B injection in 2019 for the column conducted with only Hanford sediment and at the full concentration for the column with variable concentrations of SMI (Szecsody et al. 2020, 2012). Therefore, the targeted concentration was 43.5- or 88-mM total phosphate, respectively, with 90% as orthophosphate through addition of sodium phosphate and 10% as pyrophosphate with the pH initially adjusted to pH 7.5. Approximately three pore volumes were injected at a flow rate of 0.025 mL/min followed by 6 weeks without flow to allow for slow precipitation of hydroxyapatite. The pyrophosphate slowly converts to orthophosphate and precipitates with native calcium initially as monocalcium phosphate, which then crystallizes from di- to octa-calcium phosphate and eventually forms hydroxyapatite (Sumner 2000).

The polyphosphate solutions were diluted from a stock solution prepared from the recipe developed by Two Rivers Chemicals with a 50-mL concentrated solution (965 mM). First, 42.2 mL of water is stirred with 3.35 mL (or 5.006 grams) of H_3PO_4 until dissolved. Then, 2.25 mL (or 3.47 grams) of NaOH is

added to reach a pH of 5.4 followed by 2.2 mL (or 3.2 grams) of KOH to reach a pH of 7.04. Finally, 1.02 grams of sodium pyrophosphate was added, heated, and stirred until dissolved.

A.2 Characterization of Amendments and Porous Media

Brunauer – Emmett – Teller (BET) specific surface area of these materials was measured with an Accelerated Surface Area and Porosity System ASAP 2020 from Micromeritics (Brunauer et al. 1938). The materials were degassed at 80°C for approximately 9 hours with a temperature ramp of 5°C/min. All samples were analyzed in triplicate with nitrogen (N_2) or krypton (Kr) gas. Krypton gas was used for samples with relatively low surface area, e.g., calcite samples.

X-ray diffraction patterns were collected from powders packed into zero-background well holders using a Rigaku SmartLab SE diffractometer. The instrument employed Bragg-Brentano geometry with a Cu X-ray source (λ = 1.5418 Å), a variable divergence slit, and a high-speed D/teX Ultra 250 1D detector. Patterns were collected between 2 and 100 °2θ at intervals of 0.01 °2θ and minerals identified through comparison with reference patterns in the ICDD database (International Center for Diffraction Data, PA).

Estimates of mineral concentrations were obtained by Rietveld fitting using Topas (v6, Bruker AXS). This method calculates the full diffraction profile from published crystal structures, applying convolutions for instrumental and specimen broadening arising from finite crystallite size and/or microstrain. Atomic coordinates were not refined, and instrumental parameters were also fixed after having been established from standard powders. For natural samples, the primary source of uncertainty for these determinations is the degree to which the published crystal structure of complex minerals matches that of the specimen.

A.2.1 X-ray Diffraction Patterns for Amendments

The following figures represent the amendment patterns with reference mineral patterns overlaid.

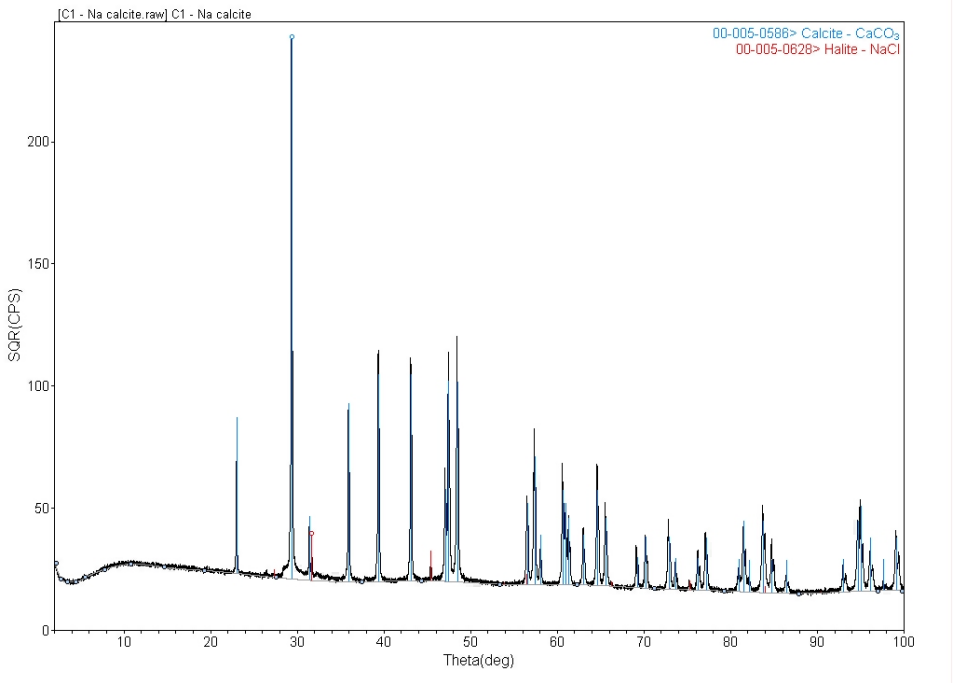

Figure A.1. XRD pattern for calcite synthesized at PNNL with counts on y-axis versus theta on the x-axis.

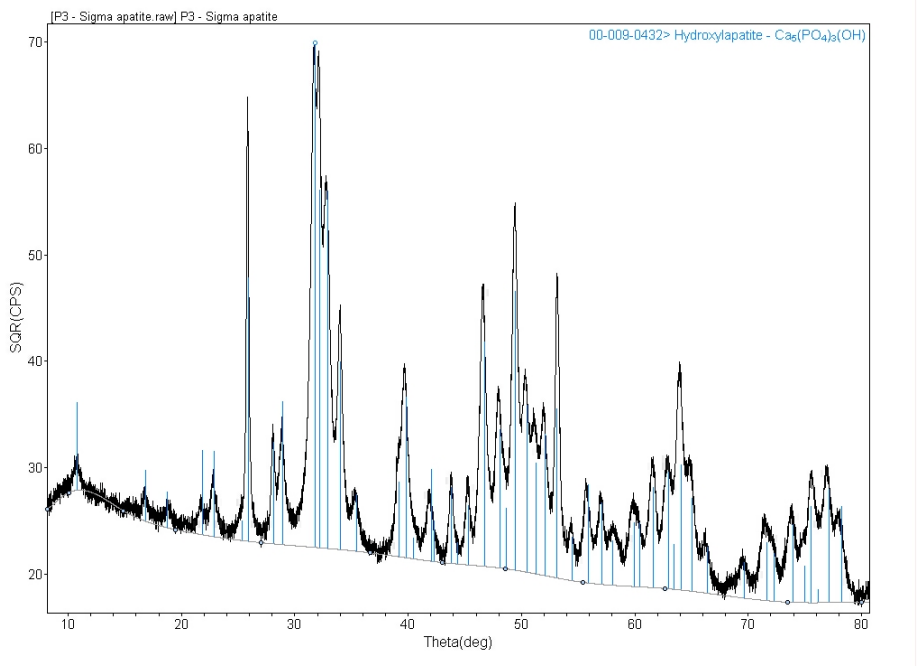

Figure A.2. XRD pattern for apatite – 1 (Sigma Aldrich) with counts on y-axis versus theta on the x-axis.

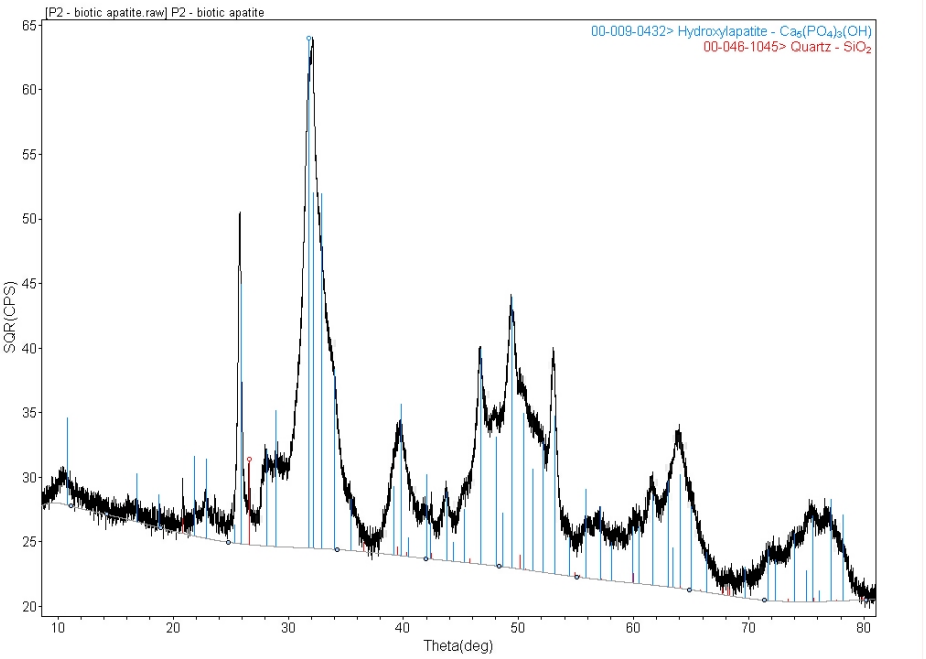

Figure A.3. XRD pattern for apatite – 2 (biotically produced apatite) synthesized at PNNL with counts on y-axis versus theta on the x-axis.

A.2.2 X-ray Diffraction Patterns for Porous Media

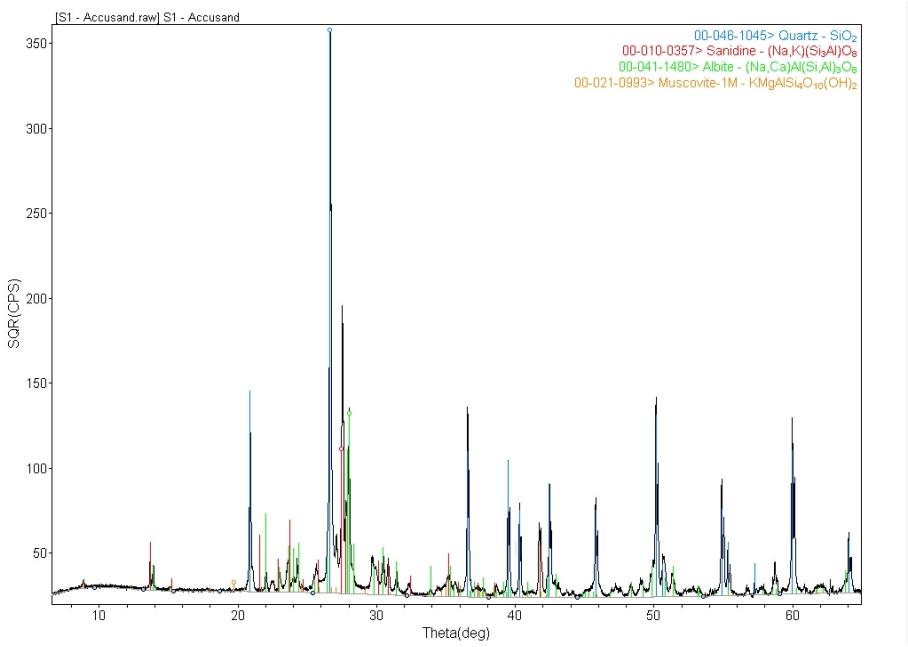

Figure A.4. XRD pattern for Accusand with counts on y-axis versus theta on the x-axis.

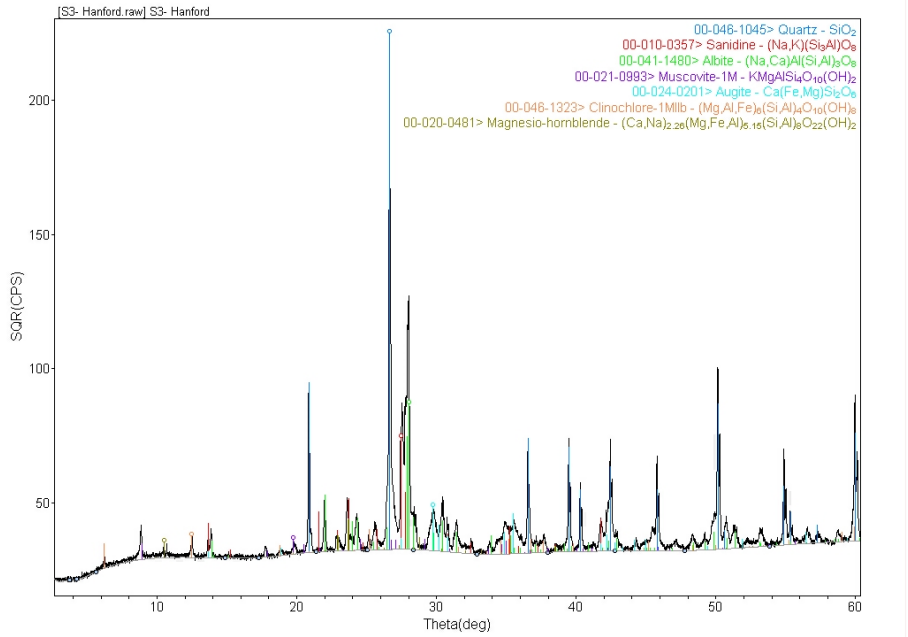

Figure A.5. XRD pattern for Hanford formation sediments with counts on y-axis versus theta on the x-axis.

A.2.3 Determination of Water Content

Moisture content was measured using ASTM Method D2216-19 based on drying of 2-3 grams of sediment at 105°C.

A.2.4 Total Inorganic and Organic Carbon in Sediments

Solid sediment samples were analyzed for total carbon (TC) and inorganic carbon (IC) using a Shimadzu combustion carbon analyzer TOC-L CSH/CSN E100V equipped with a Solid Sample Module, Model SSM-5000A (Shimadzu Scientific Instruments, Inc., Columbia, MD 21046). Samples and standards were weighed into ceramic sample boats that were pre-cleaned with 2N hydrochloric acid (diluted from Fisher Scientific catalog# A144C-212, lot# 043414), rinsed with deionized water, dried, and then fired at 900°C in a muffle furnace for 30 minutes. The TC was determined by combustion at 900°C. The IC was determined by adding 85% phosphoric acid (Fisher Scientific catalog# A260-500, lot# 076856) to the sample at 200°C. A non-dispersive infrared gas analyzer was used to detect the resultant carbon dioxide gas. The total organic carbon (TOC) was determined by difference, TOC = TC-IC. A primary TC standard was made with dextrose (D-glucose) solid (C6H12O6, 40.0% C, Fisher Scientific catalog# D16-500, lot # 170457). A verification TC standard was made with dextrose (D-glucose) solid, C6H12O6, f.w. 180.16, 40.0% C, EMD Millipore, Inc., cat# DX0145-1, lot # K47150008629. Sodium bicarbonate was used for the primary IC calibration standard (NaHCO3, 14.3% C, Fisher Scientific catalog# S233-500, lot# 172497). A verification IC standard was prepared from solid sodium bicarbonate, NaHCO3, f.w. 84.01, 14.3% C, Acros Organics, Co., cat# 424270250, lot# A0373468.

A.2.5 Extractions for Phosphorus in Sediments

Two sequential liquid extractions were conducted in series on selected pre- and post-injection sediment samples. These extractions are operationally defined and may not necessarily be representative of the targeted fraction depending on sample conditions, although previous research suggests some association (Hall et al. 1996; Gleyzes et al. 2002; Chao and Zao 1983; Larner et al. 2006; Mossop and Davison 2003; Sutherland and Tack 2002). Extraction 1 is an ammonium oxalate extraction designed to dissolve Fe oxides (1 h) at room temperature, and extraction 6 is 8 M HNO_3 at 95°C (2 h) designed to dissolve a portion of sediment minerals. The 8 M HNO_3 extraction is a strong but incomplete digestion that is expected to dissolve elements that are potentially environmentally available. For example, previous research has shown that an 8 M HNO_3 acid extraction may remove 70% of total trace metals, 40-60% of Fe and Mn, 25% of major alkaline earth metals (Ca and Mg), 15% of Al and Ti, and negligible Si (< 0.03%) based on a comparison of acid extracts with quantitative X-ray fluorescence measurements (Serne et al. 2002, 2008). These sequential extractions are conducted at a 1:3 sediment:liquid ratio.

A.3 Artificial Groundwater and Porewater

Table A.1. Artificial groundwater constituents.

Constituent	Conc. (mg/L)	Mass for 1 L (g)
H_2SiO_3*nH_2O, silicic acid	15.3	0.0153
KCl, potassium chloride	8.2	0.0082
$MgCO_3$, magnesium carbonate	13	0.013
NaCl, sodium chloride	15	0.015
$CaSO_4$, calcium sulfate	67	0.067
$CaCO_3$, calcium carbonate	150	0.15

Table A.2. Artificial perched water constituents.

Constituent	Conc. (mg/L)
$NaHCO_3$, sodium bicarbonate	900
$KHCO_3$, potassium bicarbonate	31
$MgSO_4 \cdot 7H_2O$, magnesium sulfate	67
$CaSO_4 \cdot 2H_2O$, calcium sulfate	9.7
Na_2SO_4, sodium sulfate	248
NaCl, sodium chloride	193

A.3.1 Solution Characterization by ICP-OES

Metals were analyzed quantitatively using a PerkinElmer Optima 8300 dual view inductively coupled plasma optical emission spectrometry (ICP-OES) and a PerkinElmer S-10 auto-sampler interface. The instrument was calibrated using standards made by the High-Purity Standards (Charleston, SC) to generate calibration curves. All samples and standards were diluted with 2% nitric acid (Fisher Scientific, Optima trace metal grade) and twice deionized water with resistivity no lower than 18.0 MΩ-cm. Serial dilutions were made to investigate and correct for matrix interferences. This method is similar to EPA SW-846 Method 6010C, *Inductively Coupled Plasma-Atomic Emission Spectrometry* (EPA 2007; PNNL 2016).

A.3.2 Total Inorganic Carbon in Solution

IC was determined by using a Shimadzu combustion carbon analyzer TOC-L CSH/CSN E100V with a manual injection block. Fifty-microliter samples were injected with a syringe into 25% phosphoric acid (ACS grade, Sigma Aldrich#438081-500mL) at ambient lab temperature. A non-dispersive infrared gas analyzer was used to detect the resultant carbon dioxide gas. The inorganic carbon primary standard was made from sodium bicarbonate solid (Fisher Chemical Co., Cat # S233-500, lot# 172497) and sodium carbonate solid (LabChem Co., Cat# LC229651, lot# G153-16). The inorganic carbon verification standard was made from sodium bicarbonate solid (Acros Organics Co., Cat # 424270250, lot# A0373468) and sodium carbonate solid (Acros Organics Co, Cat# 42428-5000, lot# B0143079). The calibration range for inorganic carbon was 0.5 to 50 ppm as C.

A.4 References

ASTM D2216-19, *Standard Test Methods for Laboratory Determination of Water (Moisture) Content of Soil and Rock by Mass*. ASTM International, West Conshohocken, PA. www.astm.org.

Brunauer S, PH Emmett, and E Teller. 1938. "Adsorption of gases in multimolecular layers." *Journal of the American Chemical Society* 60:309-319.

Chao T and L Zhou. 1983. "Extraction techniques for selective dissolution of amorphous iron oxides from soils and sediments." *Soil Science Society of America Journal* 47(2):225-232.

EPA 2007. *Inductively Coupled Plasma Atomic Emission Spectrometry*. Test Method 6010C, U.S. Environmental Protection Agency, Washington, D.C.

Gleyzes C, S Tellier, and M Astruc. 2002. "Fractionation studies of trace elements in contaminated soils and sediments: a review of sequential extraction procedures." *Trends in Analytical Chemistry* 21(6-7):451-467.

Hall G, J Vaive, R Beer, and N Hoashi. 1996. "Selective leaches revisited, with emphasis on the amorphous Fe oxyhydroxide phase extraction." *Journal of Geochemical Exploration* 56:59-78.

Larner B, A Seen, and A Townsend. 2006. "Comparative study of optimized BCR sequential extraction scheme and acid leaching of elements in certified reference material NIST 2711." *Analytica Chimica Acta* 556:444-449.

Lawter AR, WL Garcia, RK Kukkadapu, O Qafoku, ME Bowden, SA Saslow, and NP Qafoku. 2018. "Technetium and iodine aqueous species immobilization and transformations in the presence of strong reductants and calcite-forming solutions: Remedial action implications." *Science of the Total Environment* 636:588-595.

Mossop K and C Davison. 2003. "Comparison of original and modified BCR sequential extraction procedures for the fractionation of copper, iron, lead, manganese, and zinc in soils and sediments." *Analytica Chimica Acta* 478:111-118.

PNNL. 2016. *Inductively Coupled Plasma Optical Emission Spectrometry, Technical Procedur*e. Pacific Northwest National Laboratory, Richland, WA.

Qafoku NP, et al. 2018. *Conceptual Model of Subsurface Processes for Iodine at the Hanford Site*. PNNL-28053, Rev 1.0, Pacific Northwest National Laboratory, Richland, WA.

Saslow SA, S Kerisit, T Varga, KC Johnson, NM Avalos, AR Lawter, and NP Qafoku. 2019. "Chromate effect on iodate incorporation into calcite." *ACS Earth and Space Chemistry* 3:1624-1630.

Serne RJ, BN Bjornstad, HT Schaef, BA Williams, DC Lanigan, DG Horton, RE Clayton, AV Mitroshkov, VL LeGore, MJ O'Hara, CF Brown, KE Parker, IV Kutnyakov, JN Serne, GV Last, SC Smith, CW Lindenmeier, JM Zachara, and DB Burke. 2002. *Characterization of Vadose Zone Sediment: Uncontaminated RCRA Borehole Core Samples and Composite Samples*. PNNL-13757-1, Pacific Northwest National Laboratory, Richland, WA.

Serne RJ, BN Bjornstad, DC Lanigan, GW Gee, CW Lindenmeier, RE Clayton, VL LeGore, MJ O'Hara, CF Brown, GV Last, IV Kutnyakov, DS Burke, TC Wilson, and BA Williams. 2008. *Characterization of*

Vadose Zone Sediment: Borehole 299-W12-19 [SX-115] in the S-SX Waste Management Area. PNNL-13757-2, Rev. 1.0, Pacific Northwest National Laboratory, Richland, WA.

Sumner ME. 2000. *Soil Chemistry*. CRC Press, Boca Raton, FL.

Sutherland R and F Tack. 2002. "Determination of Al, Cu, Fe, Mn, Pb, and Zn in certified reference materials using the optimized BCR sequential extraction procedure." *Analytica Chimica Acta* 454:249-257.

Szecsody JE, ML Rockhold, M Oostrom, RM Moore, C Burns, MA Williams, L Zhong, JS Fruchter, J McKinley, J Vermeul, M Covert, TW Wietsma, AT Breshears, and B Garcia. 2009. *Sequestration of Sr-90 Subsurface Contamination in the Hanford 100-N Area by Surface Infiltration of a Ca-citrate-phosphate Solution*. PNNL-18303, Pacific Northwest National Laboratory, Richland, WA.

Szecsody JE, L Zhong, M Oostrom, VR Vermeul, JS Fruchter, and MD Williams. 2012. Use of Polyphosphate to Decrease Uranium Leaching in Hanford 300 Area Smear Zone Sediment. PNNL-21733, Pacific Northwest National Laboratory, Richland, WA.

Szecsody JE, RM Moore, M Rigali, VR Vermelu, and J Luellen. 2016. *Use of Ca-citrate-phosphate solution to form hydroxyapatite for uranium stabilization of Old Rifle sediments: Laboratory proof of principle studies*. PNNL-25303, Pacific Northwest National Laboratory, Richland, WA.

Szecsody JE, HP Emerson, RD Mackley, CT Resch, BN Gartman, CI Pearce, SA Saslow, O Qafoku, KA Rod, and MK Nims. 2020b. *Evaluation of the Change in Uranium Mobility in Sediments from the Hanford 300-FF-5 Stage B Polyphosphate Field Injection*. PNNL-29650, Pacific Northwest National Laboratory, Richland, WA.

Wellman DM, JM Zachara, C Liu, NP Qafoku, SC Smith, and SW Forrester. 2008. "Advective Desorption of Uranium(VI) from Contaminated Hanford Vadose Zone Sediments under Saturated and Unsaturated Conditions." *Vadose Zone Journal* 7:1144-1159.

Appendix B – Geometric and Formation Factor Calculations

The following tables summarize the geometric factors estimated for all nine of the 8.0-cm-long columns used for spectral induced polarization (SIP) experiments as well as the formation factors for both sand and Hanford formation sediments. These geometric factor constants are estimated based on a linear regression of the measured resistance versus solution resistivity with columns filled with solutions of variable ionic strength from 0.001 to 1.0 M NaCl. The values in Table B.1 are based on an average of constants estimated from a linear regression at seven frequencies (0.01, 0.1, 1.0, 10, 100, 1000, and 10,000 Hz). The low variability in factors across frequency as expected based on theory is confirmed with these experimental results. For longer columns, geometric factors were estimated based on geometry (A/L).

The formation factors are estimated based on a linear regression of real conductivity versus solution conductivity in columns packed with the targeted porous media material and saturated with solutions of variable ionic strength from 0.001 to 1.0 M NaCl for sand in Table B.2 and Hanford formation sediments in Table B.3. There is also little variability with respect to frequency as shown by the examples of regressions conducted across the frequency range (from 0.01 to 100 Hz) in Table B.4 and Figure B.1. Similar results were observed for Hanford formation sediments (*not shown*).

Table B.1. Geometric factor for 8.0-cm-long, 1.25-cm-ID SIP columns with standard deviation based on estimates across seven orders of magnitude of frequency (estimated at 0.01, 0.1, 1.0, 10, 100, 1000, and 10,000 Hz).

Column	K (cm^{-1})	R^2
A	1.55 ± 0.07	0.9999
B	2.19 ± 0.01	0.9999
C	1.93 ± 0.01	0.9998
D	1.99 ± 0.00	0.9999
E	2.02 ± 0.00	0.9998
F	1.87 ± 0.01	0.9999
G	1.95 ± 0.01	0.9999
H	1.18 ± 0.01	0.9999
I	2.09 ± 0.01	0.9999

Table B.2. Formation factor for sand (40-60 mesh) with standard deviation based on the average of three columns, each of which are based on an average across five orders of magnitude of frequency (estimated at 0.01, 0.1, 1.0, 10, and 100 Hz and averaged for each column).

Column	F (unitless)
D	5.103 ± 0.008
E	5.311 ± 0.001
F	5.071 ± 0.001
Average	*5.16 ± 0.13*

Table B.3. Formation factor for Hanford formation sediments (< 2 mm) with standard deviation based on the average of three columns each of which are based on an average across five orders of magnitude of frequency (estimated at 0.01, 0.1, 1.0, 10, and 100 Hz and averaged for each column).

Column	F (unitless)
D	3.848 ± 0.005
E	3.593 ± 0.011
F	3.810 ± 0.011
Average	*3.75 ± 0.14*

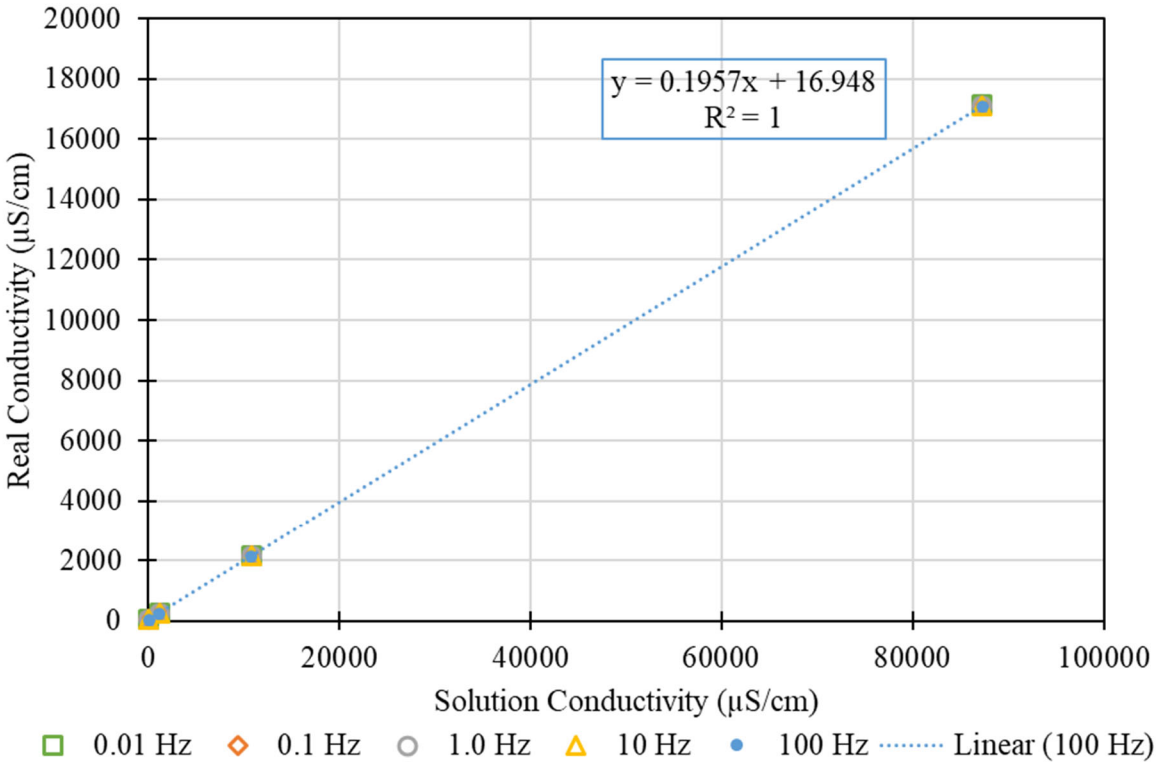

Figure B.1. Comparison of formation factor regressions for Column D packed with sand at variable frequency. Note: Each frequency nearly overlays on top of the other.

Table B.4. Comparison of formation factor estimated at variable frequencies in sand.

Frequency (Hz)	Formation Factor	Standard Deviation	R^2
0.01	5.313	0.0056	0.999998
0.1	5.3116	0.006	0.999997
1	5.3107	0.0057	0.999998
10	5.3107	0.0057	0.999998
100	5.3095	0.0054	0.999998

Appendix C – Development of SIP Electrodes for Unsaturated Conditions

A Novel Electrode Design for Spectral Induced Polarization Measurements in Unsaturated Porous Media
Jon Thomle, Adam R. Mangel

Spectral induced polarization (SIP) is a remote subsurface sensing and imaging method that measures the frequency dependent electrochemical polarization across charged interfaces. Charged interfaces, known as electrical double layers (EDLs), occur at soil grains due to charge balances between the soil grain and the ions present in porewater. Polarization responses are typically on the order of a few milliradians; therefore, it is important to construct electrodes in a way that does not obscure these small signals. Additionally, special considerations must be taken for measuring SIP signals in unsaturated porous media, as the porewater often provides electrical coupling between the electrode and the sample. In order to address these challenges, a novel electrode design was tested for acquisition of SIP data on unsaturated porous media.

For SIP data collection in porous media, it can be difficult to maintain coupling between the electrode and the porous media. For saturated conditions this is simpler, as ions in solution provide an electrolytic pathway for electricity to flow from the electrode and into the sample. As fluid is removed from the sample, however, the coupling can be adversely affected due to the less abundant pathways for electricity to flow. Many authors have introduced designs for electrodes that contain an electrode in some solution that is in hydrologic contact with the sample across some porous membrane. For example, Zimmerman et al. (2012) discuss the use of a plastic tube filled with solution and a ceramic membrane with high air-entry pressures to maintain a liquid bridge between the electrode and the sample. They propose that an optimal ceramic membrane should have high surface area with a minimal wall thickness to prevent issues with high contact impedance (Zimmermann et al. 2012).

Several electrode designs were examined to advance application of SIP technology, reduce costs associated with electrode construction, and explore alternative electrode designs. Electrodes were tested using a simple four-electrode, dipole-dipole configuration in tap water with salts added to increase electrical conductivity. Test were performed in water due to the absence of polarization mechanisms; therefore, no polarization response should be observed. The final electrode design and the associated testing data are shown in Figure C.1. Central to the electrode design is a plug of silica flour in which the brass wire electrode is embedded. The silica flour is comparable to the porous ceramic cups suggested by Zimmerman et al. (2012), using a high air-entry pressure to maintain saturation. The loose silica flour is packed into the electrode body and held in place with a hydrophilic porous plastic frit. Overall, the water test data show that the electrodes are performing favorably, with polarization responses generally below 0.5 milliradians at frequencies less than 1000 Hz. These results are in good agreement with published quantities for electrode responses and cost roughly $10 in materials, with the majority of the cost coming for the SMB [sub miniature version B (type of radio frequency connector)] connector. Additional testing of the electrodes is required to fully evaluate the performance over a range of soil water saturation values. These tests should first be performed on soil analogues, like silica gel, before testing on actual soil samples in order to provide experimental control on polarization mechanisms.

Additional testing and development of the unsaturated electrode designed here is included in Thomle et al. (2021)

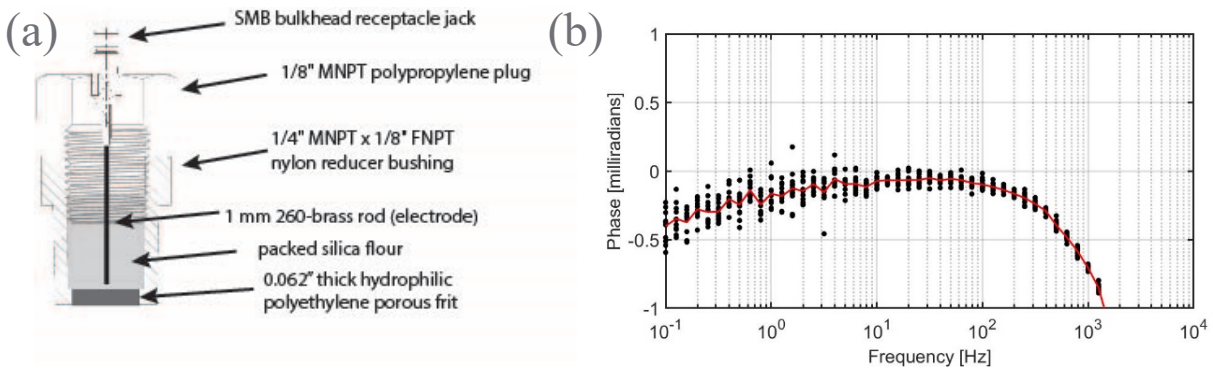

Figure C.1. (a) Schematic of SIP electrode and (b) results of repeat measurements with a four-electrode configuration in water.

References

Thomle et al. 2021 "An alternative electrode design for accurate spectral induced polarization measurements in variably saturated porous media." *Applied Geophysics*. In prep.

Zimmermann E, J Huisman, B Wolters, and S van Waasen. 2012. "Optimal electrode design for improved phase accuracy of spectral EIT images." Proceedings of the 6th International Symposium on Process Tomography, Cape Town, South Africa 26, 2012-2028.2003.

Appendix D – Preliminary SIP Response for FeS

For a pure silica sand (with no clay, iron oxides, or other minerals that exhibit a capacitance), the addition of a small mass of FeS (mackinawite) resulted in a large positive imaginary conductivity increase at low to mid frequency (green circles, Figure D.1c), but a decrease in imaginary conductivity for high FeS addition. For a Hanford formation sediment, the same FeS additions resulted mainly in a decrease in the normalized imaginary conductivity (Figure D.1d). From a related spectral induced polarization (SIP) study (Szecsody et al. 2020), adsorbed ferrous iron and two different iron sulfides (mackinawite, pyrite, 200 μmol/g is approximately 1.7 wt.%) were added to Hanford formation sediments. Normalizing the SIP changes in imaginary conductivity for ferrous iron or iron sulfide resulted in different shifts for the two ferrous iron phases. More specifically, addition of adsorbed ferrous iron showed an increase in the imaginary conductivity in the 0.1 to 10 Hz range, whereas additions of FeS and FeS_2 showed a decrease in the imaginary conductivity in the 0.001 to 0.1 Hz range (Figure D.1a and b). The sensitivity of the change in imaginary conductivity was greater for the adsorbed ferrous iron as compared to iron sulfides, although different increases and decreases have been observed for different porous media (Orozco et al. 2011; Williams et al. 2009). For different sediments, the increase in capacitance (i.e., greater phase angle shift) also differs.

Chemical reduction of Hanford formation sediments with calcium polysulfide (CPS) results primarily in the formation of iron sulfide precipitates. The normalized imaginary conductivity of the CPS-treated sediment as observed in previous research (Figure D.1) shows primarily a decrease in the 0.001 to 0.1 Hz frequency, which is similar to FeS and FeS_2 additions to the same sediment (Figure D.1b,d) and FeS addition to sand (Figure D.1c). To summarize the results of iron sulfide additions in this project, FeS (mackinawite) additions at 1.7 wt.% to both sand and Hanford formation sediments resulted in a decrease in the imaginary conductivity in the low range frequency (< 1 Hz). This response to FeS additions was similar to that observed in a previous study (Figure D.1a,b and Figure D.2). This imaginary conductivity response is the opposite of the response to sulfur modified iron (SMI) addition at the same frequency range, although additional measurements are necessary as these columns were not able to be conducted in triplicate.

The SIP response for iron sulfide (FeS, mackinawite) addition to sand or sediment differed significantly from zero valent iron (ZVI) or SMI addition to sand or sediment. For a single concentration of FeS added to sand or Hanford formation sediment in this study (1.7 wt.%) or multiple concentrations of FeS addition to Hanford sediment in a previous study (Szecsody et al. 2020), there was a consistent decrease in the imaginary conductivity (60 to 100 μS/cm) in the low frequency range (0.01 to 1 Hz) in contrast to a consistent increase in the imaginary conductivity for ZVI (at > 100 Hz) and SMI (0.01 – 10 Hz) additions to sand or sediment. The sensitivity of measurement of FeS additions to sand (-30 mrad/1 wt.% FeS) or sediment (23 mrad/1 wt.% FeS) was about the same as ZVI or SMI additions, but the imaginary conductivity changes were larger, with a 59 μS/cm imaginary conductivity decrease for 1 wt.% FeS addition to sand and a 35 μS/cm imaginary conductivity decrease for 1 wt.% FeS addition to Hanford sediment. Therefore, detection of ZVI, SMI, or FeS addition to sediments was generally highly sensitive and SIP response differed between the three amendments in terms of frequency response.

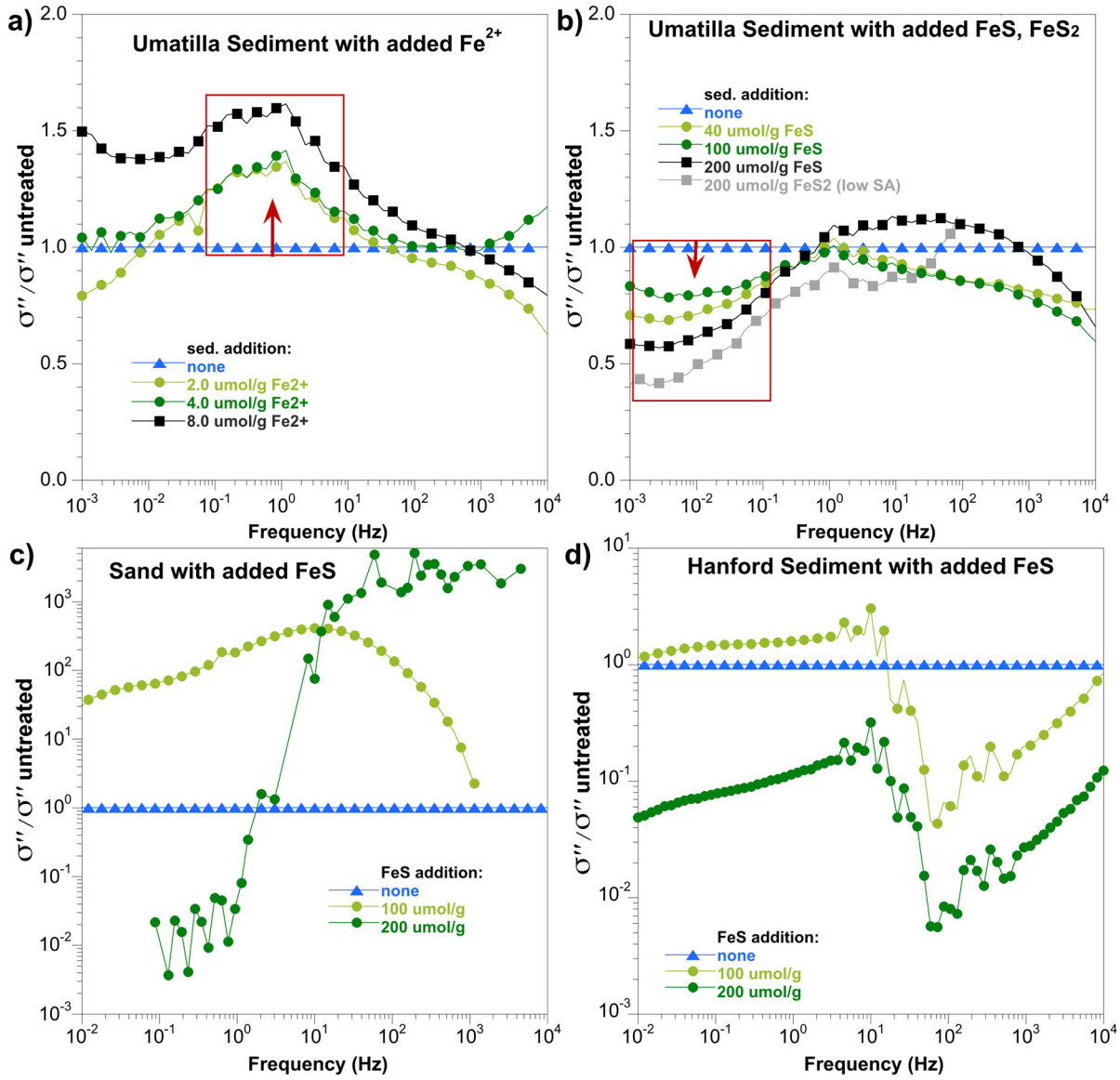

Figure D.1. Change in the normalized imaginary conductivity with (a) Hanford formation sediment with additions of Fe^{2+}, (b) Hanford formation sediment with additions of FeS, FeS_2, (c) sand with FeS additions, and (d) Hanford sediment with FeS additions. SIP experiments in (a) and (b) are from previous research (Szecsody et al. 2020).

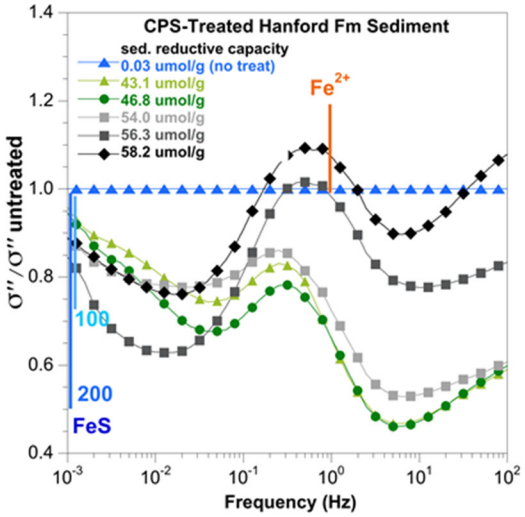

Figure D.2. Normalized imaginary conductivity of calcium polysulfide treated Hanford formation sediments (Szecsody et al. 2020).

References

Orozco AF, KH Williams, PE Long, SS Hubbard, and A Kemna. 2011. "Using complex resistivity imaging to infer biogeochemical processes associated with bioremediation of an uranium-contaminated aquifer." *Journal of Geophysical Research: Biogeosciences* 116.

Szecsody JE, PG Tratnyek, TC Johnson, HP Emerson, JL Robinson, E Placencia-Gómez, M Bradley, TN Thomle, MJ Truex, CT Resch, and BN Gartman. 2020. *Characterization of Enhanced Subsurface Abiotic Reactivity with Electrical Resistivity Tomography/Induced Polarization.* SERDP Project ER-2619 Final Report, Strategic Environmental Research and Development Program (SERDP), Arlington, VA. https://www.serdp-estcp.org/.

Williams KH, A Kemna, MJ Wilkins, J Druhan, E Arntzen, AL N'Guessan, PE Long, SS Hubbard, and JF Banfield. 2009. "Geophysical monitoring of coupled microbial and geochemical processes during stimulated subsurface bioremediation." *Environmental Science & Technology* 43:6717-6723.

Appendix E – *In Situ* Delivery of Micron-Sized ZVI with SIP Monitoring

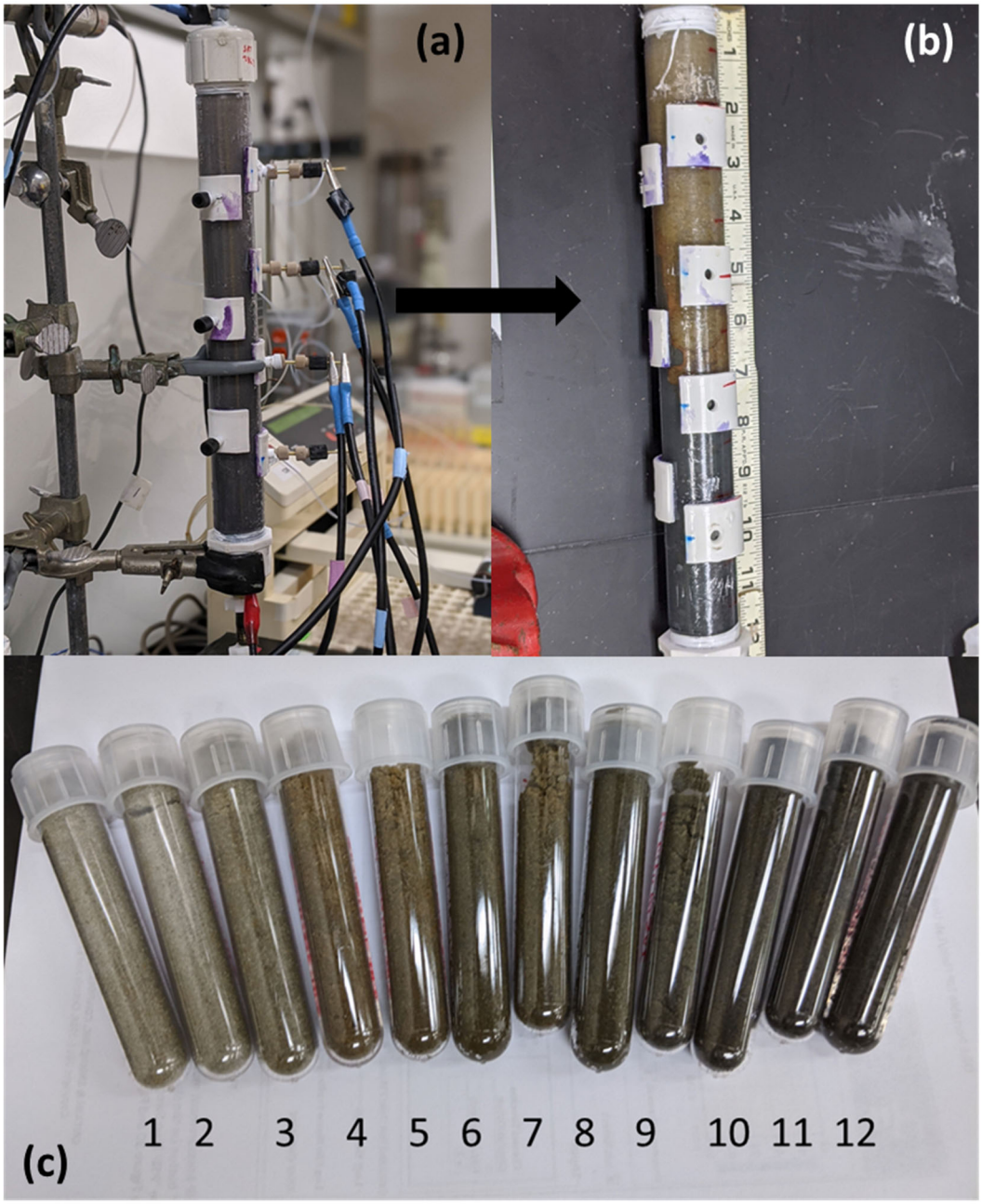

Figure E.1. Visual changes in solid phase observed over time with (a) 1 day after injection of ZVI-2, (b) after aging for 130 days with ZVI-2, and (c) solid phase changes across the column from influent end (12) to effluent end (1).

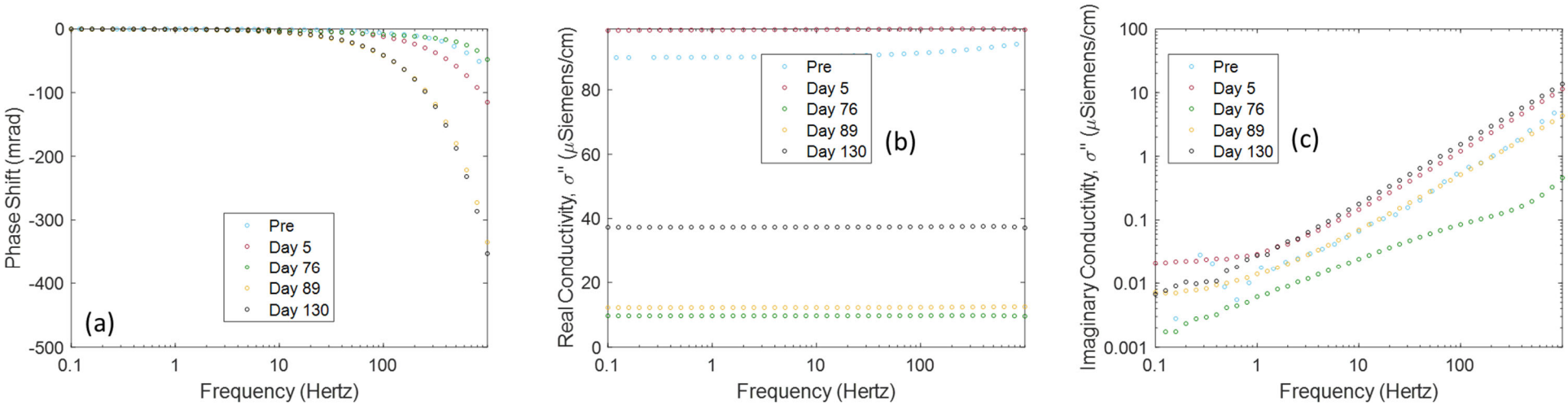

Figure E.2. Pair 1 spectral induced polarization (SIP_ response before and after injection of 1.5 wt.% ZVI-2 (1-5 µm) with artificial groundwater (AGW) and 800 mg/L xanthan gum at 1 mL/min with (a) phase shift in mrad, (b) real conductivity in µS/cm, and (c) imaginary conductivity in µS/cm, where pair 1 is the electrode potential pair closest to the influent end cap and pair 3 is the electrode potential pair closest to the effluent end cap, with *points* and *circles* representing the average of three loops of data collected on one column.

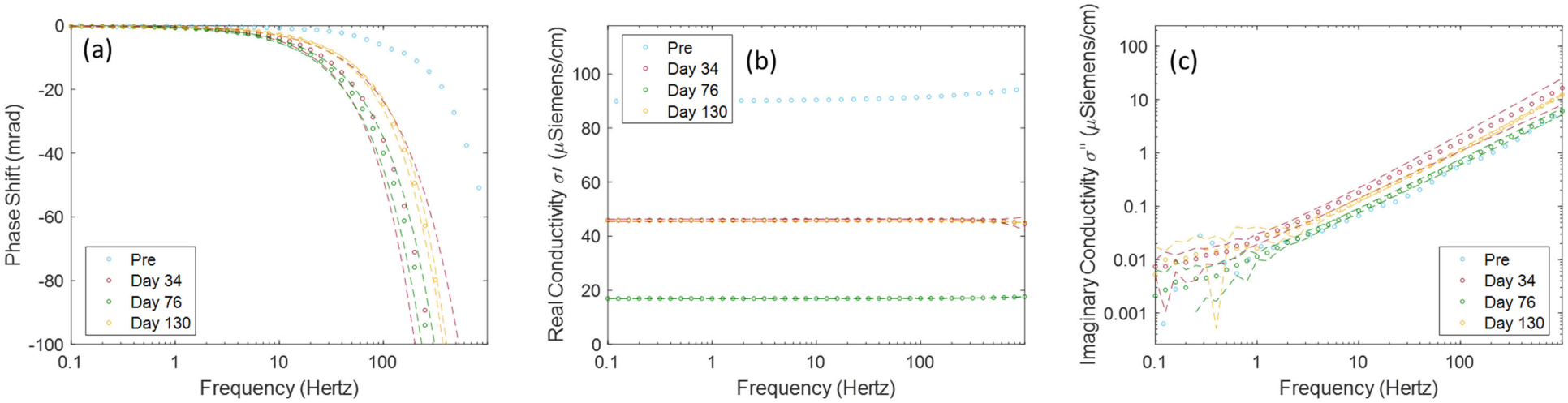

Figure E.3. Pair 2 SIP response before and after injection of 1.5 wt.% ZVI-2 (1-5 µm) with AGW and 800 mg/L xanthan gum at 1 mL/min with (a) phase shift in mrad, (b) real conductivity in µS/cm, and (c) imaginary conductivity in µS/cm, where pair 1 is the electrode potential pair closest to the influent end cap and pair 3 is the electrode potential pair closest to the effluent end cap with *points* and *circles* representing the average of three loops of data collected on one column and *dashed lines* representing the 95% confidence interval for the three loops of data collected on the electrode pair.

Appendix F – *In Situ* Delivery of Calcite and Apatite following Aging of SMI

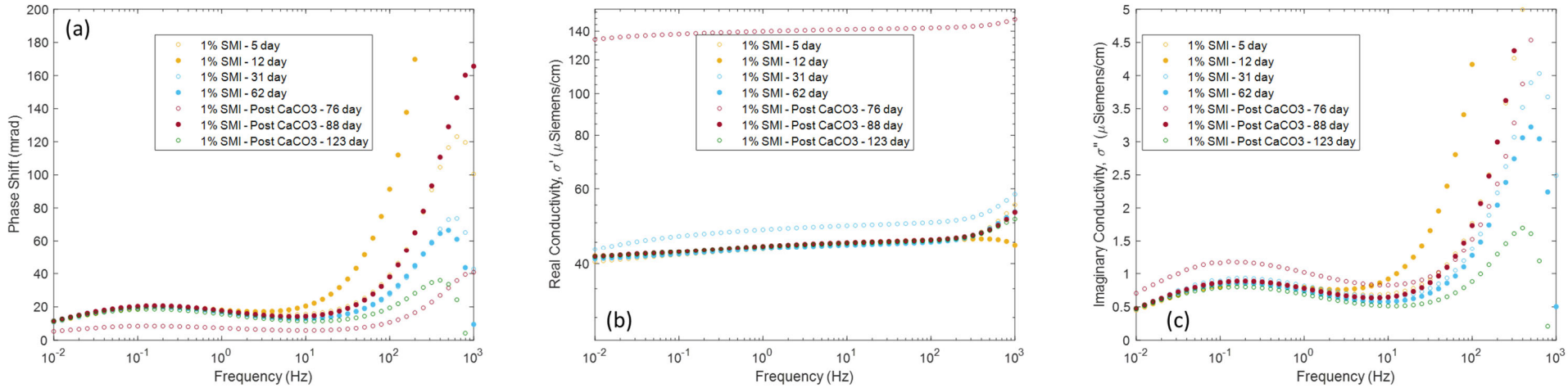

Figure F.1. Change in spectral induced polarization (SIP) response over time for 1 wt.% sulfur modified iron (SMI) with Hanford sediment saturated with artificial groundwater (AGW) followed by injection of calcite forming solutions (70-75 days) and then flushing with AGW in a 24-in. length by 0.5-in. ID column, with (a) phase shift in mrad, (b) real conductivity, (c) imaginary conductivity in µS/cm, where *circles* represent the measurement for each frequency at five days after saturation.

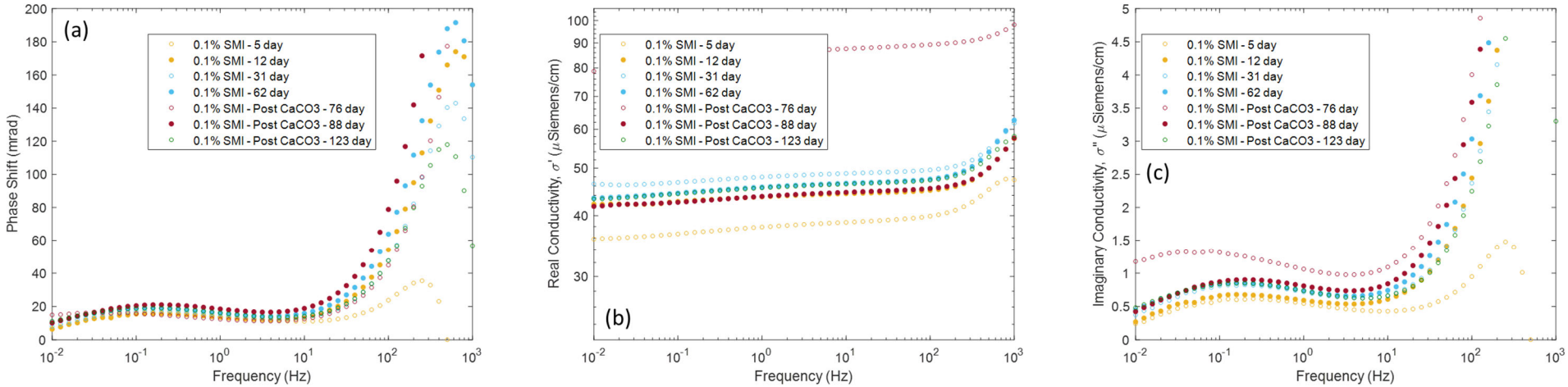

Figure F.2. Change in SIP response over time for 0.1 wt.% SMI with Hanford sediment saturated with AGW followed by injection of calcite forming solutions (70-75 days) and then flushing with AGW in a 24-in. length by 0.5-in. ID column, with (a) phase shift in mrad, (b) real conductivity, (c) imaginary conductivity in µS/cm, where *circles* represent the measurement for each frequency at five days after saturation.

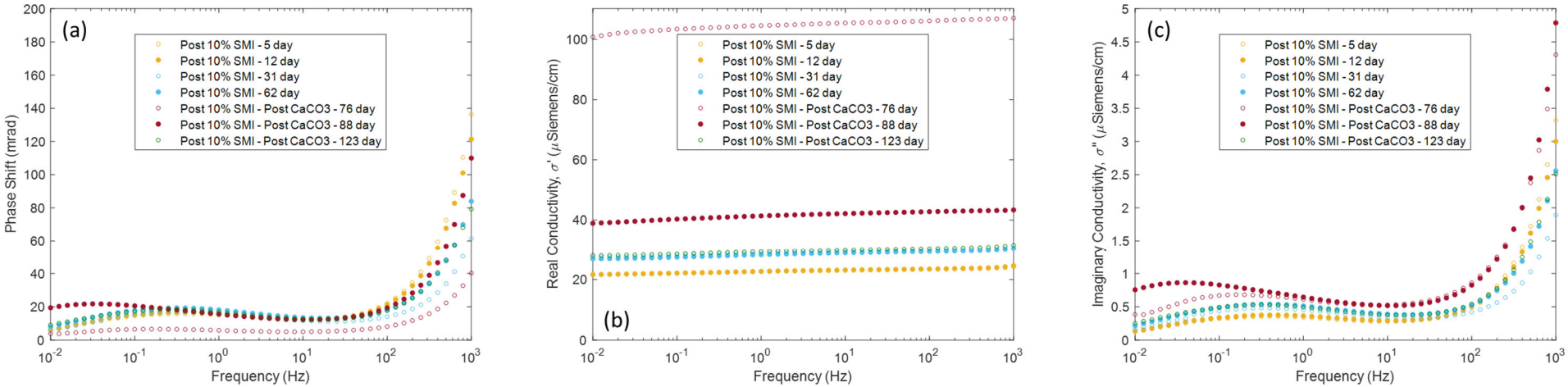

Figure F.3. Change in SIP response over time for the sediment layer immediately after 10 wt.% SMI with Hanford sediment saturated with AGW followed by injection of calcite forming solutions (70-75 days) and then flushing with AGW in a 24-in. length by 0.5-in. ID column, with (a) phase shift in mrad, (b) real conductivity, (c) imaginary conductivity in µS/cm, where *circles* represent the measurement for each frequency at five days after saturation.

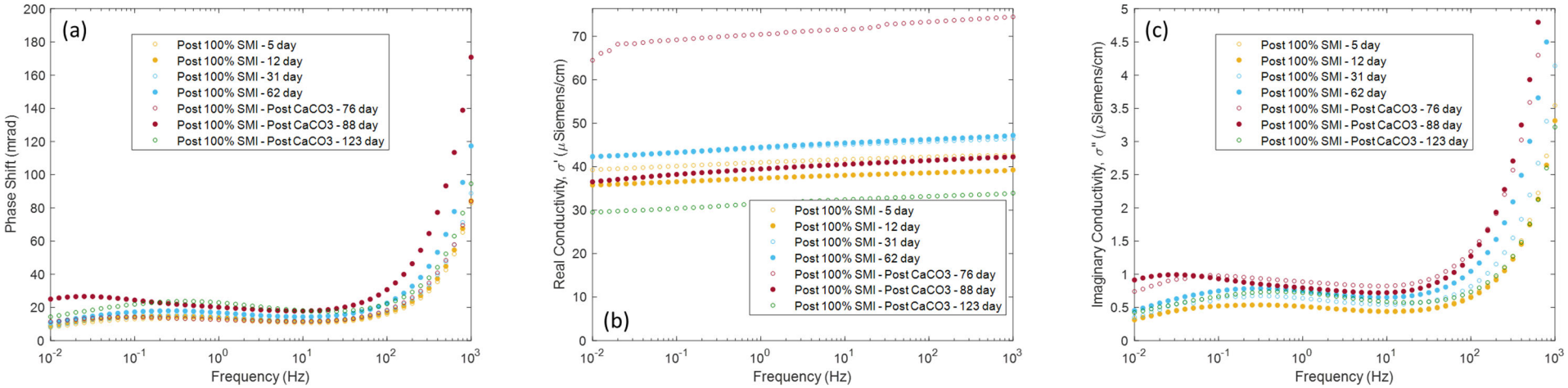

Figure F.4. Change in SIP response over time for the sediment layer immediately after 100 wt.% SMI with Hanford sediment saturated with AGW followed by injection of calcite forming solutions (70-75 days) and then flushing with AGW in a 24-in. length by 0.5-in. ID column, with (a) phase shift in mrad, (b) real conductivity, (c) imaginary conductivity in µS/cm, where *circles* represent the measurement for each frequency at five days after saturation.

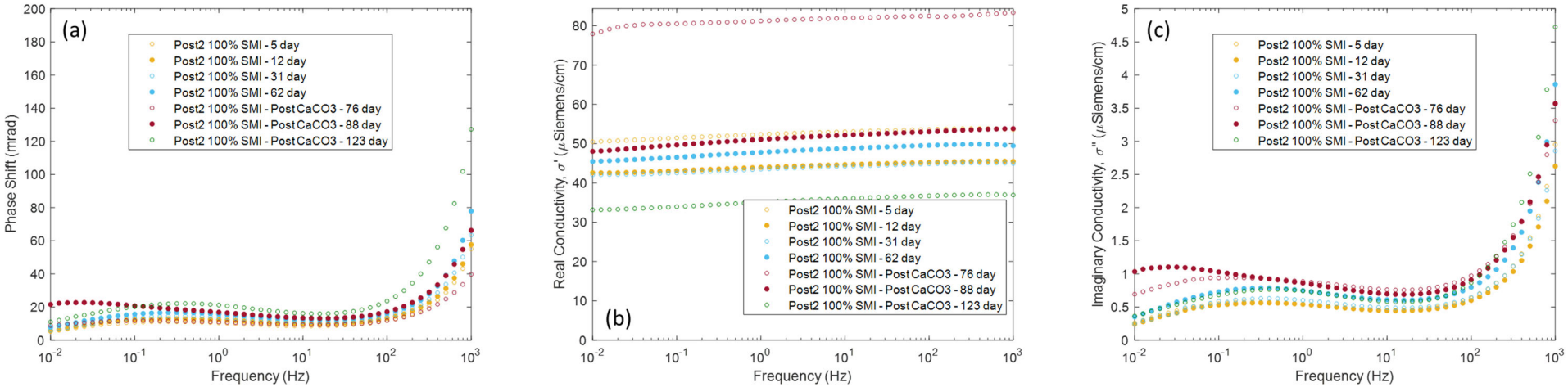

Figure F.5. Change in SIP response over time for the second sediment layer after 100 wt.% SMI with Hanford sediment saturated with AGW followed by injection of calcite forming solutions (70-75 days) and then flushing with AGW in a 24-in. length by 0.5-in. ID column, with (a) phase shift in mrad, (b) real conductivity, (c) imaginary conductivity in µS/cm, where *circles* represent the measurement for each frequency at five days after saturation.

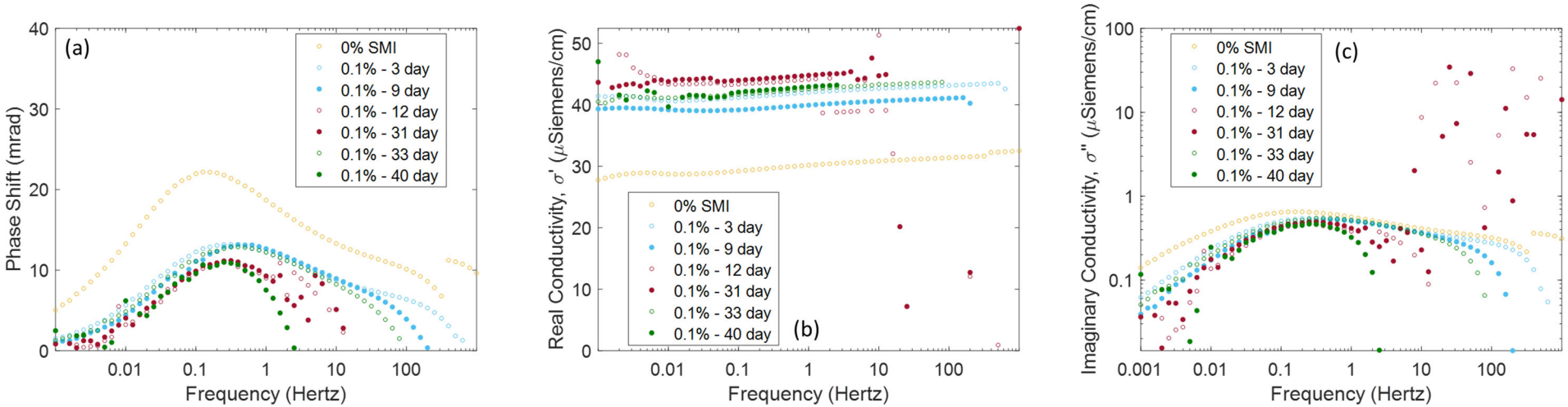

Figure F.6. Layer of Hanford formation sediments with 0.1 wt.% of SMI saturated with AGW in a 24-in. length by 0.5-in. ID column as measured over 40 days with constant flow at 0.025 mL/min, with (a) phase shift in mrad, (b) real conductivity, (c) imaginary conductivity in µS/cm, where circles represent the measurement for each frequency.

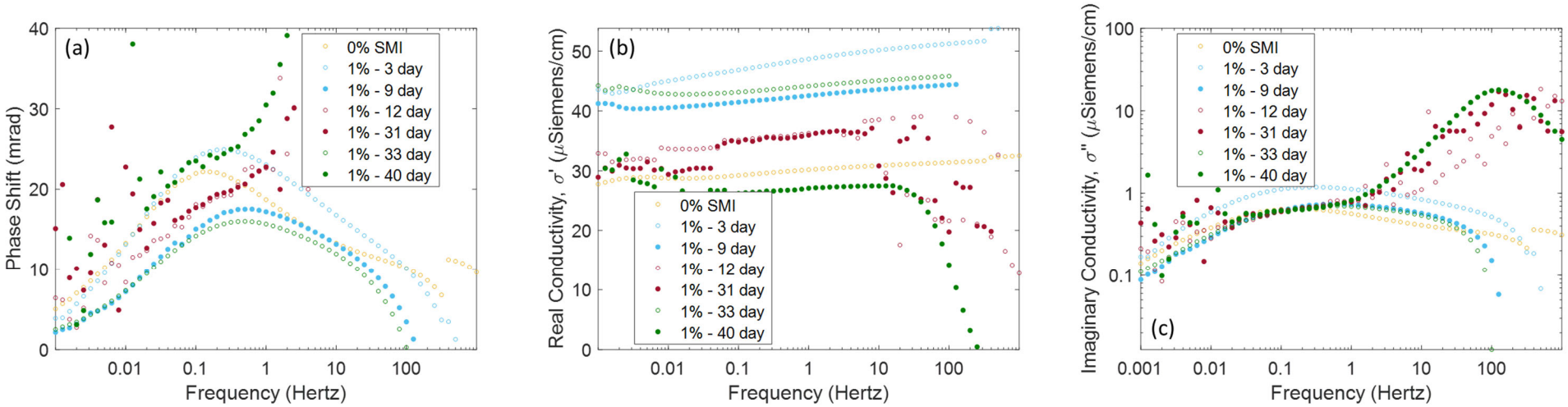

Figure F.7. Layer of Hanford formation sediments with 1 wt.% of SMI saturated with AGW in a 24-in. length by 0.5-in. ID column as measured over 40 days with constant flow at 0.025 mL/min, with (a) phase shift in mrad, (b) real conductivity, (c) imaginary conductivity in µS/cm, where circles represent the measurement for each frequency.

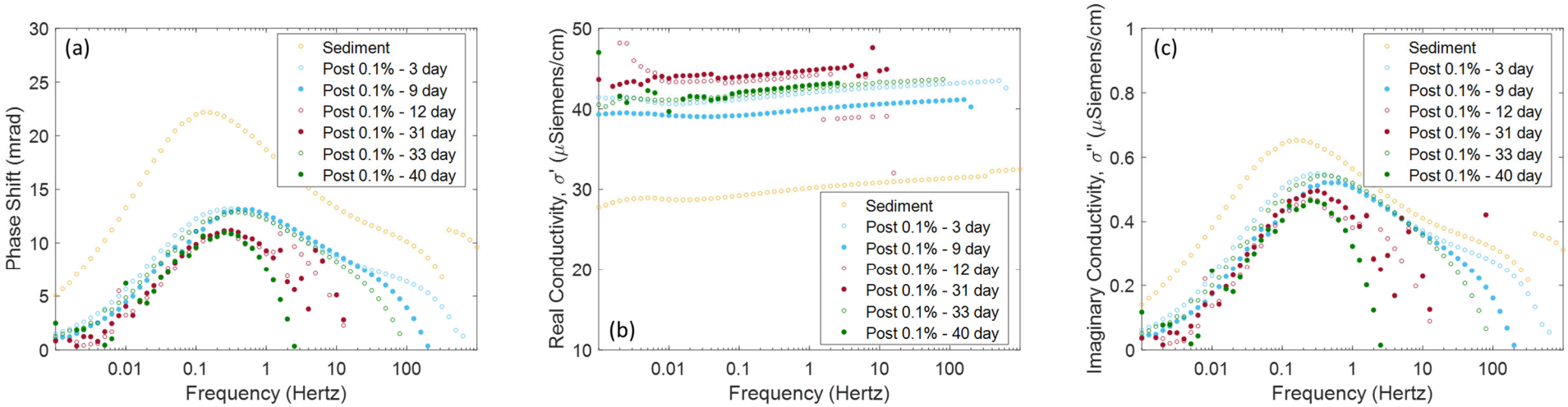

Figure F.8. Layer of Hanford formation sediments after 0.1 wt.% of SMI layer saturated with AGW in a 24-in. length by 0.5-in. ID column as measured over 40 days with constant flow at 0.025 mL/min, with (a) phase shift in mrad, (b) real conductivity, (c) imaginary conductivity in µS/cm, where *circles* represent the measurement for each frequency.

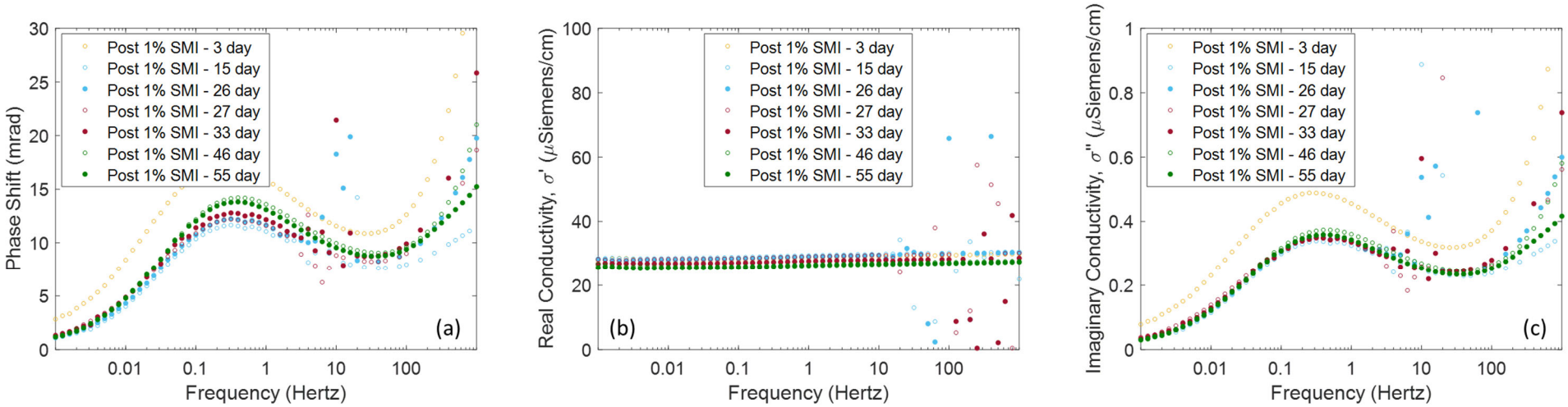

Figure F.9. Layer of Hanford formation sediments after 1 wt.% of SMI layer saturated with AGW in a 24-in. length by 0.5-in. ID column as measured over 55 days with constant flow at 0.025 mL/min, with (a) phase shift in mrad, (b) real conductivity, (c) imaginary conductivity in µS/cm, where *circles* represent the measurement for each frequency.

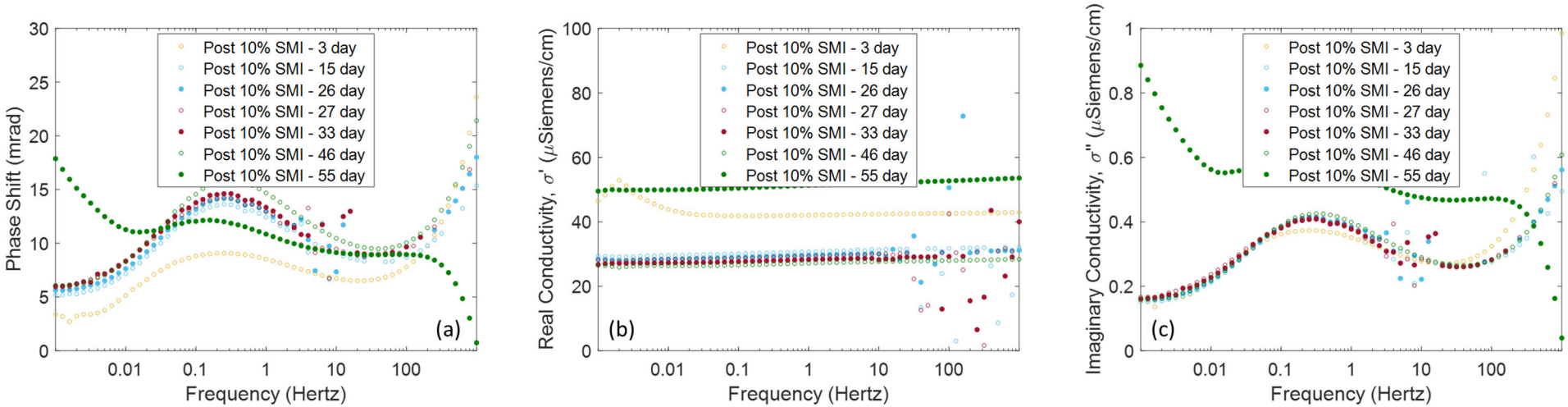

Figure F.10. Layer of Hanford formation sediments after 10 wt.% of SMI layer saturated with AGW in a 24-in. length by 0.5-in. ID column as measured over 55 days with constant flow at 0.025 mL/min, with (a) phase shift in mrad, (b) real conductivity, (c) imaginary conductivity in µS/cm, where *circles* represent the measurement for each frequency.

Pacific Northwest National Laboratory

902 Battelle Boulevard
P.O. Box 999
Richland, WA 99354
1-888-375-PNNL (7665)

www.pnnl.gov